STUDY OF A METHOD OF LOCAL CHEMICAL AND ISOTOPIC ANALYSIS USING SECONDARY ION EMISSION

G. Slodzian

Translation of "Étude d'une métode d'analyse locale chimique et isotopique utilisant l'émission ionique secondaire".
Thesis, University of Paris, 1964.

NATIONAL AERONAUTICS AND SPACE ADMINISTRATION
WASHINGTON   JULY 1965

STUDY OF A METHOD OF LOCAL CHEMICAL AND ISOTOPIC ANALYSIS   **/1
USING SECONDARY ION EMISSION

Georges Slodzian*

29727

A semi-quantitative microanalysis method with secondary ion emission, for directly obtaining distribution electron images whose limit of resolution is of the order of microns, permitting localization of a given light element in a chemical bond and isotopic analysis, is described. The obtainable results are demonstrated on the example of identification of oxides and are extrapolated to all possible solids including metals and minerals. The physical principles of conversion of ion to electron images are discussed, and formulas for computing second- and third-order aberrations are derived. The experimental apparatus, working with argon ion gun, immersion lens, electromagnet, image converter, telephotolens, and fluorescent screen, is described in detail, with suggestions for further improvement in resolving power and sensitivity.

author

INTRODUCTION

Basically, microanalysis has the purpose of establishing the chemical composition of an extremely small zone of a solid specimen. This spot analysis,

---

* Laboratory of Solid-State Physics (Professor R. Castaing); Faculty of Sciences (Centre d'Orsay S.-et-O.).

** Numbers in the margin indicate pagination in the original foreign text.

which has been extended gradually, permits an investigation of local variations in the concentration of any one of the constituent elements and, consequently, the plotting of a diagram giving the distribution of this element within the specimen.

A highly efficient method of microanalysis is already in existence, based on the emission of X-radiation, which had been studied and developed about a dozen years ago by R.Castaing (Bibl.1, 2, 3). The general principle is as follows: An electron beam is focused on the specimen on a "spot" of very small dimensions (diameter less than one micron); the small volume of matter irradiated by the electrons (of the order of μ^3) emits, among others, a characteristic X-ray spectrum of the elements contained within this volume. The wavelength of the lines of the emitted spectrum permits an identification of the chemical nature of the electrons, composing the specimen; based on the intensity of these lines, the quantitative composition can be established with an accuracy of the order of 1%.

This method has already found numerous applications but nevertheless presents several drawbacks:

The presence of a continuous X-ray spectrum, emitted at the same time as the characteristic lines, makes the detection of low-concentration elements in the specimen extremely difficult.

The ready absorption of X-rays of long wavelengths makes the analysis of constituents with low atomic number extremely difficult (such as oxygen, carbon, nitrogen, etc.).

Finally, the distribution curve of an element within the specimen cannot be plotted except by means of a series of stepwise analyses or by the artifact of electronic (Bibl.4, 5) or mechanical (Bibl.6) scanning.

Instead of making use of the emission of a characteristic X-ray spectrum for differentiating the various elements contained in a given specimen, it is also possible to define their mass ratio. From the first, mass spectrography presents two considerable advantages: On the one hand, the light elements are readily detected and, on the other hand, the continuous background due to the diffusion of ions by the residual gas in the vacuum enclosure can be sufficiently reduced to permit the detection of elements in low concentration. Still, it is necessary to select a mode of ionization of matter which permits a localization of the emission of characteristic ions of the elements composing the analyzed material.

Various types of ion sources are used in the spectrographic analysis of /2 solids. In the source with a glow anode, the solid is deposited on a filament heated by passage of an electric current. The incandescence of the filament produces an evaporation of positive ions from the solid. Thus, cesium when deposited on a tungsten filament will emit Cs^+ ions. However, this phenomenon is interesting only for elements that readily change to the ion state. In fact, it is necessary that their ionization potential V_i be lower than the work function $e\varphi$ of an electron of the metal used as support. This limits the elements that can be analyzed to alkalies, alkaline-earth metals, and metals of rare earths. In another type of source, the solid is heated in a small oven in vacuo and its vapor is ionized by an electron beam. The elements that can be analyzed with this process are much more numerous, but in any of these cases it is impossible to obtain a localization of the emission. The advantage of such sources primarily lies in the low energy dispersion of the ions produced by them (0.2 ev for a source with incandescent anode).

The use of a spectrograph with angle and energy focusing (double-focusing)

3

makes it possible to use sources that have an energy dispersion of several electron-volts, as is the case for spark sources of high frequency (Bibl.7). In these sources, the spark jumps between two electrodes machined into the material to be analyzed (or oscillates between an electrode and a single-hole plate). The tapered shape given to the electrodes makes this type of source unsuitable for investigating metallographic specimens. In addition, the localization of the emission would constitute a problem rather difficult to solve.

A novel possibility of ionizing the matter composing a solid was developed in investigations of the phenomena of cathode sputtering. It has been known for long (Bibl.8) that a target struck by an ion beam will disintegrate in the form of neutral particles; however, recently various authors (Bibl.9 - 15) have demonstrated a different aspect of the phenomenon by showing that a considerable fraction cf the sputtering products are composed of ionized particles. These particles, known as secondary ions, are f^ ned from atoms present at the surface of the specimen. Thus, these particles are to the largest extent characteristic of the component elements of the specimen although the emission may be influenced, especially at the beginning, by the presence of adsorbed gases. A source making use of this emission of characteristic secondary ions of the target constituents is of dual interest; such a source permits the use of metallographic specimens and also makes it possible to localize the emission. In fact, the localization of secondary emission can be obtained by bombarding a small region of the plane surface of a solid specimen, by means of an "ion probe". However, without mentioning the difficulties resulting from producing an ion spot as fine as the electron spot used in the microanalysis by X-ray emission, this mode of localizing the emission of secondary ions does not eliminate the necessity of using scanning means for properly establishing the distribution curve of a given

4

element.

In the new microanalysis method, whose development is the main object of this work, the primary particles bombard a rather extensive area and the secondary ions emitted by the target are focused on an image of the object surface by means of a suitable corpuscular optical system, as is done for secondary electrons in emission microscopy. Here, a device resembling those used in mass spectrography is used for isolating, from all secondary ions that contribute to the formation of this image, those that are characteristic of a given element and that, because of this fact, produce the distribution curve of this element; the initial image is thus successfully resolved into as many "elementary images" as there are elements or isotopes of the same element on the bombarded surface.

Thus, secondary ion emission permits developing a microanalysis method which, to some extent, seems to avoid the drawbacks inherent to microanalysis by X-ray emission. However, it should be noted that sputtering is a destructive process presenting a certain disadvantage with respect to microanalysis by X-ray emission. However, this disadvantage is not as important as it would appear at first and may even have some interesting aspects. In fact, as the sputtering progresses, regions at greater depths are reached; this offers the possibility of studying the object at various levels and, specifically, at the level of its surface layer.

Primarily, we will discuss the principles of the setup developed by us, comprising basically three parts that have the purpose, respectively, of forming the ion image, of realizing its magnetic filtering, and of detecting the selected elementary image by means of a suitable device. This will be followed by a description of the experimental equipment designed by us and by a discussion of the experience gained in perfecting this design. Next, we will investigate

several characteristics of secondary ion emission, which will permit to define the analytical conditions. Finally, we will give several application examples.

CHAPTER I

ELEMENTS OF THE CORPUSCULAR OPTICS USED

1. Immersion Objective

Emission electron microscopy gives numerous examples (Bibl.16) of devices that permit the investigation of the surface of solid specimens by means of electrons emitted by the specimen. The use of ions instead of electrons merely means that, among the devices used, we must select those whose optical system is purely of the electrostatic type. Speaking in a general manner, this optical system comprises an accelerating section combined with a focusing section; these two parts can be either merged or separate. In the first case, we have a simple Johanson objective (Bibl.17) which had been investigated specifically by Septier (Bibl.18) while, in the second case, we have a composite objective whose magnetic variant has been studied mainly by Fert and Simon (Bibl.19, 20). We made use of both of these possibilities and finally decided on the composite object-ive which seems better suited to our specific problem.

a. Acceleration of Secondary Ions

The plane target M is bombarded by a beam of positive ions with an axis XX'. Let a positive secondary ion be expelled at an initial energy $e\varphi_0$ and leave the target at an angle α_0 with the normal to the surface. This secondary ion is accelerated by the uniform electric field E_0, existing between the target brought to the positive potential V and the plane electrode A parallel to M at the potential of the mass and at a distance Λ from the target (Fig.I).

6

The trajectory of the ion $(\alpha_0, e\varphi_0)$, emerging from a point P of the target, thus presents a parabola limited on one side in P by the plane M and, on the other side, by its intersection L with the plane A. From the optical viewpoint,
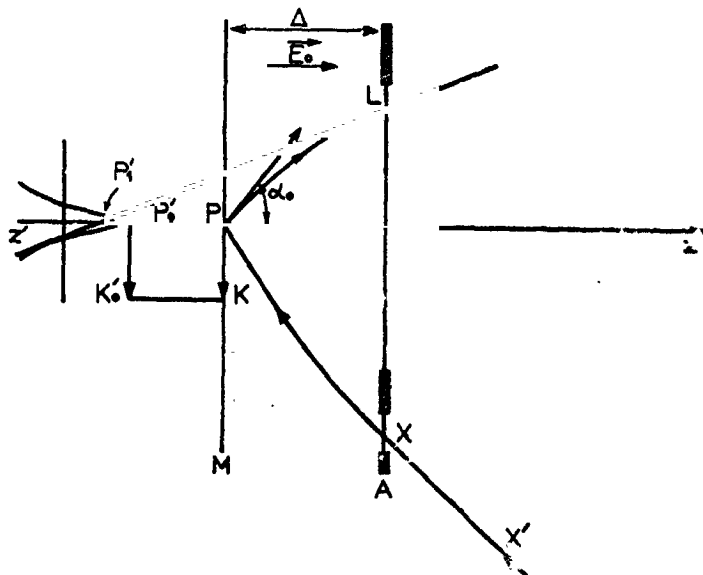
Fig.1

the process is the same as though the trajectory would continue over the tangent in L to the parabola. Let us now consider, for the same value $e\varphi_0$ of the initial kinetic energy, all trajectories emerging from P: The envelope of the tangents that form the extension of these trajectories is a caustic surface of revolution about the z'z axis perpendicular to the target in P. The intersection of this caustic by any plane containing z'z is symmetric with respect to z'z and presents an inflection point or cusp. This arrangement is quite frequent in optics; the system (M, A) is not stigmatic and gives, of the point P, a virtual image contaminated by aberrations.

These aberrations are due to the fact that the ions depart at nonzero initial energy; it is obvious that, for a zero initial energy, the aperture of the

7

beam emerging from P would be zero and the resultant image would be perfect.

The image K_0' of any point K of the target given by the system (M, A) presents the same characteristics as the image P_0' of the point P. In addition, P_0' and K_0' are located in the same plane perpendicular to z'z and at a mutual distance such that $KP = K_0' P_0'$. This raises the question as to the resolving power of the system (M, A).

a) <u>Limit of resolution</u>. The answer to this question is obtained by calculating the radius ρ_s of the aberration figure which surrounds the Gaussian image P_0' of P. The equation of a parabola $(\alpha_0,\ x\varphi_0)$ is written as

$$z = \frac{E_0}{4\,\varphi_0 \sin^2 \alpha_0}\, r^2 + \frac{r}{\operatorname{tg} \alpha_0} \tag{1}$$

in the system of rectangular coordinates $(\vec{P_r},\ \vec{P_z})$; see Fig.1.

Aside from this, the velocity component $v_0 \sin \alpha_0$ along the axis perpendicular to the electric field is retained. This will yield: $\sqrt{\varphi_0} \sin \alpha_0 = \alpha\sqrt{V + \varphi_0}$ where α is the angle of the tangent in L to the z'z axis. Moreover, it can be assumed that the initial energy of the secondary ions is small with respect to the accelerating potential; from this it follows that $\alpha \simeq \sqrt{\dfrac{\varphi_0}{V}} \sin \alpha_0$.

A simplified calculation then shows that the intersection P_1' of the tangent in L with the axis z'z is such that

$$\overline{P_1' P} = \Delta\left(1 - 2\sqrt{\frac{\varphi_0}{V}} \cos \alpha_0\right).$$

As soon as α_0 tends toward 0, the point P' will tend toward the point P_0', the Gaussian image of P, such that $\overline{P_0 P} = \Delta\left(1 - 2\sqrt{\dfrac{\varphi_0}{V}}\right)$. From this, we can derive the longitudinal aberration:

$$\overline{P_1' P_0'} = 2\Delta(1 - \cos \alpha_0) \sqrt{\frac{\varphi_0}{V}}.$$

The radius ρ_s of the aberration spot in the Gaussian plane (plane perpendicular

to z'z in P_0') will then be $\alpha \cdot \overline{P_1'P_0'}$, i.e.,

$$p_s = 2\Delta \frac{\varphi_0}{V} \sin \alpha_0 (1 - \cos x_0).$$

However, the optimum focusing plane is not located at P_0' but between P_1' and P_0', at a distance $\dfrac{1}{2} P_1'P_0'$ from P_0' (Bibl.21).

The radius of the aberration spot in this plane gives a measure for the resolution limit δ. We have

$$\delta \simeq \frac{\varphi_0}{E_0} \sin \alpha_0 (1 - \cos \alpha_0). \tag{2}$$

To improve the resolving power, we could either change the value of ω_0 $\sin \alpha_0 (1 - \cos \alpha_0)$ or else the accelerating field $E_\cdot$. The initial energy $e\omega_0$ of the secondary ions is a physical constant which is imposed. Consequently, an improvement in the resolving power can be obtained only by varying the angle $\alpha_\cdot$, i.e., by eliminating the fast particles that depart at too high an angle. However, it will be shown that the contrast diaphragm, introduced for this purpose, results in a reduction of the image luminosity; this means that one cannot go very far in this direction. It seems preferable to vary the electric field E_0, but also there we are limited by the requirements of illumination of the object.

b) _Illumination of the Object._ The target is bombarded by a beam of positive primary ions whose axis XX' makes an angle of 45° with the axis zz'; since the target is positively polarized, it repels these ions along a parabolic trajectory having the equation

$$z = \frac{E_0}{2\Phi_0} (r + r_0)^2 - (r + r_0) + \Delta \tag{3}$$

where $e\Phi_0$ is the energy of the incident ions and r_0 is the distance after which the primary ions "sense" the electric field. The incidence of the beam must be at an angle that permits retaining an ion density sufficient to operate under the conditions of cathode sputtering. If the geometric parameters of the para-

9

tolic trajectories are prescribed, any increase in E_0 will necessitate an increase in V and Φ_0 such that the ratio $\dfrac{V}{\Phi_0}$ will remain constant. Moreover, the secondary ions must then pass into the magnetic field of the mass spectrograph; for this reason, it is of no interest to impart too high an energy to these ions if one wishes to maintain a reasonable value for the radius of curvature of the trajectories in the magnetic field and, consequently, acceptable dimensions for the apparatus.

It also would be possible to increase E_0 by reducing the geometric dimensions (r_0 and Δ) and to retain the same angle of incidence on the target; however, it is obvious that there again we encounter a practical limit which it is difficult to exceed.

In part, these difficulties could be overcome by using, for the primary bombardment, neutral particles instead of positively charged particles; this would have the additional advantage of introducing the energy of the primary particles as a new parameter which could be readily influenced in such a manner that optimum bombardment conditions could be obtained.

<u>Divergent effect of the orifice O</u>. The secondary ions leave the accelerating space, comprised between the target M and the electrode A, through a circular orifice O made into the electrode A. The axis of this orifice coincides with the above-defined axis z'z. Perpendicular to the electrode A, the ions pass from a region of uniform electric field to a region of zero field. All along this path, the electric field retains symmetry of revolution about the axis z'z. The conservation of the electric induction flux results in the creation of a radial electric field E_r, correlated with the first derivative of the electric field on the axis E_z by the relation

10

$$E_r \cdot \quad \frac{r}{2}\frac{\partial E_z}{\partial z} \cdot \qquad\qquad (4)$$

It follows from this that the ion trajectories, while passing through the orifice, undergo a radial acceleration which causes them to diverge.

Calculations made under the assumption of a sharp disconti.uity of the electric field in the plane A (Bibl.20) shcw that, at the Gauss approximation, the effect of the orifice O is that of a divergent lens placed in the plane A at a focal length of -4Δ. The image of the point P is definitely a point P' located at $\frac{\Lambda}{3}$ behind the poi.it P; $\overline{PP'} = -\frac{\Lambda}{3}$; the image of a small segment KP is a segment K' P' such that $\frac{K'P'}{KP} = \frac{2}{3}$.

Let us also mention that, at the exit from the orifice C, the rays have an angular aperture equal to $\frac{3}{2}\sqrt{\frac{\alpha_0}{V}}$ sin α_0 in accordance with the Lagrange-Helmholtz relation; the exit pupil of the investigated system, which convention-ally is known as "crossover", is virtual and located in C_0 at 4Δ behind the plane of the electrode A at a diameter equal to 8Δ $\sqrt{\frac{\alpha_0}{V}}$.

Complete immersion lens. To observe the obtained virtual image, a con-vergent lens is required. In back of the electrode A, two electrodes E_1 and E_2 ·
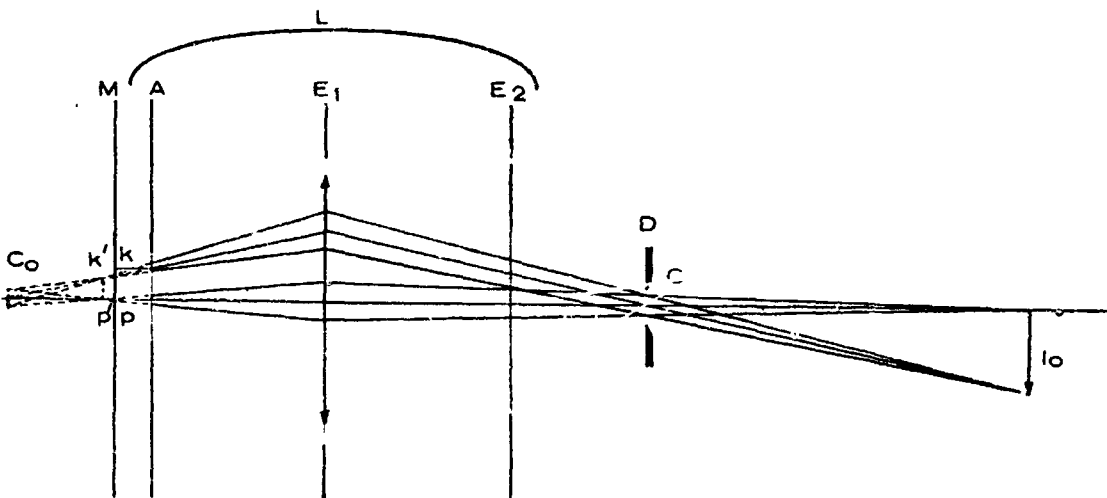

Fig.2

11

are arranged, consisting of circular diaphragms with an axis z'z, with the electrode E_1 being positively polarized and the electrode E_2 being at the mass potential. The unit (A, E_1, E_2) forms a three-electrode unipotential lens L.

The lens L, of the virtual image, gives a real image I_0 and, of the virtual crossover C_0, a real crossover image C. If we place a diaphragm D with a diameter d at the point C, we can eliminate those ions which, at a given initial energy, had been emitted at too high an exit angle α_0 or which, at a given exit angle, had been emitted at too high an initial energy $e\omega_0$; this makes it possible to influence the resolving power.

a) <u>Resolving power</u>. To be somewhat more accurate, let us imagine that we have placed the lens L in such a manner that it produces, of the crossover C_0, a real image at an enlargement of -1 (Fig.2). The ions, emitted at an initial energy $e\omega_0$ and at an exit angle α_0, traverse the plane of the crossover C at a distance ρ from the axis such that

$$\rho = \rho_M(\varphi_0) \cdot \sin \alpha_0 \quad \text{where} \quad \rho_M(\varphi_0) = 4\Delta\sqrt{\frac{\varphi_0}{V}}. \tag{5}$$

The contrast diaphragm permits the passage of all particles having an energy $e\varphi_0$ lower than or equal to an energy $e\varphi_{0m}$ whose value is given by the relation $2\rho_M(\varphi_{0m}) = d$. A portion of the ions with an initial energy above $e\varphi_{0m}$ is stopped, and only particles such that $\rho \leq \dfrac{d}{2}$ are passed, i.e., ions whose lateral velocity is below or equal to $\dfrac{d}{8\Delta}\sqrt{\dfrac{2eV}{m}}$. Referring to the expression for the resolving power, it is easy to demonstrate that δ begins increasing linearly as a function of $e\varphi_0$ up to a value of $\delta_M = \dfrac{\varphi_{0m}}{E_0}$. As soon as the influence of the diaphragm begins to manifest itself, δ decreases because of the fact that $\sqrt{\dfrac{2e\varphi_0}{m}}\sin \alpha_0$, which is the lateral component of the initial velocity, is limited to a maximum equal to $\dfrac{d}{8\Delta}\sqrt{\dfrac{2eV}{m}}$, which causes a decrease in the

12

factor $\sqrt{\epsilon_0}\,(1 - \cos \alpha_0)$ and thus of the expression $\dfrac{q_0}{E_0}\, \sin \alpha_0 (1 - \cos \alpha_0)$.

The curve plotted in Fig.3 describes the variation in the limit of resolution,
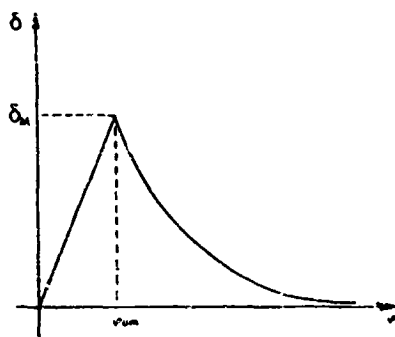as a function of the initial energy $e\epsilon_0$.

Fig.3

Thus, the diaphragm plays the role of an energy filter whose action in-
fluences only the "lateral energy" (denoting here by lateral energy the kinetic
energy corresponding to the lateral velocity). It follows from this that the
initial width of the energy dispersion band remains unchanged but that the energy
distribution at the interior of this band is basically modified. Nevertheless,
this "imperfect filtering" would be sufficient in absolute value to prevent an
influence of the fast particles on the resolving power provided that, during
passage through the orifice O and specifically within the lens L, the ions of
differing energy were focused in the same manner. Since, however, this latter
condition is not satisfied, it must be expected that chromatic aberrations will
contaminate the image I_0.

   b) <u>Filtering efficiency</u>. The proportion of particles eliminated by the
filter effect exerted on the initial lateral energies depends on the angular
distribution of the secondary ions. In order to define the possible course of

13

these phenomena, let us assume that the emission takes place in accordance with a law of the type of Lambert's law used in optics. The number dn of energies of ions with an energy $e\varphi_0$, emitted in a solid angle $d\Omega$ about the exit angle α_0, is given by the expressions $dn = \Re(\varphi_0) \cos \alpha_0 d\Omega$, where $\Re(\varphi_0)$ is the number of ions with an energy of $e\varphi_0$, emitted per area of the imaged field and per steradian. The number of particles emitted in the solid angle, limited by the half-angle cones at the vertex α_0 and $\alpha_0 + d\alpha_0$, thus will be

$$dn = 2\pi \mathcal{N}(\varphi_0) \sin \alpha_0 \cos \alpha_0 d\alpha_0.$$

In addition, in the diaphragm plane, the particles emitted in the investigated solid angle pass between two circles of radii ρ and $\rho + d\rho$. The area da of the circular corona, comprised between these two circles, has a value of $2\pi\rho d\rho$, i.e.,

$$da = 2\pi \rho_M^2 \sin \alpha_0 \cos \alpha_0 d\alpha_0. \tag{6}$$

We thus have

$$dn = 2\pi \mathcal{N}(\varphi_0) \cdot \frac{\rho}{\rho_M^2} \cdot d\rho = \mathcal{N}(\varphi_0) \frac{da}{\rho_M^2}. \tag{7}$$

Consequently, the crossover C is covered by a uniform density of particles.

The ratio of the number $N_D(\varphi_0)$ of particles allowed to pass by the diaphragm to the total number $N_T(\varphi_0)$ of emitted particles is equal to the ratio of the area of the diaphragm to the area covered by the crossover grouping the ions of energies $e\varphi_0$ in the plane C, i.e.,

$$\frac{N_D}{N_T} = \frac{d^2}{4\rho_M^2} = \frac{d^2}{64\Delta^2} \cdot \frac{V}{\varphi_0} \quad \text{whence} \quad \frac{N_D}{N_T} = \frac{\varphi_{0m}}{\varphi_0}. \tag{8}$$

c) <u>Chromatic aberration.</u> Chromatic aberrations are produced on passage through the orifice O and during focusing of the secondary ions by the lens L.

The orifice O, separating a region of uniform field E_0 from a region of

practically zero field plays the role of a divergent lens of a focal length -4Δ. The variation in slope $\Delta r'$ of a trajectory passing in the plane of the orifice at a distance r from the axis, is given by

$$\Delta r' = \frac{r}{4} \cdot \frac{V_0}{V + \varphi_0 \cos^2 \alpha_0} \cdot \qquad (9)$$

The divergence of the orifice O is less pronounced for fast ions emitted along the normal to the object. However, as soon as, at a given energy $e\varphi_0$, the exit angle α_0 increases, the divergence will increase up to a value independent of the initial energy at $\alpha_0 = \frac{\pi}{2}$; this is due to the fact that the velocity along the axis is then the same for all particles, no matter what their initial energy might be. Starting from the expression (9), we can calculate the radius ρ_1 of the chromatic aberration spot which surrounds an image point

$$\rho_1 = \frac{r}{3} \cdot \frac{\varphi_0}{V} \cdot \cos^2 \alpha_0. \qquad (10)$$

Two different types of chromatic aberration can be differentiated: chromatic aperture aberration (aperture defect) and chromatic field aberration (field curvature). A beam of trajectories emerging from the object will diverge more or less, after the orifice O, depending on the magnitude of the initial energy. Due to this fact, a chromatic aberration will appear on the image which depends on the aperture of the beam. This chromatic aberration will occur only at the center of the image. A trajectory emerging from the center of the object will pierce the plane of the orifice O at a distance $r = 2\Delta \sqrt{\frac{\varphi_0}{V}} \sin \alpha_0$ from the axis. Consequently, this trajectory will deviate the more from the axis /7 the greater the initial lateral velocity; however, the diaphragm imposes an upper limit on this velocity and causes the expression of the radius ρ_1 to become

$$\rho_1 = \frac{d}{12} \frac{\varphi_0}{V} \cdot \varphi_{0m}. \qquad (11)$$

15

Dividing this by the $\frac{2}{3}$ enlargement yields the value ρ_c of the aberration radius, reduced to the level of the object:

$$\rho_c = \frac{d}{8} \varphi_0 \frac{\varphi_{om}}{V}.$$ (12)

The variation in the divergence of the orifice O with the energy of the ions traversing this orifice also leads to the introduction of enlargement differences on the image. The degree of aberration will increase with the distance h from the imaginary point at the center of the object. Naturally, this chromatic field aberration is superposed by the chromatic aperture aberration which has been calculated above. Let ℓ_1 be the chromatic shift at the level of the image; since r = h, we have

$$\ell_1 = \frac{h}{3}\frac{\varphi_0}{V} \qquad \text{i.e.,} \qquad \ell_c = \frac{h}{2}\frac{\varphi_0}{V} \quad \text{on the object.} \qquad (13)$$

To give an order of magnitude, let us imagine a lens provided with a diaphragm of 0.5 mm diameter, limiting the lateral energy of the ions to 1 ev. As values for the other parameters, let us take Δ = 3.75 mm and V = 3750 v, which will give an extracting field $E_0 = 10^4$ v/cm and lead to a limit of resolution δ of the order of microns. For values of φ_0 of the order of 10 v, we obtain $\rho_c \simeq$ $\simeq$ 0.15 μ at the center of the image and $\ell_c \simeq$ 0.2 μ along the edge of a field of 0.3 mm diameter. These aberrations have a direction opposite to that introduced by the lens L but, as demonstrated below, these latter are of a higher order of magnitude.

The lens L, for ions whose initial energy varies by ΔV, presents a variation of Δf of the focal length given by $\frac{\Delta f}{f} = K \cdot \frac{\Delta V}{V}$, where K is the chromatic aberration coefficient of the lens; for a lens of the type used, K is of the order of 3.5 (Bibl.21). Taking into consideration the $\frac{2}{3}$ enlargement produced by the orifice O, the radius ρ_c of chromatic aberration at the level of

16

the object will be

$$\frac{2}{3}\rho_c \simeq K.\alpha./. \frac{\Delta V}{V}$$

where α is the half-aperture of the beam on the object side:

$$\alpha = \frac{2}{3}\sqrt{\frac{\varphi_0}{V}}.\sin \alpha_0 = \frac{3d}{16\Delta}.$$

Defined, we obtain

$$\rho_c = \frac{9}{32}.\frac{d}{\Delta}.K\frac{\Delta V}{V}./. \qquad (13)$$

This is the aberration at the center of the observed field. There also exists a chromatic field aberration produced by the variation in enlargement of the image I_0 whenever the initial energy of the secondary ions varies. The ions of differing energy, emerging from a point of the object located at a distance h from the axis and leaving the object perpendicularly, enter the lens under an inclination of $\alpha = \frac{h}{4\Delta}$ but do not all pass through the center of the crossover; their trajectories intersect the axis in points located at $2f + 4\Delta f$ from the center of the lens L. This results in a chromatic shift l_1 of each image point, with the fast ions deviating less from the axis than the slower ions. This displacement reduced to the level of the object, taking the $\frac{2}{3}$ enlargement given by the orifice O into consideration, will be

$$\frac{2}{3}l_c \simeq 2K.\alpha./. \frac{\Delta V}{V}$$

i.e.,

$$l_c \simeq 3K.\frac{h}{4\Delta}.\frac{\Delta V}{V}./. \qquad (14)$$

To give an order of magnitude, let us take f = 10 mm as the focal length of the lens L. The value of ΔV is more difficult to determine since, depending on the potential applied to the central electrode, it is not the ions of the same energy that are focused at a focal length f. For example, if the initial

energy band, covered by the ions, is limited to 10 ev, the excitation of the lens L can be controlled in such a manner that the focusing takes place at a focal length f for ions whose energy takes any of the values of this band. The selection of this value depends on the energy distribution of the ions after the diaphragm; to fix the concept, let us take the mean of the band, namely, $\Delta V = 5$ v. At the center of the field we will then have an aberration of the radius $\rho_c \simeq 1.7\mu$. Along the edges of a field of 0.3 mm diameter, we must use a value of $\Delta V = 10$ v since ℓ_c represents the distance between the slowest and the fastest particles: $\ell_c \simeq 2.8\mu$. If desired, these values can be corrected by the aberrations given by the orifice O, yielding: $\rho_c \simeq 1.6\mu$ and $\ell_c \simeq 2.6\mu$.

The chromatic aberrations may seem prohibitive, specifically when considering that the initial energies may have several hundreds of volts. In fact, the magnetic prism which separates the secondary ions in accordance with their mass, also isolates an energy band for ions of the same type. In addition, we demonstrated above that only a fraction $\dfrac{\varphi_{0\,\blacksquare}}{\varphi_0}$ of particles with an energy φe_0 passes through the diaphragm, so that the chromatic aberrations discussed here appear in the form of halos which become increasingly faint as the energy $e\varphi_0$ increases. Although these halos interfere much less with the optical resolving power than would be expected from their calculated numerical values, they still may reduce the accuracy of the analysis. Let us mention also that the aspect of the aberration figure changes with the adjustment or focusing of the lens. Finally, a calculation of the aberrations at the level of the crossover shows that their effects on the filtering are negligible.

The immersion objective, described above, represents a lens system which, because of the fact that the optics used is electrostatic, focuses in the same manner all ions, independent of their charge-to-mass ratio e/m. All the ions,

/18

18

no matter what their charge or mass might be, thus participate in the same way in the formation of an enlarged image of the object surface. For observing this ion image, it would be easiest to use a fluorescent screen. Unfortunately, the available fluorescent screens have an extremely low sensitivity for ions and specifically for heavy ions which travel at relatively low velocities; in addition, metallic ions, for example, rapidly contaminate the phosphors by coating them with a layer opaque to ions. Finally, the fluorescent substances generally are insulators which means that they become positively charged by retaining the ions and, under their impact, emitting secondary electrons which results in a migration of the image and breakdowns. We were able to bypass this difficulty by using an image converter of a type suggested by Mollenstedt (Bibl.22) and experimentally investigated by Jouffrey (Bibl.23).

2. Image Converter

a. Principle

The principle of the image converter is as follows: The real ion image is formed on the highly polished cathode of an emission electron lens. The impact of the ions on this cathode produces an emission of secondary electrons which are then accelerated and focused by the lens into an electron image which can be observed on a fluorescent screen. As shown in the sketch in Fig.4, the pencil of ion trajectories passes through the hole T_1 pierced in the fluorescent screen E and converges at a point B_1 of the cathode K. This cathode, which is negatively polarized with respect to the anode A_n, repels the secondary electrons. A Wehnelt electrode W, placed between K and A_n and brought to a potential close to that of the cathode, curves the equipotentials of the electric field thus creating a radial field of revolution which focuses the electrons emitted

by B_1 in a point B_1' of the fluorescent screen.

The image converter reproduces the ion image, outlined on the cathode, as an enlarged electron image on the fluorescent screen; thus, this converter can serve as a "projection lens", except that then, in the final enlargement, the contraction of the ion image must be taken into consideration.

Contraction of the ion image. The ions, arriving in the converter, are attracted by the cathode, and the arrangement of the equipotential lines produces a certain convergent effect. This means that, on the one hand, to obtain
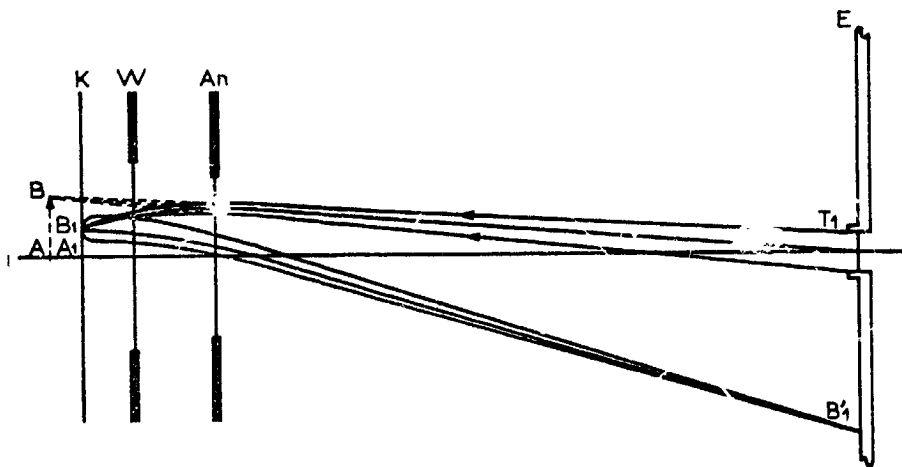
Fig.4

a focused ion image on the cathode it is necessary to form the initial image in back of this cathode and, on the other hand, that the ion image is contracted. Thus, the image AB is reduced to A_1B_1 by a factor k which depends on the ratio q of the energy of the ions on arrival at the cathode to their energy before entering the converter.

The values obtained experimentally by Jouffrey give an order of magnitude for this phenomenon: A ratio q of the order of 2 will lead to a contraction

of 1.8 while a ratio q of the order of 4.5 will produce a contraction greater than 4.5.

The electron image, observed on the fluorescent screen, is not equally distinct over the entire field. This is due to the field curvature of the con-verter, which introduces a different collimation for the center and for the edges of the image. This can be eliminated by replacing the plane cathode by a concave cathode having a spherical form. The radius of curvature is adjusted such that the image will be distinct over the entire observed field, for one and the same focusing.

In addition, the electron image is affected by so-called pincushion dis-tortion which can be readily eliminated since it has a direction opposite to that imparted by the contraction in the converter to the ion image, so that - at a suitable voltage ratio - the three following distortions are exactly compen-sated: pincushion distortion of the emission lens; barrel distortion of the ion image on traversing the converter; and pincushion distortion of the electron image.

Let us also note that the cathode must be so highly polished that its structure does not interfere with the electron image. In addition, the enlarge-ment of the ion images, which are to be observed on the screen, must be so ad-justed that the resolving power of the converter does not place a limit on the sharpness of the ion image.

The use of such a converter, because of the considerable luminosity gain it permits, makes an observation of ion images of extremely low intensity pos-sible. Thus, we can obtain a direct reproduction of the image I_0 given by the immersion objective. This is the main goal of a series of preliminary experi-ments which also will contribute to the justification of the microanalysis

process we intend to develop.

3. Preliminary Experiments

a. Mass Spectrograph Analysis

As a first step, it is necessary to identify the exact nature of the ions
extracted from the target. Primarily, we used an immersion lens diffe·ing from
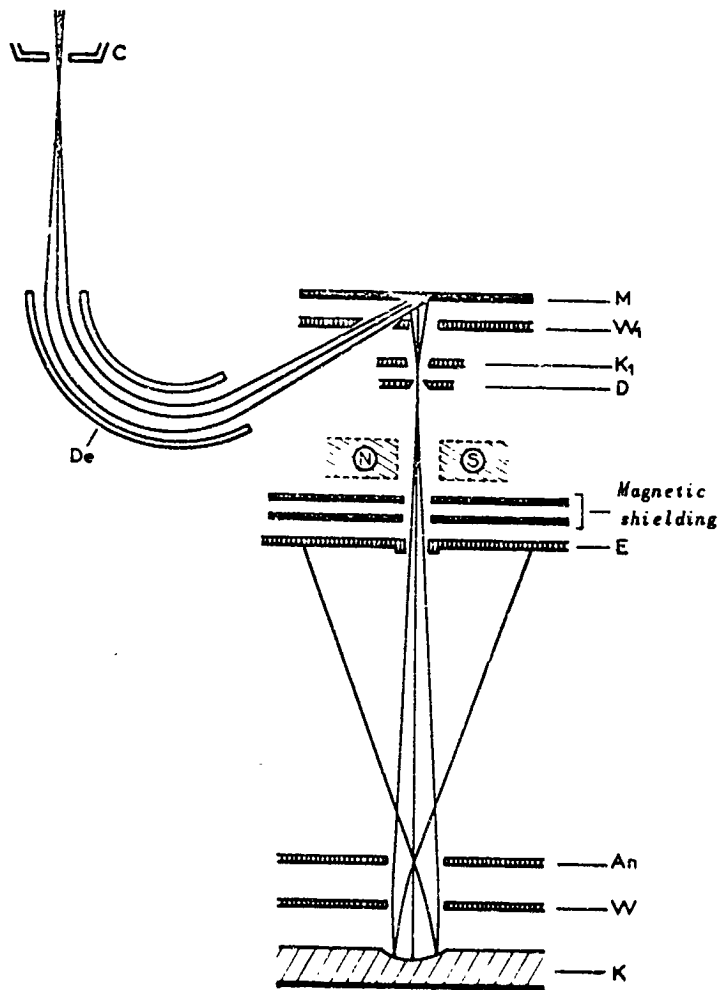
Fig.5

that described above. The immersion objective shown in Fig.5 is a simple model. This objective comprises a plane target M and a Wehnelt electrode W_1, brought to the same positive potential (several kilovolts), and a grounded electrode K_1; the Wehnelt W_1 is provided with a channel which allows passage of the primary beam. The accelerating and focusing functions are no longer clearly separated as had been the case in the above-described lens. The Wehnelt, inserted between the object and the cathode K_1, curves the equipotential lines which permits a focusing of the ions emitted by the target. In addition, due to an electric screening effect, the presence of the Wehnelt weakens the extracting field at the surface of the object. To avoid such weakening of the electric field, we will use the strong-field lens described on p.7 in our final design. Let us also note that a diaphragm D, placed at the crossover, will limit the "lateral energy" of the ions to a few electron-volts.

The immersion objective is placed at the entrance of a mass spectrograph; the diaphragm D, which limits the crossover, serves as entrance slit. This made it possible to separate the characteristic secondary ions from the primary ions diffused by the target at a low initial energy and to record, for example, the spectrum shown in Fig.6 which corresponds to the emission of Al^+ ions by an aluminum specimen bombarded with argon ions.

These experiments have shown that characteristic secondary ions exist at a relatively large proportion in the sputtering products. In addition, during /10 these experiments, we investigated various elements such as copper, nickel, aluminum, magnesium, and beryllium; on all these substances we were able to observe the emission of characteristic ions. This, together with the data contained in the literature concerning the emission of tantalum, molybdenum, silver, germanium, and silicon, indicates that the emission of secondary ions

23

is not a phenomenon limited to a few elements and seems to promise that the method can be generalized. In addition, the emission of light metals is particularly intense, which is of advantage since it is exactly for light elements

27

40

15
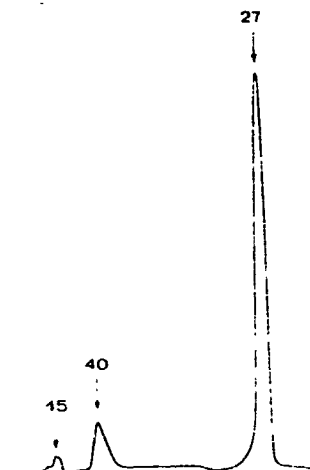
Fig.6

that the use of an electron microprobe is so precarious.

b. Reproduction of an Ion Image

In a second series of experiments, we had the purpose of directly reproducing the image I_0 of the object surface, given by the emission lens. Toward this end, we devised the experimental setup shown schematically in Fig.5. An electrostatic deflector De, composed of two coaxial cylinders, deflects by 120° the argon ion beam emitted by the gun C and directs it toward the object M. These primary ions arrive at the target with an energy of the order of 4 Kev. The ion image I_0 is observed by means of an image converter whose optical axis coincides with that of the emission lens. The final electron image is received on the fluorescent screen E, which is pierced at its center by a hole to permit

passage of the secondary ion beam which transports the image I_0. Immediately below the emission lens, there is a permanent magnet which permits application of a magnetic field perpendicular to the axis of the secondary ion beam. This magnet slides in a plane parallel to that of the fluorescent screen; this motion can be controlled, during operation, from outside the vacuum enclosure. The magnetic field deflects the ion trajectories in accordance with an angle proportional to the square root of the specific charge of the particles that pass through the air gap. Between the magnet and the fluorescent screen, there are two soft-iron disks having a hole at their center for passage of the ion beam and ensuring magnetic shielding of the fluorescent screen, in such a manner that the electron image will be insensitive to the position of the magnet.
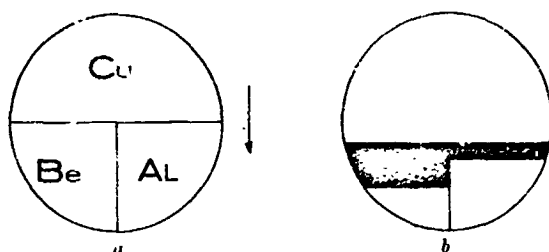
Fig.7

Since the Wehnelt and the target are electrically coupled, the adjustment of the image I_0 on the cathode of the converter is done by increasing or decreasing the distance between object and Wehnelt. By varying the polarity of the Wehnelt W of the converter, the electron image on the fluorescent screen can be focused. These various alignments are done while the magnet is detached so as to prevent its influence on the secondary ion beam. The introduction of the magnet produces a fantail spreading of the trajectories; each "rib" of this fan is traversed by ions of different type, and the image I_0 is resolved into as many images as there are ions of different type in the initial beam.

To permit convenient observation of the image displacement, we studied an object formed by the juxtaposition of a half-disk of copper with a quarter-disk of beryllium and another quarter-disk of aluminum, arranged as shown in Fig.7a. The orientation of the object in its plane is such that, as soon as the magnet is inserted into the ion path, the deviation of the trajectories will cause a motion of the images in direction of the arrow (Fig.7a). The image displacement is inversely proportional to the square root of the mass of the ions that participate in formation of the image; the lightest elements are thus more strongly deflected, which results in the aspect sketched in Fig.7b. In addition, while evaluating the displacements of these images, we were able to verify that actually an emission of Cu^+, Al^+, and Be^+ ions was taking place. Also other types of objects were investigated: For example, we deposited a few fine crystals of rock salt on a tantalum plate and observed small luminous and highly brilliant islets or regions, corresponding to the emission intensity of Na^+ ions.

This second series of experiments furnished data which later proved /11 highly useful. On the one hand, from the quality of the images it can be deduced that the ions originate in the specimen surface itself rather than during a later ionization of the particles removed in their neutral state. On the other hand, the observed images have a luminosity sufficient for convenient observation, at a magnification of the order of 100. Despite the fact that we used simple experimental means, these experiments show that it is possible to obtain images representing the distribution of an element present on the surface of a given specimen. However, in these same experiments we always ended up with a certain overlap of the various images; it is obvious that this device is no longer suitable if complete separation of the images is desired. The technique used in mass spectrography suggests the utilization of the angular focusing

properties of sectorial magnetic fields for forming, from the crossover of the

emission lens, a real crossover image where only ions of the same type will

converge. A slit, placed at this level, makes it possible to isolate the se-

lected component in the initial beam, for a given value of the magnetic field.

However, in microanalysis a simple selection of ions in accordance with

their mass is not sufficient since such an analysis must also give the local

distribution of an element at the surface of a given object. Therefore, it will
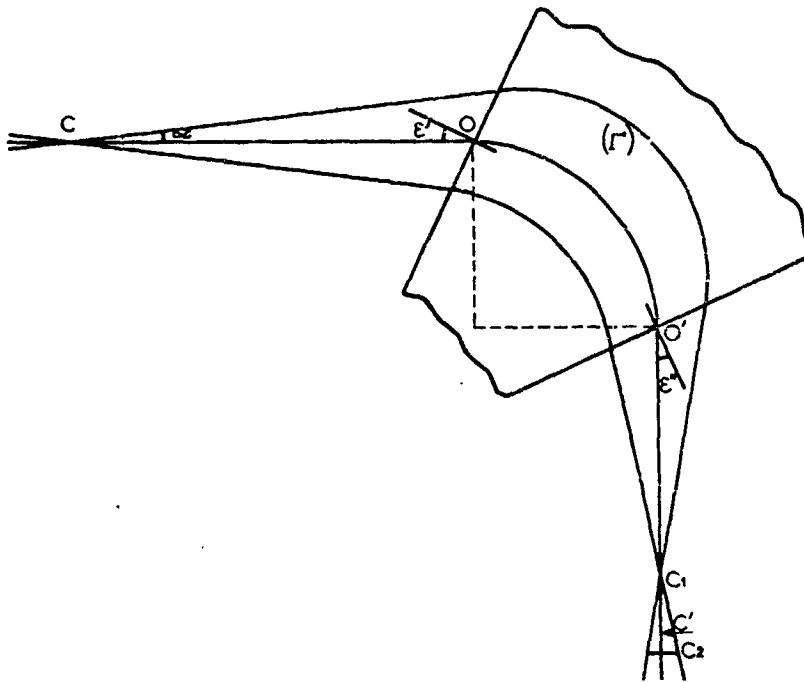

Fig.8

be necessary to investigate the optical properties of sectorial fields in more

detail so as to know what becomes of the initial image I_0 during separation of

the elements.

4. Optical Properties of the Magnetic Prism

In his thesis (Bibl.24) Cotte gave a general theory on orthogonal systems, i.e., on systems in which the mean trajectory of the particles remains in a plane which is the symmetry plane for the electric potential and for the magnetic induction. More recently, Hennequin (Bibl.25) made an experimental study of the optical properties of sectorial fields, i.e., of systems formed by a uniform magnetic field parallel to the median of the dihedron which limits the region of space over which it extends. Such a field is practically realized in the air gap of constant width of an electromagnet. The pole pieces have plane faces perpendicular to the plane of symmetry of the air gap (which, in turn, is also a symmetry plane for the magnetic field) and delimit an angular sector in which the field is localized (see Fig.8).

a. Properties of the First Order

The composition of the ion beam passing through the crossover object C is heterogeneous. Under the action of the uniform magnetic induction, the ions follow circular trajectories whose radius is equal to $143.6\sqrt{\dfrac{M}{n}}\cdot\dfrac{\sqrt{V}}{B}$ where M is the atomic mass of the ionized element, n is the number of elementary charges carried by one ion, V is the accelerating potential in volts, and B is the magnetic induction in gauss. In a device where only the ions that traverse a circle of given radius are collected and where the potential V is fixed, ions of a given type are selected by regulating the magnitude of the magnetic induction. Thus, an optical study of the magnetic prism can be made, without interfering with the generality of the reasoning, by assuming that the beam which passes through C is composed of ions having identical mass, charge, and velocity. The

case in which the last condition is not satisfied will be specifically investi-
gated below. Consider a homogeneous beam, monokinetic and emerging from C,
which obliquely strikes one of the pole faces, travels within the air gap along
a circle of radius R, and emerges obliquely through the other face. The mean
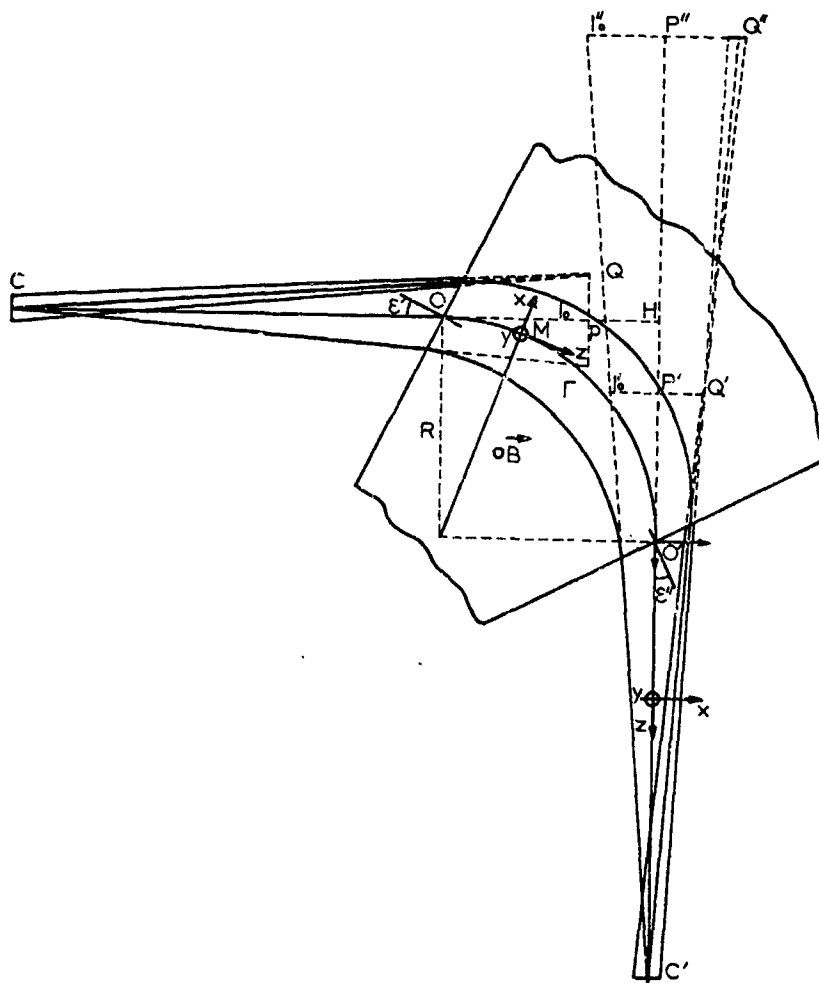

Fig.9

trajectory of this beam remains in the plane of symmetry or in the radial plane.

a) <u>Position of the focal lines, stigmatism.</u> The trajectories emerging

from C, whose initial velocity is contained in the radial plane or in the

first principal section, remain in this plane and, after rotation in the magnet, converge (at approximately the second order with respect to the aperture angle of the beam emerging from C) in a point C of the mean trajectory.

The trajectories emerging from C whose initial velocity is contained in a plane perpendicular to the plane of symmetry, are lowered toward the radial plane at the entrance and exit of the air gap, because of their oblique incidence and emergence. They remain within a cylindrical surface, known as the second principal section, whose generatrices, perpendicular to the radial plane, have their footpoint on the mean trajectory; after rotation within the magnet, these trajectories converge at approximately the second order in a point C_2 of this same trajectory.

A study of the total of all ion trajectories emitted from C and contained within a cone of revolution with a vertex half-angle α, clearly shows that, at approximately the second order in α, the trajectories after rotation within the magnet rest on two focal lines, one of which is radial and parallel to the magnetic field passing through C_1 while the other is axial and perpendicular to the field passing through C_2. The magnetic prism which constitutes the magnet thus represents an astigmatic system. However, by modifying the angles ϵ' and ϵ'' (Fig.8) at which the mean ray strikes and leaves the magnetic field, it is possible to make the two focal lines coincide in a point C and thus, at approximately the second order, obtain stigmatism of the prism, a stigmatism which the nongaussian optics limits to the single pair of points C and C'. This has primarily the result that the ion trajectories which initially had converged in a point of the image I_0 (which now plays the role of the virtual object for the prism), after rotation in the magnet, are based on two small virtual focal lines,

30

one being radial in I'_0 and the other axial in I'_0 (see Fig. 9).

Before going further, let us define several notations. The mean trajectory, (Γ) intersects the entrance face of the prism in O, the exit face in O', and rotates within the magnet along a circular arc $\widehat{OO'}$ measuring $\frac{\pi}{2}$ radians.

The ion trajectories are reduced to a system of curvilinear axes (x, y, z) where z denotes the curvilinear abscissa of a moving point M on (Γ), with the direction of increasing z being that of the motion, while (x, y) are coordinates following the principal normal and the binormal to the curve (Γ) in M.

Let us assume an object point S whose position on the axis CO is defined by $\zeta = \overline{OS}$ ($\zeta > 0$ if S is virtual and $\zeta < 0$ if S is real); at about the second order, this object point corresponds to an image point S_1 in the first principal section and to an image point S_2 in the second principal section. Here, S_1 and S_2 are located on the axis $O'C'$ and are defined by $\zeta'_1 = \overline{O'S_1}$ and $\zeta'_2 = \overline{O'S_2}$ (the quantities ζ' are positive for real images and negative in the opposite case). At the indicated order of approximation, Cotte's theory permits calculating the position of these points by the formulas: /13

$$-\frac{\zeta'_1}{R} = \frac{-\sin\Phi + \frac{\cos(\Phi + \varepsilon')}{\cos\varepsilon'}\frac{\zeta}{R}}{-\frac{\cos(\Phi - \varepsilon'')}{\cos\varepsilon''} - \frac{\sin(\Phi + \varepsilon' - \varepsilon'')}{\cos\varepsilon' \cdot \cos\varepsilon''}\frac{\zeta}{R}} \qquad (15)$$

$$-\frac{\zeta'_2}{R} = \frac{-\Phi + (1 + \Phi\,\mathrm{tg}\,\varepsilon')\frac{\zeta}{R}}{-(1 - \Phi\,\mathrm{tg}\,\varepsilon'') + (\mathrm{tg}\,\varepsilon' - \mathrm{tg}\,\varepsilon'' - \Phi\,\mathrm{tg}\,\varepsilon'\,\mathrm{tg}\,\varepsilon'')\frac{\zeta}{R}} \qquad (16)$$

where Φ is the angle about which the trajectories rotate in the magnet, having here a value of $\frac{\pi}{2}$ radians. To retain, at the exit from the magnet, the symmetry of revolution of the beam and thus to avoid distortion aberrations, we used a symmetric device where the angle of incidence $-\varepsilon'$ is equal to the exit

31

angle ϵ'' $(-\epsilon' = \epsilon'' = \epsilon)$. Equations (15) and (16) then become

$$-\frac{\zeta_1'}{R} = -\frac{-1 + \mathrm{tg}\,\epsilon\,\dfrac{\zeta}{R}}{-\mathrm{tg}\,\epsilon - (1 - \mathrm{tg}^2\,\epsilon)\,\dfrac{\zeta}{R}} \tag{17}$$

and

$$-\frac{\zeta_2'}{R} = \frac{-+\dfrac{\pi}{2}\left(1 - \dfrac{\pi}{2}\mathrm{tg}\epsilon\right)\dfrac{\zeta}{R}}{-\left(1 - \dfrac{\pi}{2}\mathrm{tg}\,\epsilon\right) - \left(2\,\mathrm{tg}\epsilon - \dfrac{\pi}{2}\mathrm{tg}^2\,\epsilon\right)\dfrac{\zeta}{R}} \tag{18}$$

Thus, symmetric focusing is obtained for an angle ϵ such that $\tan \epsilon = \dfrac{1}{2}$; the positions of C and C' will then be

$$-\zeta = \zeta_1' = \zeta_2' = 2R.$$

b) <u>Theoretical magnet, real magnet.</u> Equations (15) and (16) were derived by Cotte under the hypothesis stipulating that the magnetic field undergoes an abrupt discontinuity perpendicular to the pole pieces. Ampère's theorem demonstrates that this discontinuity is accompanied by the appearance of a magnetic field H_t perpendicular to the pole face and parallel to the radial plane. This field exists only at the entrance and exit of the prism where, because of the oblique incidence and emergence of the beam, it produces focusing of the trajectories in the second principal section. The field H_t is connected to the derivative of the field $H_y(z)$ on the axis by the relation $H_t = -y\dfrac{\partial H_y(z)}{\partial z}$.

In the hypothesis of a discontinuity of H_y, the quantity $\dfrac{\partial H_y(z)}{\partial z}$ becomes infinite which is physically completely illogical but is quite convenient for the calculation since $\dfrac{\partial H_y}{\partial z}$ does not enter except by integrals extended over the thickness of the "passage layer" which is assumed to be infinitely thin, separating the region of the zero field from the region of the air gap where the uniform field H_y^0 prevails. This case is analogous to the case encountered in calculating the trajectories by Ganz's method. In fact, the magnetic field

32

"leaks" to outside the air gap and, depending on the data given by Septier
(Bibl.18b) for example. retains a considerable magnitude over a distance of
several lengths of the air gap beyond the magnet. In the case of a real magnet,
this causes the trajectories to rotate before their entry into the air gap and
after their exit; this will modify the focusing in the first principal section.

In addition, since the passage layer presents a certain "thickness", it be-
comes necessary to define the exact value of $\frac{\partial H_z}{\partial z}$ as a function of z if the
focusing in the second principal section is to be calculated. Consequently,
Cotte's formulas are rigorously valid only in the limiting case of an infinitely
narrow air gap.

With a real magnet, we also obtain a focusing of the beam, emerging from C,
in the two principal sections; however, as experimentally established by Henne-
quin (Bibl.25), this focusing takes place for values of ε and of ζ which are no
longer those indicated by the directly applied theory. However, by arranging
the pattern of the focal-line position for various angles, Hennequin was able to
demonstrate that the overall results could be simply interpreted by applying
Cotte's theory to an "equivalent" magnet rather than to the real magnet.

The characteristics of such an equivalent magnet can be directly determined
by experiment. It is necessary to define the values of the angle ε and the
position of C, which will yield the conditions of symmetric focusing. In this
case, C must be located at a distance 2R from the entrance face of the equiva-
lent magnet. The axes CO and O'C' are orthogonal and intersect in H (see Fig.9)
so that the radius of curvature of the equivalent magnet will be such that CH =
= 3R. By design, OH is known and by experiment CO is measured, so that it is
relatively easy to calculate the equivalent radius of curvature. In addition,
if Cotte's theory is applicable to the equivalent magnet, we must necessarily

have $\tan \epsilon = \dfrac{1}{2}$.

It is also easy to see that the tangent of the angle of incidence to the real magnet will be greater than $\dfrac{1}{2}$. In fact, eqs.(17) and (18) show that ζ_1' is an increasing function of $\tan \epsilon$ while ζ_2' is a decreasing function. Since the leakage fields cause the beam to rotate before it enters the region of strong gradient $\dfrac{\partial H_y}{\partial z}$ where the axial focusing takes place, the beam will arrive in this region at an angle of incidence ϵ lower than predicted, thus causing ζ_2' to increase; ζ_1' also increases but much less than ζ_2' and for different reasons (so as to retain a deflection at 90°, the radius of mean curvature of the trajectories is greater than in the case of a magnet without leakage field, which /14 causes an increase in the geometric parameters that depend on the radius of curvature).

On increasing ϵ, the radial convergence will increase while the axial convergence will decrease; thus, it is possible to find a value of ϵ, higher than that predicted by the theory, for which stigmatism will be realized.

The use of an equivalent magnet permits to extend the simple calculations of the Cotte theory to the practical domain. In addition, the aberration calculations developed in the hypothesis of the equivalent magnet do not require an exact knowledge of the leakage field and lead to aberration coefficients whose values are comparable to the results obtained by Hennequin (see Appendix I). Therefore, it will be possible to base our further developments on the hypothesis of the equivalent magnet.

b. Chromatism of the Prism. Chromatic Focal Line

Let, at the point C, be located the crossover of the immersion objective limited by a diaphragm D of diameter d. Let any ion trajectory pierce the plane

of the diaphragm at a point (x_0, y_0). The image I_0 is located at a distance L from C. The trajectories which will converge at the point Q of the image I_0 form a conical pencil which has its nadir on the diaphragm D. The projections of the axis of this pencil onto the planes (x, z) and (y, z) form, respectively, the angles α and β with the z axis. The diameter d of the diaphragm is viewed from any point of the image under an angle of $2\gamma = \dfrac{d}{L}$ (see Fig.9).

The prism gives a real image C' of the crossover C at a magnification of -1 whose geometric dimensions are enlarged by second-order aberrations in α and β. Consequently, the selection slit, placed at this level, must have a width equal to the real dimension of the crossover C' if uniform illumination of the entire image field is desired.

In addition, the prism gives an astigmatic image of the point Q since, at the exit from the magnet, the pencil of rays which was to converge in Q thins out into two focal lines, one radial line Q' and another axial line Q'' (see Fig.9). Once the astigmatism is corrected, the quality of the image after rotation in the prism will be limited only by aberrations of the second order in α, β, x_0, and y_0, provided that the particles entering the prism had been monokinetic. Moreover, it is known that the secondary ions present a certain velocity heterogeneity to the emission, which already limits the resolving power of the immersion objective. Until now, we have made use of the dispersive properties of the prism only for separating the ions in accordance with their mass. It is obvious that these properties are useful also for dispersing the ions in accordance with their velocity. The selection slit permits passage of ions whose energy extends over an interval of a width of $e\Delta V$ which, because of the dispersion introduced by the prism, will result in a chromatic defect on the image, independent of the previously defined geometric parameters. Before

discussing the geometric aberrations it is therefore absolutely necessary to check whether the "chromatism" of the prism might not be cancelable.

   a) <u>Dispersion of the prism. Chromatic focal line</u>. Consider, for example, ions which, before entering the prism, travel along the axis CO at an energy oscillating between eV and $e(V + \Delta V)$. Wit 'n the prism, these ions follow circular trajectories of a radius R and $R + \Delta R$. At the exit from the prism,
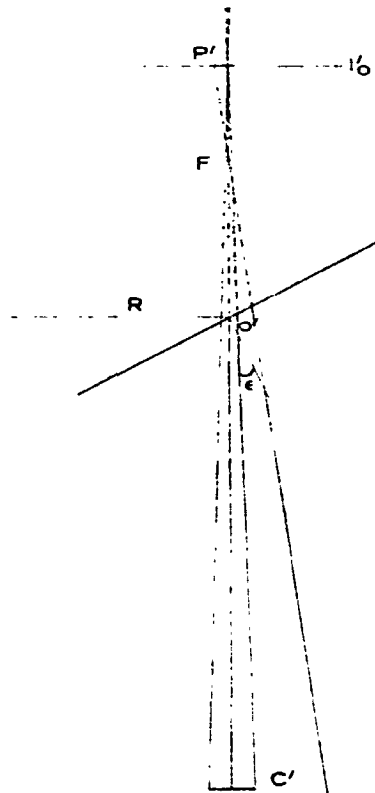

Fig.10

the trajectories spread in a fantail in the radial plane, with their base on a caustic tangent to the axis $O'C'$ in F; apparently, these originate, at approximately the second order in $\frac{\Delta V}{V}$, from the point F (Fig.10).

   As soon as the velocity of the ions varies, the rays resulting from the

dispersion of the ray CO will rotate about F similarly to the rays of a beam rotating about a geometric focal line as soon as the angle of the beam is widened. By analogy, one could speak here of a "chromatic focal line" in F. Calculations and experiments [(Bibl.25), Appendix I] show that the fantail of the trajectories spreads by an angle at the vertex of $\frac{3}{2} \cdot \frac{\Delta R}{R}$, since the /15 position of the vertex F is such that $\overline{O'F} = -\frac{2}{3}R$.

The chromatic dispersion of the prism in the plane perpendicular in C' to the axis $O'C'$ can then be calculated quite simply: The fantail of the trajectories, in this plane, intercepts a segment of a straight line whose length $\mathcal{l}$ is $\frac{3}{2}\frac{\Delta R}{R} \cdot C'F$. Since $O'C' = 2R$, we have $\mathcal{l} = 4\frac{\Delta R}{R}$. In addition, because of $\frac{\Delta R}{R} = \frac{1}{2} \cdot \frac{\Delta V}{V}$, let $\mathcal{l} = 2R\frac{\Delta V}{V}$.

b) <u>Chromatic defect on the image</u>. To permit a simple evaluation of the defects introduced on the image by the chromatism of the prism, let us limit the calculation to trajectories contained in the radial plane. Consider, for example, the point P of the image I_0 located on the axis CO, where the beam of half-aperture γ converges. At approximately the second order in γ, the point P has as image the point P' of I_0' located on the axis $O'C'$. The size of the "chromatic blur" surrounding P' is $\frac{2}{3} \cdot \frac{\Delta R}{R} FP'$, i.e., $\frac{2}{4} FP' \frac{\Delta V}{V}$ (see Fig.10). The image of P, given by the prism, is subject to a first-order aberration in $\frac{\Delta V}{V}$, which thus must be eliminated. For this, it is sufficient to cancel FP', i.e., to place P in such a position that its conjugate P', given by the prism, will be located in F.

This will result in an "achromatic point" about which the rays rotate, due either to the angular aperture of the beam or to the heterogeneity of velocity of the secondary ions.

If we now consider the trajectories contained in the second principal sec-

tion, the above statements will apply also to their projections onto the radial plane. In addition, since the convergent effect of the prism acts only when traversing thin passage layers, the dispersion enters only at the second order over the intermediary of the terms in $\gamma \frac{\Delta V}{V}$. The trajectories contained, on leaving, within this second principal section thus rotate about the chromatic focal line, perpendicular in F to the radial plane.

Let us finally consider the total beam which converges in P. Equation (17) will yield the position that must be occupied by the point P to have the radial focal line coincide with the chromatic focal line. It will be found that, for $\zeta_1' = -\frac{2}{3} R$, we have $\zeta = +\frac{2}{3} R$ from which the position of the axial focal line $\zeta_2' = -2.3R$ can be calculated by means of eq.(18). Since the radial focal line has been achromatic, the fantail of dispersed trajectories will only elongate the axial focal line in the same direction as the aperture of the beam so that, once the astigmatism is corrected, the dispersion of the prism will enter only over the intermediary of terms in $\left(\frac{\Delta V}{V}\right)^2$ and $\gamma \left(\frac{\Delta V}{V}\right)$.

It is now a question whether our above findings on the center P of the image I_0 are also valid for any point Q of this image. This question can be answered only within the framework of a general study of second-order aberrations.

c. Second-Order Aberrations Introduced by the Prism .

A study of second-order aberrations will permit a more exact solution than that obtained from eqs.(17) and (18) for the problem of the influence of the prism on any trajectory defined by the five parameters α, β, x_0, y_0, and ΔV. To simplify the calculation, without interfering with the generality of the results, we will avoid a simultaneous variation of all parameters. Depending

on the group of parameters considered, various types of aberration can be differentiated.

a) _Distortion_. Let us assume that the image I_0 is a square, with the center P and with sides parallel to the coordinate axes x and y. Let us imagine that the pencils that contribute to the formation of this image are reduced to a single ray passing through C ($x_0 = y_0 = 0$) and that, in addition, $\Delta V = 0$. The deformation of the pyramidal beam, emerging from C and based on the square RSTU, is described by the terms in α^2, β^2, and $\alpha\beta$. This deformation leads to a distortion of the image given by the prism but by no means limits the resolving power on the image.

The calculations, derived in Appendix I, define the structure of the beam in the planes perpendicular to $O'C'$ at the points O' and C' :

$$x(O') = 2R\alpha - R\alpha^2 - \ldots \beta^2$$
$$y(O') = 2R\beta - 2\pi R\alpha\beta \tag{19}$$

$$x(C') = -4R\alpha^2 - 8R\beta^2$$
$$y(C') = -16R\alpha\beta. \tag{20}$$

From this, we derive the slopes p and q of the trajectories projected, respectively, onto the first and the second principal section:

$$p = -\alpha - \frac{3}{2}(\alpha^2 + 2\beta^2) \quad and \quad q = -\beta - (8 - \pi)\alpha\beta. \tag{11}$$

Consequently, the coordinates of the intersection of any ray with the abscissa plane Z on the axis $O'C'$ are given by the expressions

$$x = pZ + x(C')$$
$$y = qZ + y(C') \tag{12}$$

where Z is the abscissa measured from C' .

The geometry of the beam may be demonstrated by successive cuts made at different points of the axis $O'C'$.

In C', the interaction of the beam yields the form of the crossover sketched in Fig.11a. Th beam is limited by two secant parabolic arcs, symmetric with respect to the x axis and having their concavity turned toward the center of rotation of the trajectories of the magnet (i.e., toward negative x).

If the incident pyramidal beam were not deformed, we would have, in O', a square R'S'T'U' ; in fact, we obtain the contour R"S"T"U" symmetric with respect to ʝx and composed of four parabolic arcs which intersect in R", S", T", and U". The arcs $\widehat{R"U"}$and $\widehat{S"U"}$ have their concavity turned toward negative x while the arcs $\widehat{R"S"}$and $\widehat{T"U"}$ have their concavity turned toward the point O' (Fig.11b).

ln P' , the quantity $Z = -\dfrac{8R}{3}$ causes

$$x(\mathrm{P'}) = \frac{8R}{3}\,\alpha \quad \textit{and} \quad y(\mathrm{P'}) = \frac{8R}{3}\,\beta - \frac{8R}{3}\,(\pi - 2)\alpha\beta.$$

The terms in α^2 and β^2 vanish, resulting in the trapezoidal aspect sketched in Fig.11c. Defining the rate of distortion by $\tau = \dfrac{2R"R'}{R'U'}$, we have

$$\tau = (\pi - 2)\alpha,$$

which, for $\alpha \simeq 10^{-2}$, yields a distortion rate of the order of 1%.

At the abscissa point $Z = -\dfrac{16R}{8-\pi}$, the terms $\alpha\beta$ vanish so that

$$x = \frac{16R}{8-\pi}\,\alpha + \frac{4\pi-8}{8-\pi}\,R\alpha^2 + \frac{8\pi-16}{8-\pi}\,R\beta^2$$
$$y = \frac{16R}{8-\pi}\,\beta.$$

This will yield the pattern sketched in Fig.11d; obviously, changes in the direction of the concavity of the parabolic arcs $\widehat{R"U"}$and $\widehat{S"T"}$ take place.

Finally, at the point P", we will have Z = -4.3 R from which it follows that

$$x(\mathrm{P"}) = 4.3R\alpha + 2.45(\alpha^2 + 2\beta^2)R$$
$$y(\mathrm{P"}) = 4.3R\alpha + 4.9R\alpha\beta.$$

The contour R"S"T"U" in Fig.11e is formed by four parabolic arcs which

intersect in R", S", T", U" and are symmetric with respect to the x axis. The concavity of the arcs $\widehat{R"U"}$ and $\widehat{S"T"}$ is turned toward positive x.

Let us also note the development of the slope of the tangents to the arc $\widehat{R"S"}$, for example, the slope which, from negative in the plane O', changes to positive in the plane P" and cancels in the abscissa plane $Z = -\dfrac{16R}{8-\pi}$.

This demonstrates that the shape of the distortion depends on the plane from which it is viewed, which means it is difficult to decide which definitely is the distortion that might affect the observed image. To answer this question, we must return to the fact that the prism is an astigmatic system for any other pair of points than C and C'.

Let us thus imagine that we have inserted at C', an astigmatism corrector which only acts on the trajectories projected onto the first principal section; this compensator reduces the radial focal line I_0' to the axial focal line $I_0"$. If the crossover C' had no aberration at all, the successive aspects described below would be integrally preserved since the trajectories passing through the center of this corrector would not be deflected. Because of the aberrations, the trajectories pass at definite points through $x(C') = -4R\alpha^2 - 8R\beta^2$. The action of the corrector (which is a convergent system) transforms a trajectory [x, p] into a trajectory [x, p - u] where u = kx, with k being a constant characterizing the convergence of the correcting lens. To determine k, let us note that

$$\frac{x}{8R} \quad u = \frac{x}{4.3R}$$
$$3$$

since the radial focal line is reduced to the axial focal line, i.e.,

$$\frac{3}{8R} - k = \frac{1}{4.3R},$$

Since

$$4.3 = \frac{8}{5 - \pi} \qquad \text{we have} \quad 4R = \frac{\pi}{8}^{-2}.$$

The trajectory [x, p] will thus be transformed into a trajectory

$$\left[x(C') - \alpha + \left(\frac{\pi}{8}^{-2} - \frac{3}{2} \right) (\alpha^2 + 2\beta^2) \right],$$

which will yield, in the plane P'',

$$x(P'') = -\left[-\alpha + \left(\frac{\pi}{8}^{-2} - \frac{3}{2} \right) (\alpha^2 + 2\beta^2) \right] \frac{8}{5 - \pi} \\ - 4R(\sigma^2 + 2\beta^2).$$

After reduction, the terms in α^2 and β^2 vanish and we will finally have, in the plane P_0'',

$$x(P'') = \frac{8}{5 - \pi} R$$
$$y(P'') = \frac{S}{5 - \pi} R\beta + 4.9 R\alpha\beta$$

from which results the trapezoidal distortion sketched in Fig.11f; the rate of distortion, being $\frac{4.9}{4.3} \alpha$, is about 1%.

b) <u>Field astigmatism. Edge effect</u>. The distortion influences the spacing of the image points. The defects described below refer to the image points themselves; each of these points is surrounded by an aberration spot which limits the resolving power. To study these defects, it is therefore possible to disregard the distortion, keeping in mind, of course, that the found defects affect each point of the distorted image.

Equations (15) and (16), which yield the conjugation relations between <u>/17</u> the object and image points, have been derived to about the second order, which means that the first-order "aberrations" on the image are zero or else, since the aperture of the beam is an infinitely small first-order quantity, that the position of the images is known only to the first order. Thus, eqs.(15) and (16) will determine the position of the image of a point such as P located on

the axis CO, while the position of the image of the off-axis point Q is defined only to approximately the first order. This justifies the question as to whether the prism is "aplanatic".
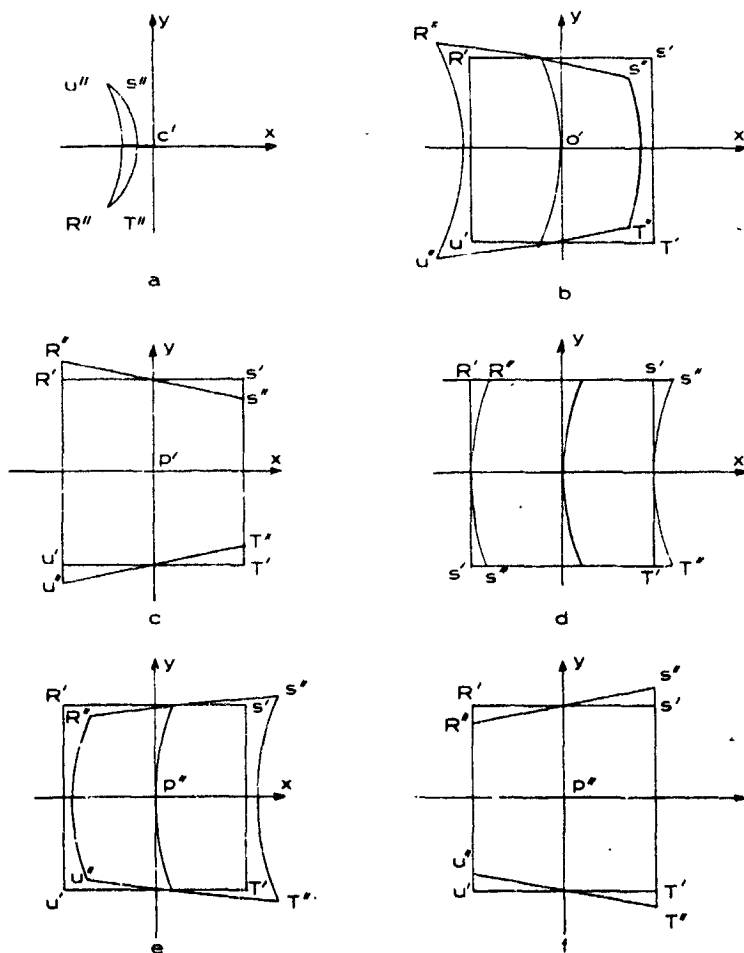

Fig.11

In the calculations given in the Appendix, we have terms in $x_0\alpha$, $y_0\alpha$, $x_0\beta$, and $y_0\beta$ which contain the elements for answering this question.

Taking only aberrations of this type into consideration, we established (Appendix I) that the coordinates of the intersection of any trajectory with

the plane perpendicular to $O'C'$ in C' are given by

$$x(C') = (\pi - 2)y_0\beta - x_0$$
$$y(C') = (\pi - 2)y_0\alpha - y_0$$

and, in O' ,

$$x(O') = 2R\alpha - \frac{x_0}{4} - \frac{x_0\alpha}{4} - \frac{y_0\beta}{2}$$

$$y(O') = 2R\beta - \frac{\pi - 1}{4}y_0 + \frac{\pi}{4}x_0\beta - \left(\frac{\pi}{4} + 2\right)y_0\alpha .$$

From this, we can derive the slopes of the trajectories at the exit from
the prism:

$$p = \frac{x(C') - x(O')}{2R} = -\alpha - \frac{3x_0}{8R} + \left(\pi - \frac{3}{2}\right)\frac{y_0\beta}{2R} + \frac{x_0\alpha}{8R}$$

$$q = \frac{y(C') - y(O')}{2R} = -\beta - \frac{5 - \pi}{8}\frac{y_0}{R} + \frac{5\pi}{8}\frac{y_0\alpha}{R} - \frac{\pi}{8}\frac{x_0\beta}{R} .$$

Let us limit the discussion to trajectories contained in the radial plane.
The aperture of a flat pencil of rays, which initially was to converge in Q, is
limited by the dimensions of the crossover; the axis of this bundle of rays /18
passes through C and makes an angle α with CO. After rotation within the mag-
net, this pencil appears to originate from a virtual point Q'. The rectilinear
trajectories, at the exit from the prism, and their virtual prolongation are
expressed by the following equation:

$$x = \left(-\alpha - \frac{3x_0}{8R} + \frac{x_0\alpha}{8R}\right)Z - x_0$$

Since $\beta = 0$, the value of Z which renders this equation independent of x_0, i.e.,
of the aperture of the object pencil, gives the abscissa of the point Q' where
the image pencil is focused. This yields

$$x = \frac{8R\alpha}{3} + \frac{3}{9}R\alpha^2, \quad \text{to about the third order, for}$$

$$Z = -\frac{8R}{3}\left(1 + \frac{\alpha}{3}\right).$$

At $\alpha = 0$, the point Q' coincides with P' located on the axis $O'C'$ such

that $Z = -\dfrac{8R}{3}$.

If α is not zero, the point Q' no longer will be on a segment of a straight line perpendicular to $O'C'$ in P' but beyond or before the segment, depending on the sign of α (Fig.12). The image of a virtual segment PQ is a virtual segment $P'Q'$ inclined to the axis $O'C'$ by an angle whose tangent is equal to 3 in absolute value whereas it would be infinite if $P'Q'$ were perpendicular to the axis $O'C'$. This is simply due to the fact that the trajectories [α], for the case that α is positive, follow, within the magnet, a path longer than that of the trajectories [$\alpha = 0$] and thus are subject to a stronger convergent effect. The pencil originating from the virtual point Q' thus is less divergent than the pencil that appears to originate from P', from which it follows that the point Q' is farther back than P'. Analogous reasoning applies to a negative angle α, in that the prism this time exerts a less strong convergent action and that the point Q' thus would be more in front than P'. The same results are obtained from eq.(15) which gives the position of the conjugate points in the first principal section; the angle of deviation Φ is successively taken as equal to $\dfrac{\pi}{2} + 2\alpha$, $\dfrac{\pi}{2}$ and $\dfrac{\pi}{2} - 2\alpha$. In conclusion, it can be stated that, in the first principal section, the prism is a "nonaplanatic" system.

Since the prism has a differing convergent effect, depending on the angle α, it is suggested to investigate the behavior of a flat pencil contained in each of several cylindrical surfaces analogous to the second principal section but differing from it by the "curve (χ)" contained in the radial plane which for... as axis for their generatrices. Each "curve (χ)" comprises a circular arc of radius R and an angle at the center $\dfrac{\pi}{2} + 2\alpha$ to which refer, respectively, at the entrance and at the exit of the magnet the projections onto the radial plane of the axis (α, β) of the pencil and of the axis ($-\alpha$, $-\beta$). Thus,

each surface is characterized by the angle α. The aperture of a flat pencil which initially converged toward a point Q of I_0 has a value of $\dfrac{3y_0}{8R}$ (since the pencil is flat, x_0 is zero). At the exit from the prism, the rectilinear trajectories and their virtual prolongation are expressed by the equation

$$y = \left(-9 \cdot 5 \frac{\pi}{8} \frac{y_0}{R} + \frac{5\pi}{8} \frac{y_0 \alpha}{R} \right) Z - \pi - 2 y_0 \alpha - y_0.$$

The value of Z which renders y independent of y_0, i.e., of the aperture of an object pencil, gives the position of the point Q'' where the image pencil focuses. We then have

$$y = \frac{8R}{5 - \pi} \left[1 + \left(2 + \frac{\pi^2}{5 - \pi} \right) \alpha \right] \beta, \quad \text{to within the third order,}$$

for

$$Z = -\frac{8R}{5 - \pi} \left[1 + \left(2 - \frac{\pi^2}{5 - \pi} \right) \right].$$

If α and β are zero, the position of the point P'' is obtained. Since Z is independent of β, the image of a small virtual segment of a straight line perpendicular to the radial plane, is also a small virtual segment of a straight line perpendicular to the radial plane, no matter what the value of α might be. Consequently, we can state that the prism is "aplanatic" in each of the defined surfaces. However, when considering a small plane area, perpendicular to CO in P whose every point is "illuminated" by a flat pencil (for which the convergence in the first principal section exerts no influence), then the virtual image given by the prism will be a plane area, perpendicular to the radial plane and inclined to the axis $O'C'$. The normal to this area, together with the axis $O'C'$, makes an angle whose tangent is $2 + \dfrac{\pi^2}{5 - \pi}$, which yields an angle of about $82°$! This is due to the fact that the axial focusing is highly sensitive to the angle of incidence and to the angle of exit of the beam. A beam entering and leaving the prism at an angle $(\epsilon + \alpha)$ is subject to a much stronger

convergent action than that affecting a beam whose angle is ϵ and which, conse-
quently, moves the axial focal line far in back of the position P".

If, for comparing the resultant effects, we place ourselves in the same
observation plane, it can be imagined that the correction for astigmatism is
done by a correcting lens whose center coincides with C' and which, acting only
on the trajectories projected onto the radial plane, reflects the image P' to
P". The focal lines corresponding, for example, to a point Q have no reason to
coincide so that the astigmatism will be corrected only at the center of the
image. Outside of this center, the beam will remain astigmatic. To give a
general idea on the pattern obtained in that case, let us consider an object
segment perpendicular to OC in P and contained in the radial plane. An ion $\underline{/19}$
pencil converges toward each point of this segment, and the aperture of the
pencil is limited by the diameter d of the crossover. The prism gives an asti -
matic image of each point of the segment. The locus of the points Q' where the
radial focal lines intersect the radial plane is a segment of a straight line D_1
(Fig.12), inclined to the axis $O'C'$ by an angle of about 71° (angle whose tan-
gent is equal to 3). The locus of the points Q", which is the locus of the
axial focal lines, is a segment of a straight line D_2 which, together with $O'C'$,
makes an angle of the order of 8° (complement of the 82° angle). The astig-
matism corrector, of the segment D_1, gives an image D_1' inclined to the axis and
passing through P". However, D_1' is much less slanted than D_2 and, consequently,
when viewing a plane perpendicular to $O'C'$ in P", one would always be closer to
the radial focal line than to the axial focal line. The image points other
than P" are surrounded by an aberration figure elongated in the direction of the
radial focal line, i.e., parallel to the magnetic field, whose elongation is
greater the more the observer is distant from P" (Fig.13). When considering

47

the points outside the radial plane, the aspect to be defined is modified by another type of defect described by the terms in $y_0\beta$ and $x_0\beta$, which had not been
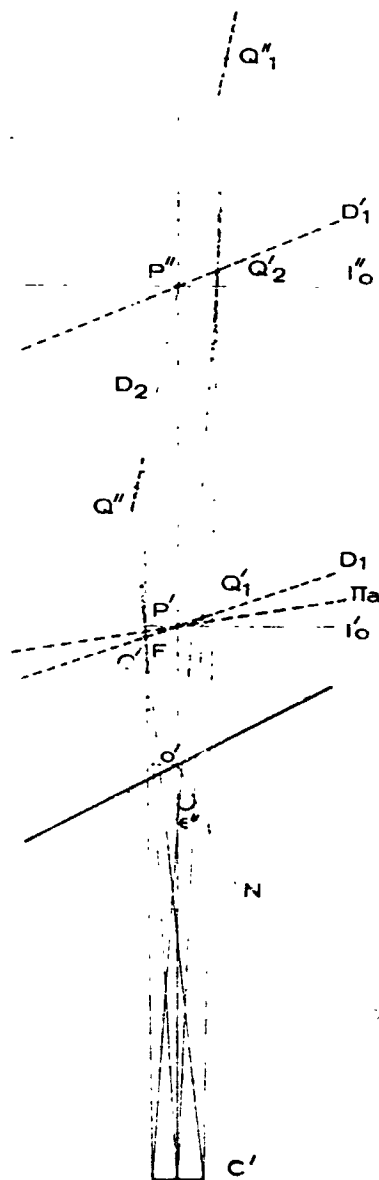

Fig.12

taken into consideration until now, either by assuming $\beta = 0$ or by making use of flat pencils.

These terms represent the specific action of the so-called passage layers. In fact, we demonstrated above that a ray such as $x_0 = 0$, $y_0 = 0$, $\alpha = 0$, $\beta \neq 0$ does not remain in the second principal section and will yield an aberration term equal to $-8R\beta^2$ at the level of C'. In the same manner, if we consider the total beam emerging from the crossover, terms in $x_0\beta$ and $y_0\beta$ will be introduced. On traversing the entrance layers and the exit layers, the beam is given an impulse which lowers the trajectories toward the radial plane; however, this momentum also has the effect to make the beam leave the second principal section. This is known as an edge effect aberration.

Finally, we will have, in the plane $Z = -\dfrac{8R}{3}$,

$$\begin{cases} x = \dfrac{8R}{3}\alpha - \dfrac{\pi}{3}y_0\beta - \dfrac{x_0\alpha}{3} \\ y = \dfrac{8R}{3}\beta + \dfrac{\pi-2}{3}y_0 - 2\left(\dfrac{\pi}{3}+1\right)y_0\alpha + \dfrac{\pi}{3}x_0\beta \end{cases}$$

and, in the plane $Z = -\dfrac{8R}{5-\pi}$,

$$\begin{cases} x = \dfrac{8R}{5-\pi} + \dfrac{\pi-2}{5-\pi}x_0 - \dfrac{\pi^2-3\pi+4}{5-\pi}y_0\beta - \dfrac{x_0\alpha}{5-\pi} \\ y = \dfrac{8R}{5-\pi}\beta - \left(2 + \dfrac{\pi^2}{5-\pi}\right)y_0\alpha + \dfrac{\pi}{5-\pi}x_0\beta. \end{cases}$$

On reducing everything to the plane $Z = -\dfrac{8R}{5-\pi}$, the correcting lens will transform a trajectory $[p, x(C')]$ into $[p - kx, x(C')]$, which will furnish the following trajectory:

$$x = \left[-\alpha - \dfrac{5-\pi}{8}\dfrac{x_0}{R} + \dfrac{8\pi-\pi^2-10}{8}\dfrac{y_0}{R}\beta + \dfrac{x_0\alpha}{8R}\right]Z + (\pi-2)y_0\beta - x_0 \ .$$

i.e.,

$$x = \dfrac{8R}{5-\pi}\alpha - \dfrac{\pi}{5-\pi}y_0\beta - \dfrac{\alpha x_0}{5-\pi}$$

and

$$y = \dfrac{8R}{5-\pi}\beta - \left(2 + \dfrac{\pi^2}{5-\pi}\right)y_0\alpha + \dfrac{\pi}{5-\pi}x_0\beta.$$

49

It is then possible to define the shape of the aberration figure which
surrounds each point Q" of the image, defined by the coordinates

$$x = \frac{8R}{5 - \pi} \alpha \quad \text{and} \quad y = \frac{8R}{5 - \pi} \beta.$$

Since the diaphragm, limiting the crossover, is circular and has a dia-
meter d, we will have

$$x_0 = \frac{d}{2} \cos \psi, \quad y_0 = \frac{d}{2} \sin \psi.$$

where ψ is a parameter which varies from 0 to 2π.

Let us relate the coordinates of any ray to a system (Q"X, Q"Y) whose axes
pass through Q" and are parallel to the axes (P"x, P"y). We then have

$$X = -\frac{\pi\beta}{5 - \pi} y_0 - \frac{\alpha}{5 - \pi} x_0$$
$$= -\frac{d}{2(5 - \pi)} (\pi\beta \sin \psi + \alpha \cos \psi$$
$$Y = -\left(2 + \frac{\pi^2}{5 - \pi}\right) \alpha y_0 + \frac{\pi\beta}{5 - \pi} x_0$$
$$= -\frac{d}{2(5 - \pi)} (\pi^2 - 2\pi + 10)\alpha \sin \psi - \pi\beta \cos \psi.$$

The aberration figure, surrounding Q", is limited by an ellipse whose
major axis, together with the Y axis, makes an angle ω such that tan 2ω =
$= \frac{2\pi}{\pi^2 - 2\pi + 11} \cdot \frac{\beta}{\alpha}$; the distance of one point of the ellipse to its center Q" is

$$\rho^2 = X^2 + Y^2$$
$$= \frac{d^2}{4(5 - \pi)^2} [\pi^2\beta^2 - 2\pi(\pi^2 - 2\pi + 9)\alpha\beta \sin \psi \cos \psi$$
$$+ \alpha^2 \cos^2 \psi + \alpha^2(\pi^2 - 2\pi + 10) \sin^2 \psi].$$

For α = 0, the ellipse becomes a circle with a radius of $\frac{\pi\beta}{2(5 - \pi)}$ d; the
aberration terms are due exclusively to the edge effect. At β = 0, the major
axis of the ellipse is vertical and has a value of $\left(2 + \frac{\pi^2}{5 - \pi}\right) d\alpha$, while the value
of the minor axis is $\frac{d\alpha}{5 - \pi}$; this aberration is produced by the single effect
of field astigmatism. On traversing a square of the type R' S' T' U' , the general

shape will be that shown in Fig.13.

It should be mentioned that the above-described aberrations affect an enlarged image of the object; to define the resolving power which these aberrations are likely to limit, it is necessary to refer them to the object by taking
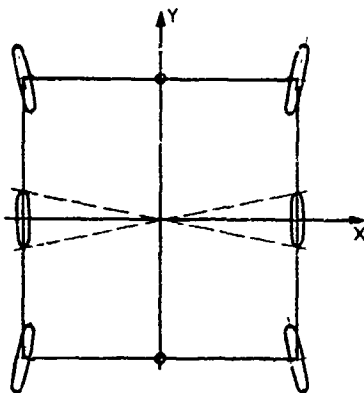
Fig.13

the enlargement of the image into consideration. On maintaining α, β, and d constant, the aberrations due to the prism remain invariant on increasing the enlargement of the image I_0 and consequently the aberrations referred to the object will be weaker. Thus, in principle, their effects can be reduced as much as desired.

Let us assume that, in a certain arrangement, we obtain a limit of resolution δ on the filtered image. This limit is composed of two terms δ_a and δ_L one of which is due to the magnet and the other to the emission lens. Let us check on the best way of reducing δ_a by discarding the trivial solution which consists in limiting the observed field to more and more central regions.

The contrast diaphragm of the emission lens can be reduced by a factor k; here, δ_a and δ_L, respectively, are changed into $\frac{\delta_a}{k}$ and $\frac{\delta_L}{k^2}$; in addition, the

51

intensity of the light allowed to strike the image is divided by k^2. This method is not advantageous since it improves the resolving power of the objective much more rapidly than that of the magnet which here is assumed to be the principal cause of limitation.

However, it is also possible to enlarge the image I_0 by a factor k, for example, on reducing the geometric parameters of the emission lens by a factor k. For a diaphragm with a diameter d/k, no decrease in the flux of secondary ions striking the image will result from this. Nevertheless, since the electric field E_0 is now k-times higher, the limit of resolution of the lens is k-times weaker and is δ_L/k. The reduction of the diaphragm and the increase in enlargement of I_0, at unchanged α and β, result in a decrease in δ_a which becomes δ_a/k^2, while the imaged field is reduced by a factor k. Consequently, it is obvious that the limit of resolution, introduced by the magnet, can be reduced as much as desired. If the "image quality" is defined as the ratio of the dimension of the observed field to the value of the limit of resolution δ and if we proceed as described below, the quality of the filtered image will increase and tend toward a value which it would have at zero δ_a.

Finally, let us give an order of magnitude. In the device designed by us, we have $\alpha \simeq 10^{-2}$, $d = 0.4$ mm, and, at the level of I_0'', an enlargement of the image of the order of 40. With reference to the object, the limit of resolution introduced by the magnet along the edges of a field of 0.3 mm diameter, is /21 about 0.8 μ while δ_L is of the order of 0.7 μ.

c) <u>Aperture aberrations</u>. This type of defect are aberrations in x_0^2, y_0^2, and $x_0 y_0$. They are noticeable only at the center of the observed field, since it is obvious that they can be neglected with respect to the field aberrations described above.

In addition, when referred to the object, these aberrations are negligible with respect to the resolution limit given by the immersion objective. It should be mentioned that, on reducing the diameter d of the contrast diaphragm by a factor k, the limit of resolution of the emission lens is divided by k^3 and, since x_0 and y_0 become $\frac{x_0}{k}$ and $\frac{y_0}{k}$, the aberrations due to the prism will also be divided by k^2. These aberrations will thus never be able to reduce the resolving power obtained on the filtered image.
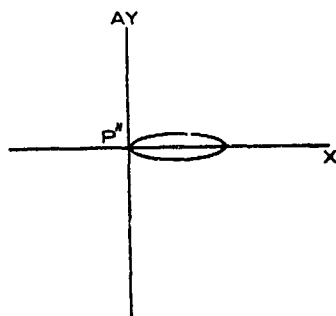
Fig.14

Let us recall the form of the aberration disk in the plane I_0'', after correction of the astigmatism:

$$x(P'') = \frac{27 + 10\pi}{16R} \cdot \frac{\pi^2}{} y_0^2 \quad \textbf{and} \quad y(P'') = \frac{4 - \pi}{5 - \pi} \frac{\pi}{8} \frac{x_0 y_0}{R}.$$

It is clear that this disk has the form of an ellipse whose major axis coincides with P_x'' and has a value of about $\frac{3d^2}{4R}$ (Fig.14).

In the setup developed by us, this will lead to a limit of resolution on the object of the order of $0.04\,\mu$, whereas the objective gives a limit of the order of microns.

d) <u>Chromatic aberrations</u>. In the description of geometric aberrations, we have implicitly assumed that ΔV is zero. However, ΔV differs from zero. Conse-

53

quently, chromatic aberration terms of the type

$$\frac{\Delta V}{V}\alpha, \quad \frac{\Delta V}{V}\beta, \quad \frac{\Delta V}{V}x_0 \quad and \quad \frac{\Delta V}{V}y_0 \quad and \quad \left(\frac{\Delta V}{V}\right)^2.$$

are introduced. We will neglect $\left(\frac{\Delta V}{V}\right)^2$ with respect to the other terms.

Taking only chromatic aberrations into consideration, the intersection of any ray will be given, at the level of C' resp. O' by

$$\begin{cases} x(C') = -x_0 + 2\frac{\Delta V}{V}R + \frac{1}{8}\frac{\Delta V}{V}x_0 + 3\frac{\Delta V}{V}R\alpha \\ y(C') = -y_0 \end{cases}$$

and

$$\begin{cases} x(O') = -\frac{x_0}{4} + 2R\alpha + \frac{1}{2}\frac{\Delta V}{V}\cdot R + \frac{1}{8}\frac{\Delta V}{V}x_0 + \frac{\Delta V}{V}\cdot R\alpha \\ y(O') = -\frac{\pi-1}{4}y_0 + 2R\beta + \frac{\pi}{8}\cdot\frac{\Delta V}{V}y_0. \end{cases}$$

From this, we derive

$$p = \frac{x(C') - x(O')}{2R} = -\frac{3}{8}\frac{x_0}{R} - \alpha + \frac{3}{4}\cdot\frac{\Delta V}{V} + \frac{\Delta V}{V}\alpha$$

$$q = \frac{y(C') - y(O')}{2R} = -\frac{5-\pi}{8}\frac{y_0}{R} - \beta - \frac{16}{\pi}\frac{\Delta V}{V}\frac{y_0}{R}.$$

In the radial plane a ray with the equation $x = pZ + x(C')$ intersects the plane of the abscissa

$$Z = -\frac{8R}{3}\text{ in }x(P') = \frac{8R}{3}\cdot\alpha + \frac{1}{3}\cdot\frac{\Delta V}{V}\cdot R\alpha + \frac{1}{8}\cdot\frac{\Delta V}{V}x_0.$$

At $\alpha = 0$ and $x_0 = 0$, the position of the chromatic focal line will be found readily. The term $\frac{1}{3}\frac{\Delta V}{V}R\alpha$ vanishes in the plane $Z = -\frac{8}{3}R\left(1 + \frac{\alpha}{6}\right)$, which indicates that the "achromatic plane" is inclined to the axis $O'C'$. The term $\frac{1}{8}\cdot\frac{\Delta V}{V}x_0$ can also be eliminated in the plane $Z = -\frac{8R}{3}\left(1 + \frac{1}{16}\frac{x_0}{R}\right)$ or, on introducing the angle $\gamma = \frac{3x_0}{8R}$ which is the half-aperture of the pencil that converges in any point of the image I_0, in the plane $Z = -\frac{8R}{3}\left(1 + \frac{\gamma}{6}\right)$. Thus, the plane π_a passing through F (Fig.12) perpendicular to the radial plane and having a normal which makes an angle ω with the axis $O'C'$ such that $\tan\omega = \frac{1}{6}$,

is an achromatic plane.

Now, let us consider the total beam and let us be stationed in the plane I_0'' where the astigmatism is canceled by the action of a correcting lens placed at the level of C'. A simple calculation, analogous to those made above, indicates that, in the plane $Z = -\dfrac{8}{5-\pi} R$, the coordinates of the intersection of any trajectory will be

$$x(P'') = \frac{8R}{5-\pi}\alpha + \frac{1}{5-\pi}\cdot\frac{\Delta V}{V}R\alpha + \frac{3}{8(5-\pi)}\frac{\Delta V}{V}x_0$$
$$y(P'') = \frac{8R}{5-\pi}\beta + \frac{\pi}{2(5-\pi)}\frac{\Delta V}{V}y_0.$$

At $\alpha = 0$, the aberration figure is limited by an ellipse with a vertical major axis, whose minor and major axes, respectively, have the value of

$$\frac{3}{8(5-\pi)}d\cdot\frac{\Delta V}{V} \text{ and } \frac{\pi}{2(5-\pi)}d\cdot\frac{\Delta V}{V}:$$

At $\alpha \neq 0$, the aberration figure has the shape of an aigrette terminated by an elliptical arc (Fig.15).
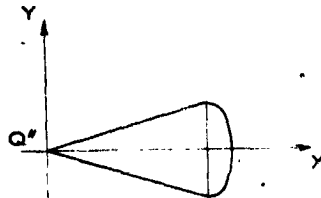

Fig.15

e) <u>Energy filtering</u>. The value of $\dfrac{\Delta V}{V}$ depends on the width h of the selection slit, on the diameter d of the crossover object C, and on the geometric aberrations that influence the crossover image C'. Since the slit is parallel to the y axis, only the geometric aberrations exert an influence, en-

larging the crossover in the direction of x. It is easy to verify that the

aberrations in α^2 and β^2 are predominant at the level of C' . Thus, we have

$$x(C') \simeq -x_0 + 2R\frac{\Delta V}{V} - 4R\alpha^2 - 8R\beta^2.$$

Let us denote by d_a the maximum value assumed by the geometric aberrations on

the x axis and let us assume that the ray corresponding to a zero initial energy

passes through C' . The ions with an initial energy $e\varphi_0$, disregarding the aber-

rations, form a crossover image whose center moves away toward positive x pro-

portional to φ_0 but whose diameter increases as $\sqrt{\varphi_0}$ as soon as φ_0 is less than

φ_{0x} . The abscissa x_t of the extremity of the crossover image, still assuming

the absence of aberration, located on the side of negative x is given by the

relation

$$x_t = 2R\frac{\varphi_0}{V} - 4\Delta\sqrt{\frac{\varphi_0}{V}}.$$

Since φ_0 varies, x_t presents a minimum equal to $-2\frac{\Delta^2}{R}$ for $\frac{\varphi_0}{V} = \frac{\varphi_{01}}{V} = \frac{\Delta^2}{R^2}$

at $\varphi_{01} \geq \varphi_{0x}$ or equal to $2R\frac{\varphi_{0m}}{V} - \frac{d}{2}$ for $\varphi_0 = \varphi_{0m}$ if $\varphi_{01} \leq \varphi_{0m}$. Let x_A be the abscissa

of the extremity of the crossover image on the side of negative x, taking the

aberrations into consideration, so that we have

$$x_A = -d_a + x_R.$$

If one does not wish to "lose" the particles on the side of low energies, it is

necessary to place one of the rims of the slit into x_A so that the abscissa x_B

of the other rim will be

$$x_B = x_A + h.$$

There exists an initial energy $e\varphi_{0m}$ for which the corresponding crossover

is outside of the slit but in such a manner that one extremity still touches

the rim located in x_B; φ_{0m} gives the value ΔV of the pass band. Let 2ρ be the

diameter of this crossover, a diameter equal to d if $\varphi_{oK} \geq \varphi_{on}$ and equal to $8\Delta\sqrt{\dfrac{\varphi_{oH}}{V}}$ if $\varphi_{oK} < \varphi_{on}$. The center of this crossover is located on the abscissa $x_a + d_a + \rho$ so that the following relation is obtained:

$$2R\frac{\Delta V}{V} = x_a + d_a + \rho.$$

Let us assume, as will be always the case in the following text, that h and φ_{on} are such that $\varphi_{oH} > \varphi_{on}$, i.e., that $2\rho = d$. Two cases are then in question:

$$\varphi_{o1} > \varphi_{om}$$

which result in

$$\frac{\Delta V}{V} = \frac{h}{2R} + 2\frac{\sqrt{\varphi_{o1}}\cdot\sqrt{\varphi_{om}}}{V} - \frac{\varphi_{o1}}{V}$$

and

$$\varphi_{o1} \leqslant \varphi_{om} \quad \text{which yields} \quad \frac{\Delta V}{V} = \frac{\varphi_{om}}{V} + \frac{h}{2R}.$$

Naturally, if one is not interested in conserving the particles that leave the target at low initial velocities and if an energy band of a width ΔV is isolated whose center is sufficiently far from the energy $e\varphi_o = 0$, we will have

$$2R\frac{\Delta V}{V} = h + d + d_a \quad \text{i.e.,} \quad \frac{\Delta V}{V} = \frac{h}{2R} + \frac{d + d_a}{2R}.$$

This goes back to the classical expression; the ray corresponding to $e\varphi_o$ of zero no longer passes through C'.

The width given to the slit is ruled by the desire to obtain an image of uniform illumination for the case that the object presents no variations in concentration. If the slit suppresses some rays, shadows will appear on the image (Bibl.25). However, because of the initial energy dispersion and the finite width of the slit, there will necessarily be energies in existence for which the corresponding crossover does not give complete passage, in which case

the particles eliminated in this manner must not be too numerous. Unfortunate-
ly, the calculation of the optimum widths for the slit requires knowledge of
the dispersion law of the initial energies. If this is impossible, it could be
assumed that the slit must at least permit passage of all ions with an energy
$e\varphi_{ea}$; since the ions of higher energy are already partially eliminated by the
contrast diaphragm, their contribution to the formation of the image may be less
important. However, if $e\varphi_{ea}$ is far on this side of the mean emission energy,
the ions having an energy higher than $e\varphi_{ea}$ may, despite the presence of the
diaphragm, represent a considerable fraction of the total number of ions that
form the image. Thus, it would be highly desirable to have a controllable /23
slit which would make it possible to adjust the value of h during operation.

Nevertheless, to give an order of magnitude, let us assume that the width
of the slit is such that $h = d + d_a$ and that a circular diaphragm limits to u
the half-aperture of the beam emerging from C. We then have

$$\alpha = u \cos \psi \quad \text{and} \quad \beta = u \sin \psi,$$

where ψ is a parameter that varies from 0 to 2π on traversing the edge of the
aperture diaphragm. The maximum of the expression $4R\alpha^2 + 8R\beta^2$ is obtained for
$\psi = \dfrac{\pi}{2}$ and, consequently, $d^a = 8Ru^2$. For the values of Δ, V, u, R given above
and at $d = 0.5$ mm, we have

$$\varphi_{em} \simeq 1 \text{ volt} \quad \text{and} \quad \varphi_{ei} < \varphi_{om}.$$

Thus, we find $\dfrac{\Delta V}{V} \simeq 3 \times 10^{-3}$.

It is now possible to evaluate the order of magnitude of the chromatic
aberrations at the level of the image I_0''. At the center of the image I_0'', the
minor and the major axes of the aberration ellipse assume, respectively, the
values $0.3\ \mu$ and $1.3\ \mu$. In addition, the term in $\dfrac{\Delta V}{V}\ \alpha$ introduces an aberra-
tion of the order of $1.8\ \mu$ along the edge of the imaged field. These aberra-

tions affect an image at a magnification of about 40 and thus, with reference
to the object, will be less than 0.05 μ and therefore negligible with respect
to the limit of resolution of 1 μ which is imposed by the immersion lens used
with a diaphragm of 0.4 mm.

In summation, it can be stated that the prism, combined with an astigmatism
compensator, will convert the initial image I_0 into a filtered image at the
level of I_0'. This image will be affected by a weak distortion. In addition,
since the magnetic prism does not focus except at about the second order, the
planes perpendicular to the mean trajectory will no longer be favored as is the
case for a Gaussian optics of revolution. It follows from this that the geo-
metric loci of the radial, axial, and chromatic focal lines are planes inclined
to the optical axis of the system but still remaining perpendicular to the
radial plane; this results in a type of field defect supplemented by other field
aberrations introduced by the passage layers. Of all these defects only the
field astigmatism has a noticeable influence; in addition, its effects can be
made less noticeable than those of the defects of the initial image.

5. Observation of the Filtered Image

For a given excitation of the magnetic prism, only one type of secondary
ions, after rotation within the magnet, will pass through the selection slit
placed in C' and will form the image of the object surface. This image is
virtual and astigmatic.

a. Correction of Astigmatism

The correction must be preferably effected in the vicinity of the crossover
C' so that the central region of the correcting lens can be used to its optimum

extent and that the position of C' is influenced as little as possible.

The stigmatizer is an electrostatic hexapole of classical type but operating under rather unusual conditions for this type of lens. In fact, we found that, at the level of C', the dispersion of the trajectories in the radial plane yielded a term $2\frac{R\Delta V}{V}$ which means that the correcting lens must act, on either side of its center, on particles of differing energy. However, the chromatic defect which might result from this does not interfere. The ions passing from the side of positive x are faster, which means that they are less deflected by the stigmatizer, whereas those ions that pass on the side of negative x are slower and thus more deflected; in all, the trajectories envelop a caustic whose contact point with the axis of the beam is the point of ordinary convergence for a beam of monokinetic particles, except that the convergence will be of about the second order in $\frac{\Delta V}{V}$. Since, in the object space, the trajectories have their footpoint on a caustic because of the existence of a chromatic focal line, the influence of the lens modifies the shape of this caustic without affecting the ordinary positions of convergence or introducing new aberrations.

We definitely can then observe a virtual image located at the level of I_0'', i.e., quite far in back of O'. To sight this image, it will thus be necessary to insert behind the crossover C' a device of the type of a telephoto lens, which would furnish a real ion image of this crossover.

b. "Telephoto" System

The arrangement for observing the ion image necessarily terminates in the image converter described above. The electron image, resulting from conversion of the ion image, is received on a fluorescent screen of which it is known that

the luminous efficiency is greater the higher the energy of the impinging elec-

trons. Therefore, it would be desirable to give the cathode of the converter a

highly negative polarization so as to have the electrons reach the screen with

energies of at least several tens of kiloelectron-volts.

In addition, since the radius of curvature of the trajectories within the

magnet is proportional to the square root of the energy of secondary ions, these

latter will be accelerated in the emission lens only at a potential difference

of several kilovolts, so as to maintain a practical order of magnitude in view

of the values of the magnetic field and the dimensions of the experimental

equipment.

When used under these conditions, the converter will strongly contract

the ion image, thus reducing in the same proportion the final enlargement at

which the image of the object surface is observed. Any further enlargement

of this image encounters two types of limitations, one of which is due to the

discontinuous nature of the receiver (fluorescent screen, photographic plate)

while the other is due to the resolution limit of the converter introduced by

the energy dispersion of the secondary electrons emitted by the cathode. In

order to prevent the converter from limiting the resolving power given by the

preceding optical system, it is possible either to increase the enlargement of

the ion image projected onto the converter cathode or else to reduce the con-

traction to lower values. The first solution is inapplicable since it would

mean that an image with an extremely reduced field will be observed. Thus, the

second solution is the only one possible; in this solution, a postacceleration

of the ions after traversing the magnet, will be necessary.

a) <u>Postacceleration</u>. Acceleration of the ions takes place between the

two plane electrodes E_4 and E_5 which, respectively, are brought to the potential

of the mass and to a negative potential $-V_1$ and are composed of two circular
diaphragms with an axis $O'C'$ spaced at a distance Δ from each other. The space
after the electrode E_5 is limited by a cylindrical tube with an axis $O'C'$ which
is brought to the same potential as the electrode E_6. After having crossed the
plane of this electrode, the ions will thus move in an equipotential space where
they are agitated by an energy $eV_2 = e(V + V_1)$. Since the square root of the
energy of the particles, in corpuscular optics, plays the role of the refractive
index in light optics, the total postacceleration arrangement forms an immersion
system. This system does not limit its function to a simple acceleration of
the ions but also causes the ion trajectories to converge. The optical charac-
teristics of postacceleration can be readily calculated by the Ganz method.
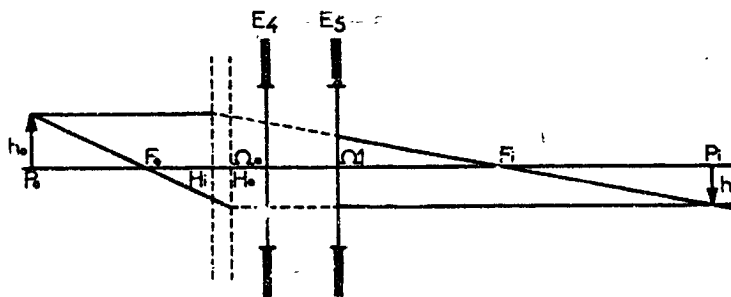
Fig.16

It is generally known that this method consists in replacing the curve of
the electric potential variation on the axis of the optical system by a poly-
gonal line where each side corresponds to an interval over which the potential
is assumed to vary linearly along the axis. Consequently, the derivative of the
potential is discontinuous as soon as we pass from one interval to the other.
The conservation of the electric induction flux thus causes the appearance of a
radial component of the electric field which would be infinite, which is physi-

cally illogical but is mathematically convenient for calculating the trajec-
tories. The action of this radial component consists in a pulsation which pro-
duces a change in direction of the particle velocity at each passage from one
interval to the other. Since, at the interior of each interval, the electric
field is uniform and parallel to the axis, the calculated trajectory in this
approximation is a broken line whose every segment is formed by a parabolic arc.

In the postacceleration system of interest here, it is sufficient to use a
single interval, limited by the planes of two electrodes E_4 and E_6 (assumed to
be infinitely thin). The resultant approximation will be acceptable since the
particles never are displaced at velocities sufficiently low for having the
accurate form of the electric field noticeably modify the slope of the calcu-
lated trajectory.

The influence of postacceleration on the trajectories is completely de-
scribed by the optical characteristics of the system. Let Ω_0 and Ω_1 be the
intersection points of the planes of the electrodes E_4 and E_6 with the optical
axis (see Fig.16); let F_0 and F_1 be the foci of the object and of the image,
while H_0 and H_1 will be the intersections of the principal planes of the object
and the image with the axis. This will yield the following formulas:

$$\overline{H_1\Omega_1} = \frac{4\Delta}{3}\frac{V_2}{V_2 - V}\overline{V}, \; \overline{F_1\Omega_1} = \frac{4\Delta}{3}\frac{\left(3 - \sqrt{\frac{\overline{V_2}}{\overline{V}}}\right)\frac{V_2}{V}}{\left(1 - \sqrt{\frac{V_2}{\overline{V}}}\right)\left(\frac{V_2}{V} - 1\right)}$$

$$\overline{H_0\Omega_0} = \frac{4\Delta}{3}\frac{V}{V_2 - V}\overline{V}, \; \overline{F_0\Omega_0} = \frac{4\Delta}{3}\frac{3\sqrt{\frac{V_2}{V}} - 1}{\left(\sqrt{\frac{V_2}{V}} - 1\right)\left(\frac{V_2}{V} - 1\right)}$$

The conjugation correlation between an object point P_0 and an image point
P_1 will be

$$\overline{F_0H_0}.\overline{F_1H_1} = \overline{F_1P_1}.\overline{F_0P_0}.$$

The linear enlargement $\frac{h_i}{h_0}$ has a value of $\frac{F_0 H_0}{F_0 P_0} = \frac{F_i P_i}{V_i H_i}$. The Lagrange-

Helmholtz relation $\sqrt{V h_0 \alpha} = \sqrt{V_i h_i \alpha_i}$, where α and α_i are the apertures on the

object side and on the image side, completes this formula group which is well

known in optics (Bibl.21).
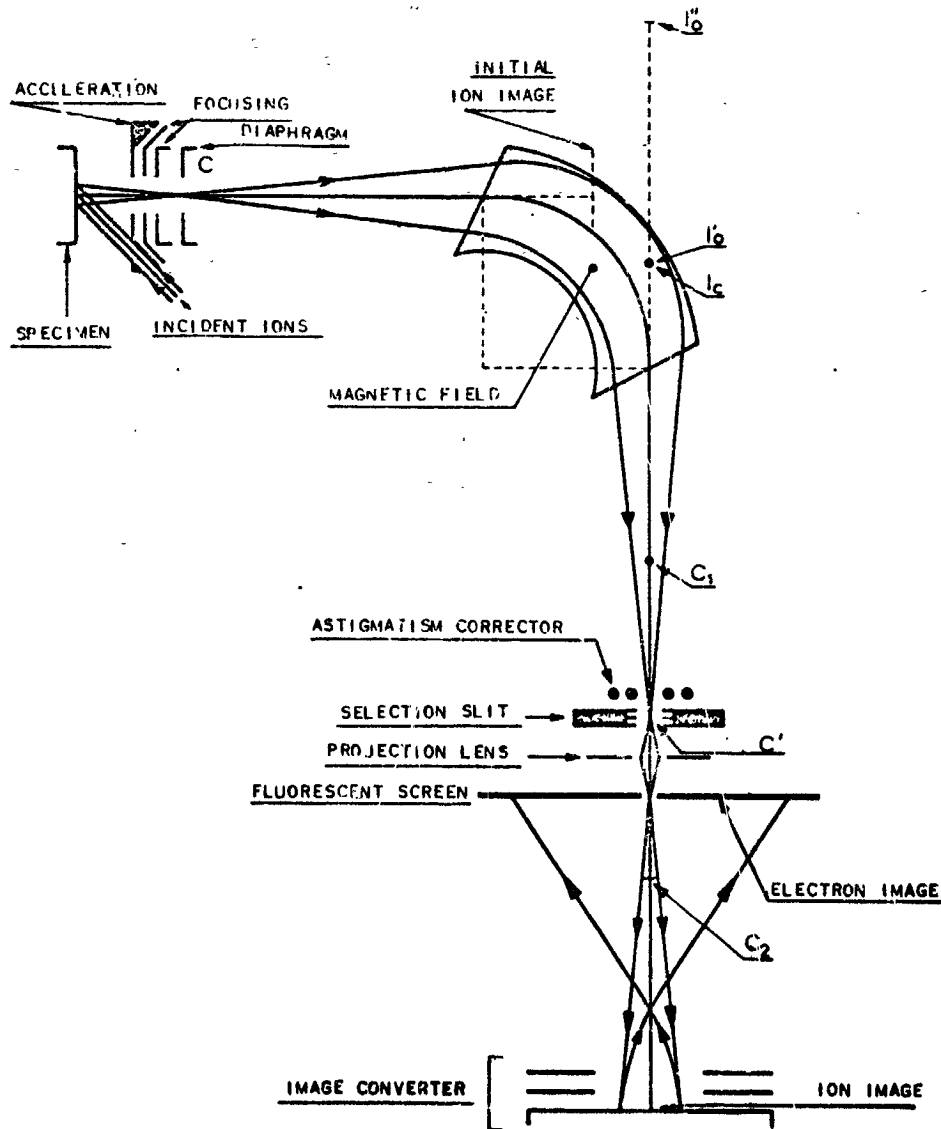
Principal Sketch

The postacceleration device constitutes the first lens of our telephoto lens system and furnishes, of the virtual image I_0'' filtered by the prism, a real image I_1 located near the image focus F_1. Conversely, the image of the crossover C' is virtual and located in C_1.

b) Projection lens. The image I_1 has too slight an enlargement to be directly usable in the converter. It is necessary to add an auxiliary lens to the postacceleration system, which will project the image I_1 onto the converter cathode. In addition, this lens gives a real image C_1' of the crossover C_1. If the fluorescent screen for receiving the electron image is placed at the level of C_1', the dimensions of the hole in the screen, allowing passage of the ion beam, can be the same as those of the crossover C_1'; thus, the useful surface of the screen would not be reduced by the presence of this hole.

The projection lens simply is a unipotential electrostatic lens whose characteristics can be derived from graphs (Bibl.21) or can be calculated, for example, from Regenstreif's formulas (Bibl.28). /26

The combination of the projection lens with the postacceleration lens constitutes the telephoto lens which furnishes, of the virtual image I_0'', an ion image focused on the cathode of the converter.

c. Image Converter

The image converter is of the type described above. This converter constitutes the final element of the entire unit for permitting observation of the ion image filtered by the magnet. This converter transforms the ion image into an electron image which can be observed on the fluorescent screen over the intermediary of a plane mirror, inclined by $45°$ to the axis (Fig.23).

The various devices described above are arranged within the optical unit

in accordance with the above principal sketch. The design of the experimental apparatus follows more or less the general lines sketched here.

CHAPTER II

EXPERIMENTAL SETUP

The first problem before even starting the design of the apparatus is the vacuum that must be maintained in the enclosures in which the particles are moving. At first sight, this problem seems identical to that ordinarily encountered in mass spectrography. However, there are some differences which should be mentioned here.

1. Vacuum

In mass spectrography, ion sources are generally used in which the residual gas of the vacuum enclosure can be ionized, which results in parasite spikes whose intensity may be comparable to that of the lines of the elements to be analyzed. So as to reduce the intensity of these peaks, it is necessary to produce extremely high and clean vacuums, i.e., vacuums free of hydrocarbon vapors such as might be due to diffusion-pump lubricants or to degassing of organic matter. In our case, the secondary particles leave the target directly in the form of ions, meaning that their ionization does not require passage through the vapor phase so that the influence of the residual gas "in the source" will be quite low. The residual gas molecules may be ionized by collision either with primary ions or with secondary ions or electrons; they can also be ionized by the phenomenon of charge exchange with the secondary ions. Each of these processes depends on the frequency of interparticle collisions; however, in the accelerating space of the immersion lens, where such collisions

66

might occur, the distance between the target and the electrode A is only a few millimeters. Therefore, it is necessary that the mean free path of the particles be large with respect to this distance, which does not necessitate extremely high vacuums. In addition, it should be mentioned that the ions formed by the residual gas would be accelerated under potentials staggered all along the potential drop between the target and the electrode A, which means that such ions would be defocused by the immersion lens and practically eliminated by the contrast diaphragm.

However, this reasoning obviously does not take into consideration the fact that the residual gas may react with the material of the target to form surface films of oxides or of adsorbed gas. During the sputtering process, these layers are obliterated as they are formed, giving rise to secondary ions which depend on the compound formed. Therefore, it is necessary to reduce their significance by working in as perfect a vacuum as possible.

In addition, as soon as the ion path lengthens, the diffusion of the ions on the residual gas will manifest itself by the presence of a continuous background and by a broadening of the ion trajectory pencils. This will result in a lessening of contrast and in the appearance of a haze or blur on the image. In addition, if the pressure within the vacuum enclosure rises excessively (5×10^{-4} mu Hg), the charge-exchange process between molecules of the residual gas and secondary ions becomes quite specific and causes the appearance of parasite or ghost images, as observed by Jouffrey (Bibl.23). The ion trajectories may change into neutral atom trajectories without change in direction: Thus, the ions and neutral atoms will transport the same image but, upon reaching the converter (for example), the ions may undergo a contraction whereas the neutral atoms will not be subject to such a contraction, thus resulting in two

superposed images on the fluorescent screen.

On the other hand, it would be desirable to have the greatest part of the ion path contained within a clean vacuum free of organic vapors, so as to avoid or at least retard the contamination of the converter cathode, which would lead to a lowering of the yield in secondary electrons and thus to a reduction of the electron image luminosity.

2. Pumping

In our experimental apparatus, we restricted the design to technically realizable solutions without excessive complication. For practical reasons, we also limited our projects to the realization of a vacuum of 10^{-6} mm Hg in the space ahead of the contrast diaphragm and of a vacuum of 10^{-7} mm Hg along the ion path after the diaphragm. [27]

It would seem that the use of rubber gaskets to ensure a tight seal of the vacuum enclosure makes a mechanical shifting of the object especially easy. However, the presence of such gaskets limits the vacuum that can be expected. In addition, as discussed below, an adjustable gas leak is used for feeding the ion gun; the evacuation of the excess gas introduced requires auxiliary pumping. To obtain a vacuum much higher than 10^{-6} mm Hg in the zone ahead of the dia- phragm, a considerable increase in the degree of such pumping would be neces- sary. Using certain precautions, a vacuum of 10^{-6} mm Hg can be rapidly re- established after introducing an object, thus permitting a frequent change of specimens and giving considerable experimental flexibility to the apparatus.

In front of the diaphragm, the secondary ions traverse a distance of only a few centimeters, which means that their diffusion on the residual gas does not require a vacuum of 10^{-6} mm Hg but, conversely, such a vacuum is insufficient

68

for completely avoiding the formation of a surface film on the specimen.

Downstream of the contrast diaphragm, the realization of a vacuum of 10^{-7} mm Hg can be expected. In this region of "better vacuum", the oil vapors from the diffusion pump are stopped by a liquid nitrogen trap; tightness is ensured by indium metal seals and the castings used there are carefully cleansed. Particularly, the use of any organic solvent is prohibited so as to prevent the always possible propagation of a thin film of organic matter over the surface of the cleansed castings. Unfortunately, it is difficult to perfect the quality of the vacuum by hot degassing since the optical systems used in constructing the apparatus cannot be subjected to such treatments without damage.

In detail, the layout of the pumping system is as follows: A diffusion pump with a capacity of the order of 50 ltr/sec removes the excess gas, introduced into the ion gun by an adjustable leak. A fractional diffusion pump, whose limit vacuum is 5×10^{-7} torr at a capacity of 150 ltr/sec maintains the vacuum in the zone located ahead of the contrast diaphragm, which we will designate as "object space". Finally, downstream or after the contrast diaphragm, in the so-called "image space", the vacuum is obtained over the intermediary of a fractional diffusion pump with an output of 600 ltr/sec, supplemented by a liquid nitrogen trap. The requirements of placement of this pumping system are the determining factors for the substructure of the experimental equipment.

3. Description of the Equipment

a. Overall Unit and Central Part

The entire unit is mounted on a parallelepiped baseplate of welded angle irons. At the center of the baseplate, a cylindrical pipe T (see Fig.17,

Plate VII) of stainless amagnetic steel, terminated by two cheek plates, rests

on its lower base. From the lower cheek plate, the liquid nitrogen trap and

the adaptable diffusion pump are suspended. The pipe serves as pumping link

between the diffusion pump and the central part C mounted to the upper cheek

plate of the pipe. This central casting C, made of amagnetic stainless steel,

accommodates on the right the "object part", on the left the "image part", and

at the rear the deflecting electromagnet. The air gap of the electromagnet runs

along a horizontal tongue machined into the body of the part C. A groove,

milled into this tongue, permits passage of the beam between the pole faces of

the magnetic prism and osculates over its entire length a bore centered on the

bore of the pipe T. Two other conduits also end in this bore which, one on the

right and the other on the left, permit pumping of the space following the con-

trast diaphragm and of the "image space". In this arrangement, the groove in

which the beam circulates is pumped down directly and the fact that the casting

C is machined of one block eliminates, as far as possible, the use of seals and

thus the risk of leakage.

Machining of the casting C must be done with extreme care since it is used

as reference point for adjusting the optical axis of the "object part" as well

as that of the "image part" in the plane of symmetry of the air gap.

b. Object Part

The object part (Fig.18 and Plate VIII) comprises the ion gun and its con-

denser, the immersion lens, and the object support. These various elements are

arranged with respect to a central duralumin body D in which the vacuum is pro-

duced by means of the diffusion pump P_2 connected with the casting C.

a) Ion gun. The ions used are generally argon ions and occasionally hydro-

gen ions. The gas is introduced through a controllable leak into a glass am-

poule where a plasma is maintained by means of a high-frequency discharge. The

excitation of the plasma is produced over the intermediary of two copper rings

circling the ampoule (capacitive coupling) and connected to a 60-watt high-

frequency source, oscillating at 100 mc. The plasma is brought to a high posi-

tive potential of 10 kv by means of the electrode 1 (see Fig.19). The potential
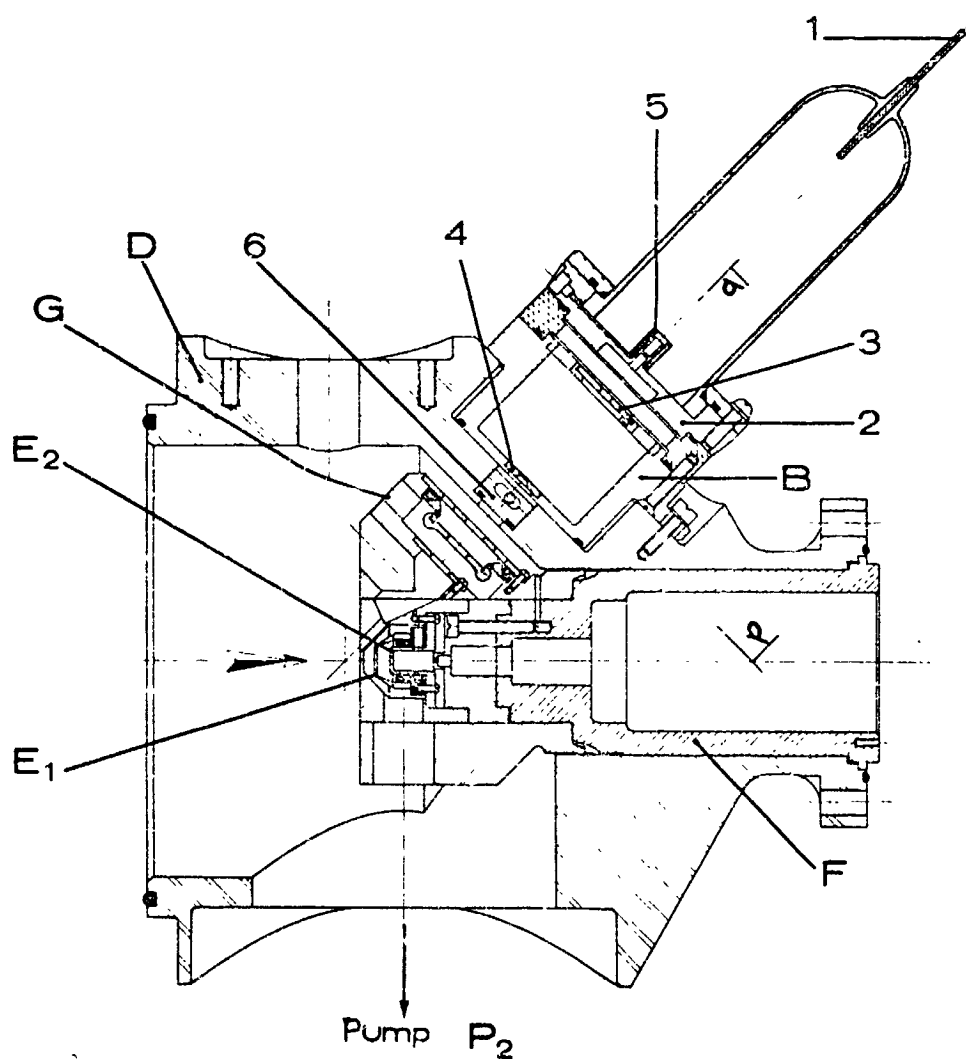

Fig.19

drop which extracts the ions from the plasma takes place between the lower limit of the plasma, frequently marked by a luminous sheath, and the extracting electrode 2 brought to a potential which is controllable about a value of approximately 9 kv. The extracting electrode, made of a small channel with a constriction at the center, is surrounded by a quartz cylinder which, while retaining the positive charges, repels the ions and thus plays the role of a /28 Wehnelt. The extracting electrode, cut into a duralumin casting on which the base of the glass ampoule is resting, is fitted into an insulating washer of araldite which, in turn, is attached to a base B. This base or shoulder carries the electrode 3, at mass potential, which postaccelerates the ions extracted from the plasma, as well as a diaphragm 4 having a diameter of 3 mm and limiting the aperture of the ion beam; in addition, this shoulder is connected, over a flexible tombac membrane, to the diffusion pump P_1 which ensures evacuation of the gas escaping through the ion exit hole 5.

The base B rests on a plane milled into the duralumin body D and inclined by 45° with respect to the axis of the immersion lens. The base is slidable along this plane, which permits centering of the gun, with vacuum tightness being ensured by a toric joint. The gun space can be insulated from the immersion-lens space by means of an airlock 6 located directly below the diaphragm 4.

The density of the ions, arriving at the target, must be sufficient to prevent the phenomenon of contamination which would manifest itself by the deposit of a carbonized layer. In addition, the luminosity of the images will depend on the "illumination" density of the object. Therefore, it is necessary to insert a condenser for concentrating the ion beam on the target. This condenser simply consists of a unipotential electrostatic lens with three diaphragms. The condenser is placed as close as possible to the object so as to

72

give a reduced image of the source hole 5. This will make it possible to obtain an argon ion beam of about 20 μamp having an energy of 10 Kev and con- centrated in a spot which, because of the inclination of the beam relative to the target, has dimensions that differ in two perpendicular directions and measures about 0.5 mm by 1 mm.

The condenser has a fixed position with respect to the immersion lens, while the gun assembly can be displaced for centering the primary beam on the target.

b) Immersion lens. The immersion lens consists of an amagnetic stainless steel cylinder whose base, turned toward the object, is plane, carefully polished, and pierced at its center by an orifice O with a diameter of 0.5 mm. Three channels of 3 mm diameter end on this plane face at 120°, arranged symmetrically around the orifice O and having axes that intersect the axis of the
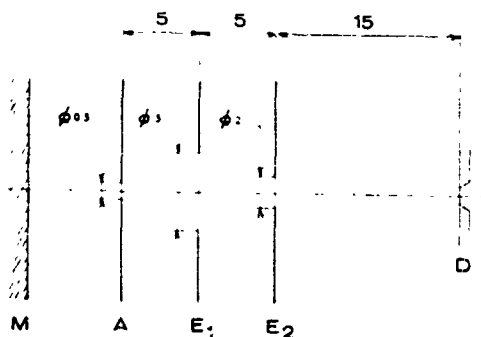

Fig.20

orifice by making, with this latter, an angle of 45°. The ion beam arrives through one of these channels; the two other channels, for the time being, are used only for establishing the symmetry of the electric field but could possibly be used later for permitting passage of auxiliary bombarding beams.

The inside of the stainless steel cylinder is bored so as to accommodate the mounting of electrodes E_1 and E_2. The electrode E_1, brought to a high positive potential, is insulated on a support of araldite. The lead-in for the voltage goes through an aperture made in the lateral wall of the cylinder, while other ports arranged symmetrically over this wall represent feedthroughs for facilitating the pumping of this region. The two electrodes E_1 and E_2 made of amagnetic stainless steel, are carefully polished and can be centered under the microscope with respect to the axis of the orifice O. Similarly, the contrast diaphragm can also be slid under the microscope relative to the immersion lens assembly. Figure 20 gives the principal dimensions.

The immersion lens is aligned with the casting G which simultaneously serves as support for the condenser, in such a manner that the optical axis of the condenser coincides with the axis of one of the inlet channels for the primary beam. The piece G is aligned on another piece F which carries the immersion lens and is centered on the casting C. The base of the duralumin body D engages the piece F and flanges the assembly to the casting C.

c) <u>Object stage</u>. The objects generally are formed by disks of 20 mm diameter. They are secured in a dismountable cartridge (Fig.21) mounted to the end of a rod whose axis must be parallel to the axis of the lens. The motion of the rod along its axis is controlled by a threading, so that the distance of the object with respect to the face of the lens is controllable and checkable. The interior of this hollow rod is laid out so as to ensure airtight passage for the lead-in of the potential to the object.

This shaft is carried by a cheek plate, resting on the rear of the body D in such manner as to keep the axis of the shaft parallel to the axis of the lens, which ensures parallelism of the object surface with the lens face. To

observe various zones of the specimen, the object must be displaceable in the plane of its surface. This motion is made possible by sliding the cheek plate with respect to the body D, by means of screws attached to knurled knobs, in two directions at 90°, which can be done without special precautions since the image is observed at a direct magnification of the order of 250. Airtightness is obtained by a toric joint of limited compression since the cheek plate rests directly on the body D.

This plate also has an airlock which permits insertion of the object into the vacuum enclosure and withdrawal, without destroying the vacuum. The design of this airlock is quite simple: The hole pierced into the cheek plate for passage of the object-stage shaft can be hermetically sealed by a movable disk provided with a toric joint. The object-stage shaft slides along a toric joint and can be pulled backward. Thus, for insulating the vacuum enclosure it is sufficient to put the disk in place. A grooved ring permits detaching the object-stage shaft still pushed down by the atmospheric pressure. To insert the object, the process is reversed. Since there is no forepumping in the airlock, a small amount of air will penetrate into the vacuum enclosure together with the object. However, this does not interfere greatly; one or two minutes after operating the airlock, the vacuum is practically restored to its previous value, i.e., to about the degassing of the specimen.

Finally, it should be mentioned that the object space is pumped down over a bore of 100 mm diameter, drilled into the body D. The object part assembly is held by the jack V_1 so that no mechanical effect can interfere with the centering of the object part on the central casting C.

c. Electromagnet

So as to reduce the surface of the air gap and thus also the dimensions

of the magnetic circuit, of the excitation coils, and of the electric lead-ins, the pole pieces of the electromagnet follow the shape of the mean trajectory. /30

Fig.21

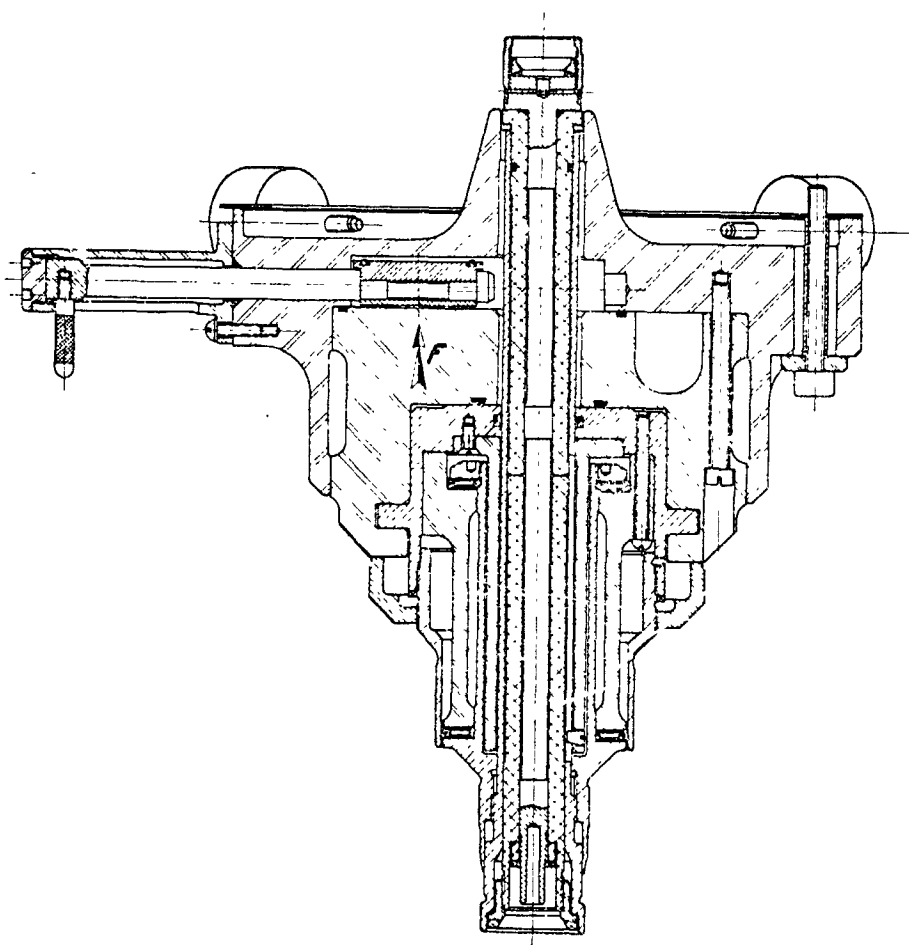These pole pieces are projected onto the radial plane along two circular arcs, intersected by two segments of a straight line in RSTU (Fig.22), where the angle of the normal to each of these segments with the axis of the beam is, respect- ively, equal to the angle of incidence and the angle of exit of the beam. So as to have the magnetic field maintain a sufficient homogeneity along the ion

76

path within the air gap, the difference in the radii of the arcs $\widehat{RU}$ and $\widehat{ST}$ is made equal to four times the width of the air gap. It 　　　.ible to attach
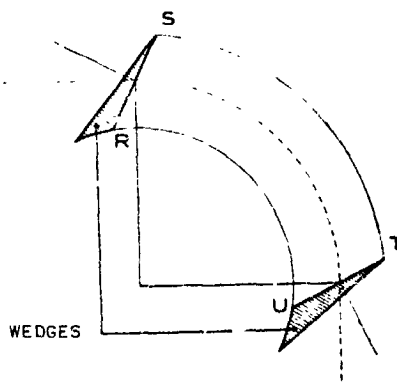
Fig.22

soft iron wedges to the plane faces projecting along the segments RS and TU, which permits setting the angles of incidence and exit to their optimum value . These wedges are carefully aligned so as to maintain a constant air gap.

The electromagnet is supported on three jacks by which the orientation of the plane of symmetry of the air gap in space can be controlled. The jacks, in turn, are mounted to a baseplate which can be displaced in two perpendicular directions; this arrangement ensures control of the magnet position with respect to the casting C and thus with respect to the "object part" and to the " image /31 part" which are adapted to this piece.

The electromagnet is fed by a DC source with an output variable between 0 and 7 amp and a voltage variable between 0 and 45 v; the intensity of this source is stabilized to within a few tenthousandths. A mechanical drive of the control potentiometer permits a regular and slow sweep of the magnetic induction which thus can vary from 0 to 10,000 gauss in an air gap of 1 cm width.

77

d. "Image Part"

The image part comprises the selection slit, the stigmatizer, the tele-
photo lens, and the image converter. A duralumin casing K bounds the vacuum
enclosure containing this assembly, whose arrangement is shown in the schematic
sketch of Fig.23.
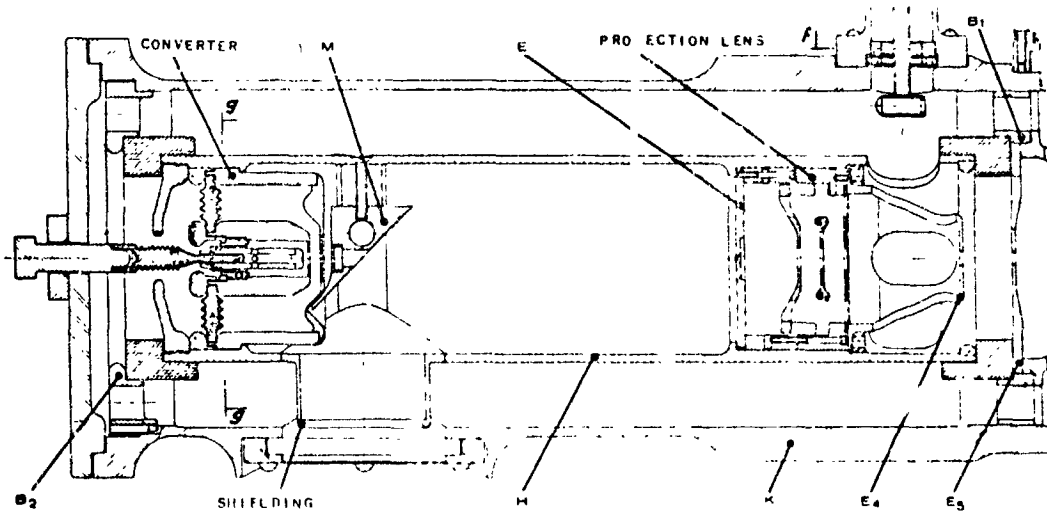
Fig.23

a) Assembly. The Armco iron tube H is brought to the negative potential
of the postacceleration. The image converter is centered at one of the extremi-
ties and is followed by a mirror M which reflects the luminous image observed
on the fluorescent screen E. The mirror has a hole at the center for passing
the ion beam in the forward direction and the electron beam in the return direc-
tion. The fluorescent screen also is provided with a small hole for allowing
passage of the ion beam. Behind the fluorescent screen, the projection lens
and the elements of postacceleration are installed. The tube is capped at each
end by a glass washer. These washers are fitted into two flanges B_1 and B_2 of

amagnetic stainless steel, and are clamped by four long rods. The flanges B_1 and B_2 are fitted into the casing and thus center the tube H. In addition, the first postaccelerating electrode is attached to the flange B_1, together with the selection slit and the astigmatism compensator. It should be mentioned that the flanges are perforated so as to permit pumping between tube and casing.

b) Image converter. The electrodes of the converter are made of stainless steel and highly polished. The anode, carried by a sheath which fits into the tube H, is at the postacceleration potential. The Wehnelt, insulated from the anode, fits into an araldite disk centered on this sheath.

Inside the Wehnelt, the cathode which is electrically insulated by an araldite sleeve, can be adjusted in depth during operation. A coaxial voltage lead-in provides lateral feeding of both Wehnelt and cathode.

The focusing is done either by adjusting the cathode in depth or by applying, to the Wehnelt, a voltage slightly differing from that of the cathode. To take up the field curvature, the cathode is given the shape of a concave spherical calotte whose axis is centered by design on that of the anode and of the Wehnelt. In addition, so as to eliminate the images produced by a possible structuring of the cathode, the latter is carefully polished; aluminum vapor deposition on its surface greatly improves the secondary electron emission coefficient and, consequently, the luminosity of the images.

c) Mirror. The converter is followed by the plane mirror M which is optically polished to a quarter interfringe and has a center orifice for passing the beams. A diaphragm, inserted into this hole, protects the converter anode from possible contact with the ion beam. The plane of the mirror is inclined by $45°$ to the converter axis, which means that the image of the fluorescent screen is reflected at $90°$. For observation, windows or apertures are cut into

79

the tube H and the casing. The hole in the casing is hermetically sealed by a glass port. Since the tube H is brought to a negative potential, an electric field is present between the casing and the tube H which leaks through the hole pierced into the tube H. This electric field slightly repels the ion beam on its forward path and attracts the electron beam on the return path. The two effects combine, resulting in a considerable displacement of the electron image on the fluorescent screen. This effect can be greatly reduced by attaching a metal shield to the hole, pushed fairly close to the glass port.

d) Telephoto lens. The telephoto lens system comprises the actual projection lens and the postacceleration device. The electrodes are made of amagnetic stainless steel and highly polished, as is conventional for electrostatic lenses.

The projection lens can be centered under the microscope although this is not absolutely necessary. In this arrangement, the central electrode is supported by three insulating rods which reduces the insulator surface and leaves the largest possible space for pumping. The three electrodes are housed in a small casing which fits into the tube H and on which the fluorescent screen is centered.

The two postaccelerating electrodes are perforated by rectangular holes along the outer rim so as to ensure better pumping of the interelectrode space.

e) Selection slit, astigmatism compensator. The selection slit consists of two platinum foils, held in place by two stainless steel rims. Originally stationary, the two rims of the slit were later made mobile so as to permit an adjustment of the slit width during operation.

The astigmatism compensator is a hexapole of conventional type. A total of six rods of 3 mm diameter are distributed at $60°$ over an insulating ring. Each

two opposite rods are electrically coupled. The power supply is by two 12-v
batteries connected in series and branched to a potentiometer which permits an
adjustment of the magnitude of the correction to be applied. A sine potentio-
meter with three outputs is connected to each rod pair, thus ensuring control
"in direction" of this correction.

4. Power Supply for the Unit

The potential of the object is fixed by a high positive voltage, stabi-
lized to within several ten thousandths and variable from 100 to 5000 v. Be-
tween the object and ground, a plug potentiometer, with a total resistance of
5 MΩ, is installed which furnishes the voltages for feeding the immersion lens
and the projection lens. The fine adjustment of the voltage applied to each of
these lenses is obtained by supplementing the voltage tapped from one of the
terminals by a variable voltage furnished by an insulated potentiometer mount-
ing, coupled to dry cells charged to high voltage.

The cathode of the converter is directly fed by a negative high voltage,
adjustable in kilovolt steps from 0 to 50 kv. The voltage of the Wehnelt can be
regulated by means of an insulated potentiometer, coupled to high-voltage cell.
A fraction of the negative high voltage, tapped from a plug potentiometer with a
total resistance of 2000 MΩ, is applied to the tube H and fixes the postacceler-
ating potential.

The positive high voltage of 10 kv, used for extraction, acceleration, and
focusing of the primary ions, is simply rectified and filtered. The various
voltages are tapped from a plug potentiometer.

In the object part, the voltage lead-ins which are vacuumtight are held by
an insulated sleeve of araldite. In the image part, the voltage feedthrough

insulator is of fritted alumina, brazed to titanium metal castings. Vacuum-tightness is obtained in the first case by toric rubber gaskets and in the second case by indium metal joints.

5. Focusing Experiments

a. Investigation on Focal Lines

We have shown above that the presence of stray fields changes the position of the focal lines produced by the magnetic prism and that the resultant difficulties can be solved by making use of the hypothesis of an equivalent magnet. The characteristics of such a magnet are determined from the real magnet, giving the symmetric positions of focusing. The experimental investigation of the symmetry conditions proceeds as follows: Iron wedges plated to the faces of the pole pieces of the electromagnet permit to vary the entrance and exit angles of the beam in the prism and thus to modify the convergence of the prism in the two principal sections. Two different methods are in question to obtain the desired result. The first method consists in first defining the topography of the stray field in the radial plane and then calculating the trajectories. Such recording should be done for each angle wedge since the "magnetic faces" are not necessarily parallel to the mechanical faces. The second method, which we used, consists in visually displaying the focal lines, which avoids the delicate operation of plotting and also yields a complete integration of the trajectories. First, the angle wedge which results in stigmatism of the prism is defined for a given position of the crossover. After this, the position of the crossover object must be varied until the symmetry conditions of focusing are obtained. However, the problem can be made less strict by referring to Hennequin's results and by using the curves of the stray field given in the literature to perform an

approximate calculation of the positions of symmetric focusing.

a) <u>Experimental assemblies</u>. Speaking generally, electron optics is a process much easier to handle than ion optics. Therefore, in our first experiments, we replaced the above-described object part by an electron gun whose distance with respect to the entrance face of the magnet could be varied, and replaced the image part by a fluorescent screen whose distance from the exit face of the magnet could be varied. However, the resultant assembly has one serious drawback: The remanent induction of the electromagnet was sufficient to cause a rotation of the electron beam, which resulted in operating conditions far from those in which the magnet can be effectively used. Therefore, it became necessary to substitute ions for the electrons despite the fact that this resulted in a complication of the detection process.

The ion source consists of the electron gun in which a tungsten filament, having a lithium aluminosilicate loop fused to its tip, replaces the conventional filament. It is generally known (Bibl.30) that such a filament, when heated, emits Li^+ ions. An ion-to-electron converter, similar to the one described above, serves as receiver for displaying the focal lines. The photograph in the Appendix (Fig.24, Plate VIII) shows the device for detecting the focal lines. The brass tube 1 carries at one end the converter itself and, at the other end, the fluorescent screen. Through the orifice in the tube 1, the mirror 2 inclined at 45° and reflecting the image of the fluorescent screen can be viewed, thus showing the hole at the center of the screen for passage of the ion beam. The assembly is mounted to a pipe 3 which slides along a toric joint. The hollow rod 4, extending along the axis of this pipe, feeds negative high voltage to the cathode; polarization of the Wehnelt, at a voltage slightly differing from that of the cathode, takes place across the tube 4. A spring attached to

the tube 1 grounds the anode of the converter by rubbing along the interior bore of the duralumin body 5. The aperture, milled into the casting 5 is closed by a transparent plexiglas sheet. Airtightness is obtained by toric joints, since the quality of the vacuum is not of extreme importance in the investigations of focal lines. In addition, a plexiglas handle attached to the extremity of the pipe 3 permits pushing and pulling of the detector assembly and to thus vary its position with respect to the exit face of the magnet.

The ion focal line is formed on the converter cathode which produces an electron image amplified several times. To have the passage of the ion beam proceed without intersecting the rays at the height of the fluorescent screen, the hole in this screen must have sufficiently large dimensions (several milli-meters). Therefore, it is to be expected that the electron image of a given focal line will be prevented from forming on this hole and thus cannot be observed. Fortunately, the stray field of the magnet is still sufficient at this level for slightly deflecting the electrons so that the image will form outside of the hole.

b) Results. With this experimental setup we were able to determine that the angle of incidence and the angle of exit of the real magnet was $32°30'$ and that the radius of curvature was 117 mm; let us recall that these values for a theoretical magnet are, respectively, $26°30'$ and 100 mm. These data permit proper placement of both object part and image part. In addition, by changing the properties of the aluminosilicate, an emission of K^+ and Cs^+ ions can be obtained, proving that the saturation of the soft iron in the electromagnet has practically no influence on the position of the focal lines.

b. Preliminary Adjustment of the Converter

For adjusting the converter, the cathode is illuminated with Al^+ ions

(selected because of their high emission intensity). By then varying either the cathode depth or the excitation of the Wehnelt, the few defects which still persist on the surface after polishing can be compensated. To obtain the conditions under which the converter would introduce a minimum of distortion, it is preferable to electrically couple the Wehnelt with the cathode and to only vary the depth of the latter. However, this focusing method is insufficient since it does not permit checking whether the curvature of the cathode properly corrects the curvature of the field and also does not give data on the enlargement produced by the converter of an ion image outlined on the cathode.

If the image of the cathode surface is to be reproduced, it is necessary to give a distinct structure to the cathode. For this purpose, a copper screen of 25 μ mesh is impressed on a concave aluminum cathode, using a steel ball. The difference in electron emission on aluminum and on copper is responsible for the contrast observed on the image (Plate I, Fig.c). On hand of an enlargement, it can be estimated that the limit of resolution introduced by the converter is about 5 μ; otherwise, the image is sharp up to the very edge. A small straight-edge photographed at the same distance as the fluorescent screen gives an indication (Plate I, Fig.c) that the converter enlarges 16 times. If an ion image arrives on the cathode, enlarged by about 15 times, the final magnification will be 250 and the limit of resolution, with reference to the object, will be one third of a micron.

Obviously, the spots appearing on the micrograph of Fig.c (Plate I) are due to faulty impression of the screen on the cathode or by defects of the screen itself.

6. Observation of Ion Images

The objects used for adjusting the optical system consist of a copper screen

85

pressed into an aluminum block. This permits a direct observation of the final magnification of the image and measurement of the resultant distortion.

a. <u>Adjustment of the Optical System</u>

As described above, the converter is adjusted by focusing on a few small markings remaining on the cathode surface after polishing.

In any type of adjustment of the telephoto lens, a focusing by the emission lens is absolutely impossible since the chromatic fog completely washes out the image. On varying the excitation of the telephoto lens, there will finally arrive a moment at which this lens is sighted on a plane not too far removed from the achromatic plane, which then permits a rough focusing of the image. On a minor modification of the magnitude of the magnetic field, the image will shift. In fact, even a slight change in the magnetic field is equivalent to a change in the energy of the ions; this will result in a rotation of the trajectories about the chromatic focal line which, in turn, produces movement of the image. On changing the focusing of the emission lens, the position of the initial image I_0 is changed and, consequently, the position of the radial focal line I_0'. Consequently, the next adjustment consists in making the radial focal line coincide with the chromatic focal line. By successive resetting, the excitation of the telephoto lens can be so adjusted that a slight modification in the magnetic field will no longer shift the image, so that proper focusing can be obtained by varying the emission lens. Incidentally, the progress of adjustment is easily checked by simply noting the improvement in the image which gradually loses its chromatic blur. This finally leaves the astigmatism to be corrected by means of a stigmatizer, so as to obtain optimum image quality.

During this latter operation, the fluorescent screen is observed through an

eyepiece which magnifies 4 - 5 ×. To make the astigmatism correction easier,
the screen object is replaced by an object into which small cells of a high-
emission substance are embedded (or deposited) in such a manner as to obtain
brilliant spots contrasting with a dark background. Finally, it is also pos-
sible to improve the adjustment of the converter since the focusing on the re-
sidual particles on the cathode is not very accurate.

The direct magnification of the image on the screen may vary between 180
and 300, and the observed field may fluctuate between 0.2 and 0.28 mm. The
various magnifications are obtained either by separately modifying the excita-
tion of the two lenses of the telephoto lens system in such a manner as to pro-
ject a more or less enlarged image onto the converter cathode while sighting
the achromatic plane or else by more or less approaching the object to the first
face of the emission lens while retaining the focusing of the image on the
plane I_0 by varying the excitation of the lens. So far as the dimensions of
the observed field are concerned, they are basically limited by the diaphragm
inserted in front of the converter. The fluorescent screen on which the images
are observed is photographed from outside, using a camera which can be retracted
for visual observation.

b. Ion Images

The micrograph in Fig.d (Plate I) was taken on a screen object with Al^+
ions. The black lines correspond to the absence of aluminum and thus represer
the bars of the copper screen. To the upper right of the micrograph, the effects
of sputtering are clearly defined. The copper screen actually has only a
thickness of 8 μ; eroded by the ion bombardment, this screen is gradually con-
sumed within a few minutes, leaving an imprint in the aluminum matrix which can

be easily detected by a relief effect. In this particular experiment, the centering of the ion beam on the target is slightly shifted so that the etching pressure can be observed.

The Cu^{+63} ions also give images, but of a much weaker luminosity. The bars of the screen appear light on a dark background and the obtained image represents more or less the negative of the image given by the aluminum. In addition, it is obvious that the distortion introduced by the magnet is negligible and that the distortion of the projection lens is practically compensated by that of the converter.

We then investigated a crude foundry Al-Mg-Si allo", The micrographs (Fig.a, b, c, Plate II) show the images obtained, respectively, with Mg^{+24}, Al^{+27}, and Si^{+28} ions. The precipitates of Mg_2Si, in the form of dendrites, appear bright on a black background on the images formed with Mg^+ and Si^+ ions, whereas they appear dark on the image obtained with Al^+ ions. On the other hand, the silicon distribution image shows brilliant conglomerates whose appearance on the aluminum distribution image is marked by a more or less pronounced shading which does not appear on the magnesium image; this means that a segregation of silicon is involved. In addition, the precipitates do not contrast with a completely dark background as is the case for magnesium, which means that the silicon is also dissolved in the aluminum matrix. This assumption is confirmed by investigation with an electron microprobe. We would like to mention that these images were taken with a contrast diaphragm of 0.4 mm and that the shielding had not yet been placed on the viewing port, so that the displacement of the image with respect to the hole for passage of the ion beam through the fluorescent screen is clearly defined.

7. Resolving Power

Obviously, the analysis method described here makes it possible to auto-matically obtain the distribution diagram of a given element at the specimen surface, in the form of a characteristic image. The first question that comes to mind is that of the resolving power that can be expected of this image.

a. Limitations due to the Optical System /35

The resolving power is primarily limited by the aberrations of the optical system used. This system comprises the initial emission lens, the magnetic prism, the electrostatic telephotolens, and the image converter. For a given diameter of the contrast diaphragm, we have demonstrated that the magnetic prism influences the chromatic aberration image and the aperture defects, which are negligible with respect to the limit of resolution of the emission lens, and that only the field astigmatism aberrations are manifest along the edge of the observed image. In the apparatus designed by us, for a contrast diaphragm of 0.4 mm and an imaged field of 0.2 mm, the field astigmatism aberrations along the edge are of the order of 0.5 μ with respect to the object. In addition, the image converter introduces an aberration which, relative to the object, is of the order of 0.3 μ.

The role of the electrostatic telephoto lens is that of projecting the filtered ion image; consequently, this lens only introduces a distortion on the image which is readily compensated by that of the converter. Finally, with a contrast diaphragm of 0.4 mm diameter, the lens system used introduces aberra-tions that permit a limit of resolution of 1.1 μ at the center and of 1.6 μ along the edges of a field of 0.2 mm. With a contrast diaphragm of 0.2 mm, a

89

limit of resolution below 1 μ over the entire field of 0.2 mm can be obtained.
In all this, we have disregarded the chromatic aberrations introduced by the
lens L since it is difficult to define to what extent these aberrations limit
the resolution and influence the image contrast. The micrograph (Fig.a,
Plate I) taken with Al^+ ions on a crude foundry Al-Mg-Si alloy shows fine Mg_2Si
precipitates which appear dark on the image, giving an idea of the image quality
obtained with a diaphragm of 0.2 mm. The micrograph in Fig.b (Plate I) refers
to another region of the same alloy, but the image is here formed by Mg^{+24} ions.

b. Ultimate Resolving Power

Another question is that of the final resolving power obtainable with the
above method, beyond the present capacity of our experimental apparatus. By
increasing the enlargement of the image given by the emission lens, the limita-
tions on the resolving power introduced by the remainder of the optical system
become negligible, so that – in the final analysis – it is the itial emission
lens which limits the resolving power. However, this latter can be improved at
will by reducing the diameter of the contrast diaphragm, placed in the crossover
of the lens. Thus, it seems a priori that no basic limitation exists for the
resolving power of the analysis; it is a fact that nowhere in this method do we
have anything like the limitation placed (for example) on the resolving power
of an electron probe microanalyzer by the diffuse penetration of primary par-
ticles into the interior of the specimen; in fact, the incident ions in our
method penetrate only a few tens of angstroms into the target.

Nevertheless, there is another limitation of the resolving power of the
analysis by secondary ion emission; this limitation is due to the process used
for forming the ion image. The ions that contribute to the formation of the

90

image are extracted from the specimen itself. However, not only is the number of characteristic ions produced by a given bombardment generally lower than that of the neutral atoms simultaneously extracted from the specimen but, in addition, the diaphragm inserted at the crossover of the emission lens permits passage of only a small portion of the emitted characteristic ions. This would indicate that the sputtering of a minimum volume of matter would be necessary to obtain a sufficient number of characteristic ions for the formation of each element of the image. This naturally leads to a limitation of the ultimate resolving power of the analysis.

This ultimate resolving power can be estimated as follows: Let ϵ be the limit of resolution and let p % be the accuracy that must be obtained for a quantitative analysis of the elementary volume ϵ^3. At the onset, let us imagine the ideal case in which rigorous calibration curves make it possible to defin without noticeable error, the concentrations of the various elements from the intensity of their ion emission and where the ion emissions themselves are measured with an absolute accuracy (which means to say that the receiver device counts the arrival of individual ions); however, in this case the accuracy with which a local concentration can be determined will be limited by the statistical fluctuations that affect the number of characteristic ions emitted per element- ary volume, fluctuations which are equal to the inverse of the square root of this number of ions. An accuracy of p % in the measuring of the concentration can thus be obtained only if the number of characteristic ions emitted per ele- mentary volume ϵ^3 is at least equal to $10^4/p^2$. This indicates clearly that the essential factor, entering the calculation of the ultimate resolving power, is the efficiency of production of secondary ions, i.e., the ratio n_1/n_0 of the number n_1 of characteristic ions contributing to the formation of the image of

a given region to the number n_0 of neutral atoms simultaneously extracted from the same region. This ratio is lower the smaller the contrast diaphragm of the emission lens; as soon as the limitation of lateral velocity, imposed by this diaphragm, is much lower than the mean emission velocity of secondary ions, it can be assumed that the ratio n_i/n_0 is proportional to the surface of this dia-phragm and thus proportional to the limit of resolution of the image furnished by the emission lens.

Therefore, it is not necessary to determine the ratio n_i/n_0 for each value of ϵ; it is sufficient to determine n_i/n_0 for one particular case. The meas- urements were made for a diaphragm adjusted such that the lens had a resolving power of $1\,\mu$. Denoting by $\left(\dfrac{n_i}{n_0}\right)_{exp}$ the value of the ratio determined under these conditions, it can be assumed that, as long as ϵ remains below or equal to $1\,\mu$, the "yield of secondary ions" $\left(\dfrac{n_i}{n_0}\right)_\epsilon$ obtained at the resolving power ϵ is given by the relation

$$\left(\frac{n_i}{n_0}\right)_\epsilon = \epsilon \left(\frac{n_i}{n_0}\right)_{exp} , \quad \text{where } \epsilon \text{ is expressed in microns.}$$

This will yield

$$\epsilon \left(\frac{n_i}{n_0}\right)_{exp} = \left(\frac{n_i}{n_0}\right)_\epsilon = \frac{n_i(\epsilon)}{n_0(\epsilon)}.$$

It is sufficient to replace, in this expression, the quantity $n^i(\epsilon)$ by its min-imal value $10^4/p^2$ and to note that $n_0(\epsilon)$ is equal to $K\epsilon^3$ where K is a constant representing the number of atoms contained in a volume of the specimen equal to $1\,\mu^3$ (K being of the order of 6×10^{10}) so as to obtain finally the relation

$$\epsilon = 10\, K^{-1/4} p^{-1/2} \left(\frac{n_i}{n_0}\right)_{exp}^{-1/4} \text{microns.}$$

The ratio $(n_i/n_0)_{exp}$ naturally depends on the concentration of the element

sought; it also depends greatly on the nature of this element and on the nature of the compound in which the element is contained. It will be shown that the ratios $(n_i/n_0)_{exp}$, measured in the case of aluminum and of copper, have values, respectively, of the order of 10^{-3} and 5×10^{-7}.

To establish the concept, we will assume an accuracy of 10% for the quantitative analysis (p = 10) thus finding, under the experimental conditions of the apparatus (where the extracting field at the object surface is 10 kv/cm), an ultimate resolving power of the order of 350 Å for the case of aluminum and of 0.35 μ for the case of copper. It is possible to improve this ultimate resolving power by increasing the electric field of ion extraction. In fact, by increasing the extracting field and by adjusting the diameter of the contrast diaphragm in such a manner as to permit passage only of ions whose lateral energy is equal or below 1 ev, for example, the limit of resolution of the emission lens can be improved without reducing the number of ions participating in the formation of the image. Let us mention that, on returning to a limit of resolution of 1 μ for the emission lens, the diaphragm of this lens will permit passage of ions whose lateral energy is above 1 ev so that there will be an increase in the number of ions contributing to the formation of the image. For the same rate of sputtering, this leads to a higher ion yield $\left(\frac{n_i}{n_0}\right)_{exp}$. One can also hope to increase the secondary ion yield by a suitable selection of the bombardment conditions: nature, energy, and angle of incidence of the primary particles. As it is, this resolving power is already clearly superior to that obtained with an electron-probe microanalyzer for the case of solid specimens. However, it will be shown later that the electron-probe microanalyzer remains superior for an analysis by secondary ion emission so far as the possibility of accurate quantitative analyses by convenient methods is concerned.

CHAPTER III

SOME RESULTS ON SECONDARY ION EMISSION

So as to have the above-obtained images of ion distribution become useful for microanalysis, it is necessary to conduct further studies on the basic characteristics of secondary ion emission. For this purpose, a measuring and recording device for secondary ion currents is substituted for the "image part"; the apparatus can then be used as a simple mass spectrograph.

1. Experimental Setup

Measurement of the secondary ion current is made by means of a Faraday cylinder coupled to a DC amplifier and an oscillating capacitor. The Faraday cylinder is protected by a metal shield brought to a slightly negative potential so as to repel the secondary electrons produced by the impact of ions on the walls of the enclosure or on the base of the cylinder. A slit is placed in front of the assembly, at the level of the crossover image; its width is regulated by taking into consideration the aperture defects affecting the crossover. The measurements are also made by limiting the "lateral energy" of secondary ions to about 1 ev by means of a contrast diaphragm, placed at the crossover of the emission lens. A recorder, coupled to the DC amplifier, permits a direct tracing of the spectrum of the analyzed material.

2. Secondary Ion Emission   /37

It would be quite difficult to give a detailed and complete view over the phenomenon of secondary ion emission. In fact, excluding studies on the reflection or the diffusion of primary ions by the surface of the target, very

few reports have been published on the emission of characteristic positive ions.
Veksler and Benjaminovitch (Bibl.9) demonstrated that tantalum targets and
nickel targets emit, respectively, Ta^+ and Ni^+ ions when bombarded by Cs^+ ions
of 0.4 to 2.8 Kev energy. Their experiments demonstrate that the phenomenon
cannot be justified by a formula of the type given by Saha-Langmuir:

$$\frac{N_i}{N_a} = \exp \frac{e}{kT} (\varphi - V_i)$$

where N_i and N_a, respectively, are the numbers of secondary atoms and extracted
neutral atoms, while $e\varphi$ is the work function of one electron of the metal, V_i
is the ionization potential of a neutral particle, and T is the absolute tem-
perature of the target.

These authors actually determined a real yield which, for tantalum and
nickel, was 10^7 and 10^9 times higher than that indicated by the above formula.
However, this formula refers to the thermal vaporization of ions so that it is
not surprising that it is inadequate for the case of sputtering, where the
ejection velocities are considerably higher. It should be mentioned also that,
if the concept of a thermal process for explaining the phenomenon of secondary
ion emission is retained, it does not seem that the mean temperature of the
target would have to intervene directly. In fact, the impact of a primary ion
produces a local heating of the crystal lattice which is resorbed by collisions
between ions of the lattice and then, after a time equal to the lattice - elec-
tron relaxation time, by electron conductivity. Therefore, it seems more logi-
cal to use a "local temperature" of the lattice. Other authors (Bibl.9, 15)
observed the emission of Be^+, Mo^+, and Pt^+ ions sputtered from targets composed
of the corresponding metal. In the case of platinum, Bradley (Bibl.11) spe-
cifically was interested in ions originating in compounds formed from platinum,

from the viewpoint of his study on surface reactions. However, the nature of secondary ions may occasionally vary within surprising limits; thus, Honig (Bibl.12), in bombarding a silver target, found an impressive series of secondary ions where the Ag^+ ions accompanied, in equal quantity, the K^+ and Na^+ ions which would indicate the absence of specificity in secondary ion emission.

Our experiments naturally do not pretend to give a complete solution of the problem. We experimented only on a restricted number of elements and combinations of elements and under insufficiently varied conditions. For example, the apparatus used had basically been designed for the production of images which made it impossible to vary the conditions of bombardment. The specimens were bombarded almost exclusively with argon ions, arriving at the target under an angle of about 30° and with an energy of 7 Kev. No special precautions were taken for verifying the composition of the incident ion beam. The source of projectile ions is simply "rinsed" with argon for a certain time. Laboratory measurements (Bibl.27) showed that the energy dispersion of primary ions, in relative value, should be of the order of 5%.

However, an experimental setup produced in the laboratory (Bibl.28) made it possible to bombard the target with neutral atoms of argon having an energy of about 10 Kev. We were thus able to verify that the impact of fast neutral atoms produces sputtering of the target, under the emission of characteristic secondary ions. We also obtained distribution images, which would indicate that it is perfectly possible to substitute the bombardment with primary ions by a bombardment with fast neutral atoms. From the theoretical viewpoint, this result is of interest for understanding the mechanism of secondary ion emission; in fact, it is possible to confirm that the mechanical conditions of impact of the primary particles on the target are responsible for the degree of ionization

96

of secondary particles and that the charge of primary particles does not inter-vene in the ionization process.

3. Pure Elements

a. Nature of the Ions

Generally speaking, a metal M principally emits M atoms. If this metal is composed of a mixture of isotopes A, B, C, naturally A^+, B^+, C^+ ions will be obtained since the abundance ratios are maintained; this is shown, for example (Fig.25a), by the recording for magnesium which, as we recall, has three iso-topes Mg^{24}, Mg^{25}, and Mg^{26} whose respective abundance is 77.4%, 11.5%, and 11.1%. Besides these simple ions, there are also ions carrying multiple charges of the type M^{++} and molecular ions of the type M_n^+, although in a much weaker proportion. Thus, an aluminum target will yield Al^{+++}, Al^{++}, Al^+, Al_2^+, Al_3^+ ions. If the height of the spike Al^+ is taken as unity, the intensities of the corresponding spikes will, respectively, be 4×10^{-4}, 10^{-2}, 1.8×10^{-3}, and 3×10^{-4}.

a) Secondary ions with several charges. The intensity ratios of the peaks Al^{++} and Al^{+++} to the peak Al^+, given above, are directly measured. Since the ions Al^{++} and Al^{+++} carry, respectively, two and three elementary charges, the ratios of the number of doubly and triply ionized atoms to the number of singly ionized atoms are obtained by dividing the intensity ratios, respectively, /38 by two and three.

Otherwise, the filtering of ions in accordance with their "lateral energy" proceeds differently, depending on whether ions with a single charge or ions with multiple charges are involved. In fact, the process is exactly as though the ions of the type M^{p+}, on leaving the target, had a potential p times higher

than that of the simple ions, so that, provided that $e\varphi_{0a}$ is the maximum energy of the simple ions which pass through the diaphragm without being stopped, the ions of the type M^{p+} with an energy $p \cdot e\varphi_{0a}$ also pass without being stopped.

In the ratios given above, we thus counted the ions Al^{++} and Al^{+++} having energies twice or three times higher than those of simple ions. This is further complicated by the fact that the energy dispersion of the prism is independent of the charge carried by the ions and that, consequently, a portion of these ions with higher energy is eliminated by the selection slit.

It is possible to observe the images given by multiply charged ions since, in the electrostatic optical system used, the trajectories are independent of the charge-to-mass ratio of the ions that they contain. With the screen object, which we had used before, the image formed by the Al^{++} ions is completely identical to that obtained with Al^+ ions. Since the Al^{++} ions "see" an electric field twice as intense as do the Al^+ ions in the accelerating portion of the lens, one could believe that the image obtained with Al^{++} ions is of a higher quality. However, this is not the case since it was demonstrated above that the contrast diaphragm permits an integral passage of ions having a lateral energy twice as high; the resolving power of the lens remains unchanged.

Let us finally note that an element composed of a mixture of isotopes A, B, C may yield A^{++}, B^{++}, C^{++} ions In the case of magnesium, it can be confirmed that the isotope ratios are the same as those measured for simple ions.

b) Molecular ions. If an element is composed of an isotope mixture, the molecular ions are formed by the association of various isotopes among themselves. For example, the two-to-two combinations of three isotopes A, B, C give six possible groupings for ions of the type M_2^+:$(A - A)^+$, $(A - B)^+$, $(A - C)^+$, $(B - B)^+$, $(B - C)^+$ and $(C - C)^+$. For the case of magnesium, Fig.25b

98

shows a recording in which the masses 48, 49, 50, 51, and 52 appear; however, it will be found that there are five spikes instead of six which no doubt is due to the overlapping of the masses, meaning that the mass 50 can be produced by the combinations $(Mg^{24} - Mg^{26})$ and $(Mg^{25} - Mg^{25})$.
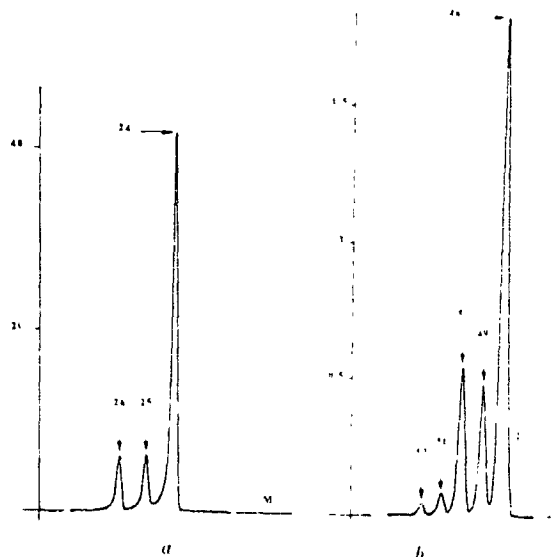
Fig.25

The images formed by the M_2^+ ions are easy to observe. For example, using the screen object we were able to observe an image made with Al_2^+ ions similar to that given by the Al^+ ions. This indicates that the molecular ions originate directly in the object or at least that they are formed in the immediate vicinity of its surface. Naturally, it can be conceived that ions of the type M_2^+ are produced by the association of an M^+ ion with a neutral atom M or else by the association of two M^+ ions, followed by neutralization of a charge, or finally by the ionization of a molecule M_2; however; these various processes – if they actually do take place – must occur in the immediate vicinity of the surface so as to make it possible to obtain an image.

b. <u>Energy Dispersion</u>

The recording in Fig.25b shows that the separation of consecutive masses is imperfect and even that, in cases of simple ions, each spike is extended by a "tail" on the side of increasing masses. This is due to the fact that the contrast diaphragm of the emission lens limits only the "lateral energy" of secondary ions. The ions, leaving the target perpendicularly to its surface, pass through the contrast diaphragm, no matter what their energy might be. The selection slit of the spectrograph isolates an energy band of the order of about 10 ev. On measuring the secondary ion current at various excitations of the magnetic field near the value given by the maximum of a spike, the order of magnitude of the energy dispersion of the sputtered ions can be evaluated. For example, for lithium, the Li^{+7} ions with an energy of about 70 ev yie 1 a current 100 times lower, while ions with an energy of about 270 v will yield a current 1000 times lower. In the case of aluminum, the current is about 30 /39 times lower for ions having an energy of the order of 100 ev.

To understand the phenomenon of ion emission, it would be highly useful to know the energy distribution of secondary ions. Consequently, it is necessary to collect all ions emerging from the target and to analyze their energy. However, in our specific arrangement, the ions are partially stopped by the contrast diaphragm. Under the hypothesis that the emission takes place in accordance with a law of the same type as Lambert's law in optics, we were able to demonstrate that the attenuation coefficient introduced by the diaphragm is $\dfrac{\varphi_{0\blacksquare}}{\varphi_0}$; thus, it is possible to compare, for example, the low-energy intensities with those measured near 100 ev. However, the results of such a comparison have only an indicative value since the emission does not necessarily take

100

place in accordance with Lambert's law and since, in addition, the effect of discrimination introduced by the orifice O of the electrode A on the ions coming from the edge of the image field is disregarded. Thus, for a given initial energy $e\varphi_0 \le e\varphi_{0\pi}$, all ions emerging from the center of the field are able to pass through the orifice O no matter what their angle of exit α_0 might be, whereas this is not at all the case for ions emerging from the edge of the field.

Under these restrictions, let us use the values given above and let us then calculate, using the above values and assuming 1 ev for $e\varphi_{0\pi}$, the real intensities of ions whose initial energies fluctuate about a value of approximately 100 v. In the case of lithium, it will be found that the ions near 70 ev would have an intensity of the order of seven tenths those of the low-energy ions and that the ions near 270 ev would still have an intensity about three tenths of this value. As to aluminum, the ions near 100 ev would be three times more numerous than those constituting the spike Al^+.

These values are far from agreeing with those given by various authors. Thus, according to Stanton (Bibl.10), the Be^+ ions originating in a beryllium specimen bombarded by Ne^+ ions of 1000 ev energy are mostly emitted between 5 and 10 ev but certain ions have energies above 200 ev. Similarly, Honig (Bibl.12) found an energy distribution presenting a maximum at 2 ev and a half-width of 2.5 ev for the Ge^+ ions emitted by a germanium target under the impact of Kr^+ ions of 400 ev energy. Presumably, this is due to the fact that, in these experiments, the energies of primary particles were much lower than in our experiments. It should also be mentioned that the manner used in collecting the secondary ions on emission in these various setups is responsible for the fact that a portion of the fast secondary ions might be eliminated: no specific

101

indication is given whether this had been taken into account.

c. Emissivity of Various Elements

The first information available for a comparison of the emission of secondary ions of various elements is that obtained by measuring the intensity of M^+ ion current, under equal conditions of primary bombardment. Since the filter effect of the emission lens is the same for all ions of the M^+ type, the comparison of obtained values would, in all strictness, have to take account of the fact that each element has an initial energy distribution of secondary ions characteristic for it. Nevertheless, it seems likely that the differences in the energy distribution from one element to another are not sufficient to believe that a rough comparison of the obtained values might be absolutely wrong; in addition, if the luminosity of the images is the prime purpose of a given investigation, such a comparison will be entirely sufficient.

In classifying the elements by decreasing order of "emissivity", the following list is obtained: Al, Be, Li, Mg, Fe, Ti, Zn, Ni, Cu, Ag, etc. To give an order of magnitude, let us indicate that the intensity of the Al^+ ion current is 5×10^{-8} amp and that of the Cu^{+63} ions 8×10^{-11} amp, under equal conditions of primary bombardment.

The bombardment of other elements, such as carbon (graphite), silicon, or germanium, also excites the emission of characteristic ions. It should be mentioned that C_2^+ ions are obtained on graphite and that, on the other hand, silicon readily yields ions of the Si_2^+ and Si_3^+ type.

Besides determining the intensity of the secondary ion current it is of interest to define the yield of ions for each element, i.e., the ratio of the number n_i of secondary ions to the number n_0 of neutral atoms which must be

sputtered in order to produce this number of ions. The ratio n_i/n_0 enters the ultimate resolving power and also enters the theory of emission. Specifically, if the energy distribution of the ions could be compared with that of the neutral atoms and if the variation in the ratio n_i/n_0 with the initial energy of the particles could be defined, we would have - for each ejection velocity - the probability that one atom leaves the surface of the solid in the ionized state.

d. Measurement of the Ion Yield

Measuring the real value of the ratios n_i/n_0 is not possible with our set-up; in fact, the real value of the number n_i cannot be measured since the contrast diaphragm eliminates all ions whose "lateral energy" is higher than a certain value and since the selection slit permits passage of only those ions contained in a certain energy band. However, the number n_i measured by us is of interest since it is the number of ions that effectively contribute to formation of the image.

The measurements of the ratio $\left(\dfrac{n_i}{n_0}\right)_{exp}$ were made with a diaphragm that limits the lateral energy of the ions to 0.8 ev and with a selection slit that passes an energy band of about 12 ev.

The number n_0 of neutral atoms is measured by sputtering a known volume of matter. For example, it is possible to vacuum-deposit a pellet of a metal A on a solid base consisting of a metal B. The diameter of this pellet is taken less than the diameter of the field imaged by the emission lens, so that all ions /110 emerging from this pellet are collected (up to the ions eliminated by the dia-phragm and by the slit). Let ρ_A and M_A be the specific mass and the atomic mass of the element A, and let N be Avogadro's number; the pellet of volume V

103

contains $\dfrac{V_{CA}}{V_s} \cdot N$ atoms.

To measure the number n_i , the mass spectrograph is blocked on the line A^+ and the ion current is measured until complete disintegration of the pellet, which is indicated by an abrupt drop in the ion current. The amount of electricity received in the Faraday cylinder gives the number of total ions produced by the sputtering of a volume V of matter. This amount of electricity is simply measured from the area of the curve representing the intensity of the ion current as a function of time, obtained directly by means of the recorder.

We made measurements of $\left(\dfrac{n_i}{n_0}\right)_{exp}$ for two elements, copper and aluminum. The vacuum-deposited pellets were of a thickness of about 5 μ and a diameter of 0.5 mm. Under the above experimental conditions, we measured an ion yield of the order of 10^{-3} for aluminum; this yield dropped to about 5×10^{-7} for copper. The copper value concerns only the number n_i of Cu^{+63} ions but, from the practical viewpoint, this is the only datum of interest since the two isotopes Cu^{63} and Cu^{65} never contribute simultaneously to the formation of an image. Taking the isotope Cu^{65} (29.9%) into consideration, the Cu^+ ion current would be 1.1×10^{-10} amp.

According to these data, it is possible to calculate that there are three times more copper atoms than aluminum atoms extracted per unit time, while the Cu^+ ion current is 450 times weaker than that of Al^+ ions. From these measurements we can also deduce that the sputtering rate is 250 Å/sec for aluminum; under the same conditions of bombardment, copper will sputter at a rate of 570 Å/sec.

4. Alloys

In alloys, the phenomena are rather complex. Proportionality of the

104

secondary emission intensity to the concentration of an element is far from being a general rule. This proportionality can be approximately proved for the case of Ni-Cu alloys, and also is present for a Al-Cu alloy with 4% copper, when comparing the emission of the Cu^{+63} ion in pure copper and in the alloy. However, on passing to a Cu-Al alloy with 5% aluminum, the Cu^{+63} ion emission is about 10 times more intense than on pure copper while the Al^+ ion emission is only two times weaker than on pure aluminum.

It is not surprising that the Al^+ ion emission varies only from single to double when passing to the aluminum alloy. In fact, in a Cu-Al alloy with 5% aluminum, roughly one aluminum atom is present for every eight copper atoms. If we assume that the sputtering rate of the alloy is of the same order of magnitude as that of pure copper, there will be three times more atoms extracted from the alloy than there are atoms extracted from the pure aluminum during the same period of time. Since each ninth of the atoms leaving the alloy is an aluminum atom, there will be only three times less aluminum atoms extracted from the alloy per unit time than aluminum atoms extracted from an object made of pure aluminum. If the secondary ion yield is the same for pure aluminum as for the alloy, there would have to be an Al^+ ion current three times less intense in the alloy than in the aluminum. In view of the limits of the hypotheses established on the rate of sputtering, on the magnitude of secondary ion yield, and on the accuracy of measurement, the estimate made is acceptable. Conversely, an increase in the Cu^+ ion emission is much more difficult to understand if the mechanism of secondary ion emission is not accurately known.

This phenomenon is not unique and occurs also in Cu-Be alloys with 2% beryllium (one beryllium atom for each seven copper atoms) where the Cu^{+63} ion emission is 60 times more intense than in pure copper.

105

Let us also mention that the ratio of the Al_2^+ ion current intensity to

that of the Al^+ ion current is 8×10^{-3} for pure aluminum and 6×10^{-3} for the

Cu-Al alloy. This fact is singular since it seems to suggest the idea that the

aluminum atoms are grouped within the alloy. However, it is generally admitted

that, up to a concentration of about 8%, aluminum is completely miscible in

copper. So as to eliminate, as far as possible, the hypothesis of aluminum

atom groupings within the alloy, two different specimens were subjected to dif-

ferent thermal treatments. The specimens were heated to $500^\circ C$ for 12 hrs, after

which one was cooled slowly and the other quenched.

In addition, in the hypothesis of a perfect solution of aluminum in copper,

it must be admitted that the grouping of two aluminum atoms within the Al_2^+ ion

cannot be due to their close neighborhood within the crystal lattice but must

be due to a later association of two Al^+ ions or of one Al^+ ion with one neutral

atom. This makes it difficult to understand that one or the other of these

processes would not be sensitive to the density of aluminum atoms existing in

the lattice and that the ratio Al_2^+/Al^+ would not be affected by this to a

greater extent.

It is possible to formulate still another hypothesis for explaining this /41

phenomenon: The sputtered material rebounds from the electrode A and is de-

posited on the target. This leads to a continuous formation of a layer which

will be much richer in aluminum than the alloy in question. As soon as formed,

this layer is destroyed by the primary bombardment, yielding Al^+ and Al_2^+ ions.

If this origin of aluminum ions is considered correct, it can be understood

that the ratio Al_2^+/Al^+ undergoes only a minor change, but it could not be under-

stood why the Al^+ ion emission should be that strong. In fact, referring to the

micrograph in Fig.26, the bars of the screen are black; this means that the

aluminum deposit on the copper bars does not give an emission comparable to that of the pure metal.

To corroborate this finding for the case of the alloy, we investigated the images of the alloy surface, formed by Al_2^+ and Al^+ ions. The objects were prepared as follows: A screen of 25 μ mesh is plated to the polished face of a pellet of the alloy in question; copper is then vapor-deposited through this screen. On removing the screen, small squares of copper are left on the surface which align themselves into a screen of 25 μ mesh. On forming the Al^+ and Al_2^+ images of such an object, two identical images will be observed; the squares appear completely dark whereas tne alloy surface not covered by copper appears light and traces a screen with light bars of 25 μ spacing. From this it can be concluded that the Al_2^+ ion emission can definitely not be due to a "redeposition" of aluminum on the target.

Let us note that the image formed by the Cu^{+63} ions shows a screen whose bars are lighter than the squares separating them which, nevertheless, are formed of pure copper; this yields a direct image of the enhancement of the emission of copper over the alloy.

For an alloy with 1% aluminum, we also found a higher copper emission of the image, but this enhancement was less than before. In addition, the Al_2^+ ions still give an image despite the fact that there is not more than one aluminum atom present for each 40 copper atoms; for the case of complete miscibility of aluminum and copper, this is difficult to understand. Naturally, it would be necessary to study these phenomena on a much more extensive range of alloys.

In conclusion, it might be stated that the laws which correlate the ion intensities with the composition are far from simple, at least wherever it is not a question of neighboring elements or of isotopes; as long as such laws

will not have been derived in a rigorous form, an empirical calibration will be necessary. Therefore, it is difficult at present to make definite statements on the exact possibilities of a quantitative analysis; the situation is somewhat similar to that obtained in light spectrography where the use of an empirical standardization by means of control alloys, having a composition close to that of the experimental alloy, is practically indispensable.

5. Composite Materials

Up to now, we investigated only a few compounds, mainly alkali metal halides and oxides.

Alkali metal halides give an intense emission of the metallic ion. Thus, the chlorides of sodium and potassium and the fluoride of lithium emit, respectively, Na^+, K^+, and Li^+ ions; for example, the Na^+ ion current is of the order of microamperes. An emission of Cl^- and F^- ions also takes place.

In iron oxides and copper oxides we observed the emission of O^+ and O_2^+ ions. In addition, the emission of the metallic ion is more intense in the oxide than in the pure metal. Thus, the Cu^{+63} ion current is about 10 times more intense in the CuO oxide than in pure copper. Since this is probably due to the "ion character" of the bond in the oxides, it must be expected that an emission of O^- ions takes place; actually, this has been found to be the case. We should also mention the existence of molecular ions of the type $(MO)^+$, formed by the association of an oxygen atom and an atom M of the oxidized metal.

Let us mention also that a specimen of aluminum, containing nitrides, will yield N_2^+ ions.

The statements made above on the subject of alloys as to the possibilities of a quantitative analysis apply even more to this particular case. This

should suggest a certain caution in the interpretation of the images. Nevertheless, the dependence of the ion emission on the chemical bonds might, in some cases, yield data on the structure of a given compound.

6. Identification of Elements

The filtering produced by the magnetic field extends only to the specific charge of the ion, i.e., to the charge-mass ratio. Ions of differing nature but having the same specific charge will pass together through the selection slit and will yield superposed distribution images. This raises the question as to the possibility of some confusion resulting from this.

Considering only the simple ions corresponding to all isotopes of the elements in the Periodic Table, the apparatus will give about 200 different "answers"; because of the fact that each ion is characterized only by its mass, this information is insufficient for identifying. without risk of error, all ions that a given alloy is able to emit.

In fact, different elements may have isotopes of the same mass. For example, in the case of nickel or of iron, the mass 58 can be produced either by the Ni^{+58} ions or by the Fe^{+58} ions. However, if Ni^+ ions are involved, /42 an identical image must be obtained with the mass 60 since its intensity is reduced merely by a factor of about 2.5 (naturally, this means that no isotope separation takes place within the specimen). If iron is involved, the image made by ions of mass 60 will not appear. The indeterminacy , in most of the cases, could thus be resolved by a control relative to the isotopes.

However, the main difficulties are produced by the presence of molecular ions and of multiply charged ions. The molecular ions introduce a series of masses which are superposed to those of the simple ions; multiply charged ions,

depending on the cases involved, may yield already existing masses or "fractional masses". For example, magnesium gives rise to the mass series 12, 12.5, 13 (doubly charged ions), 24, 25, 26 (simple ions), 48, 49, 50, 51, 52 (molecular ions formed of two atoms). Thus, the research on carbon in the presence of magnesium will be especially difficult since carbon gives the mass series 12, 13 (simple ions) and 24, 25, 26 (molecular ions formed of two atoms). However, even in such an unfavorable case it will always be possible to compare the masses 12.5 and 48 so as to confirm the distribution of magnesium which, for the two masses, should present identical images. If the magnesium and carbon are not associated, a comparison of the distribution image of magnesium with one of the images in which the distributions of magnesium and carbon are superposed will make it possible to define the distribution of the carbon. If the carbon and magnesium are associated, other factors may be in question for facilitating the investigation, such as the presence of molecular ions which reflect the nature of this association, or the increase or decrease in the emission of one or the other of the two elements depending on the character of the bond. Finally, if the carbon and magnesium are uniformly distributed one in the other, the distribution images will show a "flat shading". As a final measure, it is also possible to verify the intensity ratios between the masses 12, 12.5, and 13 or between the masses 24, 25, and 26 corresponding to the isotope abundance ratios of magnesium, and thus possibly re-establish the connection by deduction, which would return again to carbon. This entirely theoretical example shows the difficulty encountered by the analysis in certain cases which are, of course, more or less unfavorable. Speaking generally, the existence of molecular ions and multiply charged ions will introduce a certain complexity into the analysis, a complexity which has obvious drawbacks but which

also may yield valuable data. No matter what the case may be, the presence of isotopes, far from constituting a disadvantage, seems a highly beneficial phenomenon because of the fact that it permits a considerable increase in the number of distinct "answers" obtainable from the instrument used.

7. Negative Ions

The number of responses furnished by the instrument can be further increased by forming distribution images with the negative ions emitted by the target. The fact that, until now, we have used only positive ions is basically due to the finding that the characteristic emission of metals takes place in accordance with this mode. However, the alkali metal halides and the metal oxides have shown already that the emission of negative ions may also be characteristic for the constituents of the object. The results obtained by various authors (Bibl.15, 29, 31, 32, 33) indicate that numerous "parasite peaks" must be expected. Specifically, the images of wires and screens obtained by Bernard and Goutte (Bibl.29) seemed to indicate that these spikes are due to organic vapors absorbed at the surface of the target and to surface reactions with the residual gas in the vacuum enclosure.

Otherwise, from the optical viewpoint, the use of negative ions for forming the image of the surface presents some difficulties, which are due to the fact that the conversion of the optical image into an electron image does not proceed under the same advantages as in the case of positive ions. In fact, the converter cathode is of necessity negatively polarized so as to repel the secondary ions produced by the impact of ions, which means that positive ions are attracted by this cathode whereas negative ions are repelled. The negative ions will reach the cathode only if their energy is sufficient, which shows the

necessity of strong postacceleration after their passage through the prism. In addition, the image formed by these ions on the cathode is dilated instead of being contracted, as had been the case for positive ions. This means that the pincushion distortion of the lens system in front of the converter and that given by the converter itself on the electron image, are no longer compensated by the barrel distortion of the ion image produced by the contraction; quite the contrary, a pincushion distortion produced by the dilatation of the image is added to this.

a. Experimental Setup

To change from a "positive" setup to a "negative" setup, it is necessary - on the side of the "object part" - to reverse the polarities applied to the target and to the central electrode of the emission lens as well as to reverse the sense of the magnetic field. Since the positive primary ions are attracted by the target, no illumination difficulty exists. The object merely is moved away from the electrode A until the beam reaches the center of the imaged field. The distance Δ thus increases, leading to a weakening of the extracting field and to an increase in distance between virtual image and crossover. By adjusting the excitation of the emission lens, focusing will still be possible but the real crossover C, namely, the image of the virtual crossover C_0, no longer will be exactly at the level of the contrast diaphragm; this affects the filtering /43 by the diaphragm, although this filtering still remains sufficiently within the limits of our goal which is to obtain several images giving a general view over the possibilities of analysis offered by the use of negative ions. Let us mention also that the object is brought to a potential of -5 kv which causes the primary ions to arrive at the target with an energy of 15 Kev, i.e., slightly

112

more than double the potential they have when the target is positively polarized.

On the side of the "image part", the tube H, which fixes the potential of postacceleration for accelerating the negative ions, must be positively polarized. The difference in potential between the converter cathode and the tube H will give the energy of the electrons that form the final image. We have indicated above that it is important to have this energy be of the order of several tens of kiloelectron-volts. However, if it is desired that the negative ions reach the cathode, the potential of the latter must not be below the "take-off" potential of the ions. It even is necessary that the potential of the cathode be positive so that the ions will arrive at this cathode with a sufficient energy and that the image will not suffer too strong a dilatation. From all this it follows that the potential to which the tube H is brought must be, in absolute value, much greater than in the case of postacceleration of positive ions. Since the apparatus had been designed only for the utilization of positive ions, the insulation of the tube H is insufficient. In addition, we had available only a rectified positive high voltage, filtered but not stabilized. Under these conditions we were able to make only a few tests with the tube H polarized at 19 kv and the converter cathode polarized at 2 - 3 kv. Thus, the negative ions arrive at the cathode driven at 7 - 8 Kev, while the electrons are accelerated at a potential difference of 17 - 16 kv. The central electrode of the projection lens is polarized between -4 and -5 kv.

b. Focusing of the Ion Image

The focusing is done in the same manner as for the positive ions: The achromatic plane is defined by varying the excitation of the projection lens and the focusing of the emission lens. The setting is further refined by slightly

varying the magnetic field until an image insensitive to this variation is obtained. Finally, the focusing of the converter and the correction of astigmatism are played in.

The investigated object is a copper screen of 25 μ mesh, pressed into an aluminum block which is slightly pre-oxidized. The image is observed by means of O^{-16} ions. After the natural oxide film on the copper is removed, the screen will appear dark on a light background, due to the emission of O^{-16} ions by the aluminum. This makes it possible to measure the final magnification and to follow the course of the distortion. We found that the pincushion distortion is so low as not to interfere to any noticeable extent.

c. Results

We investigated iron, copper, and aluminum oxides and verified that they all emit O^{-16} ions. The micrograph in Fig.a (Plate III) was obtained with O^{-16} ions on a copper specimen, containing small islets of Cu_2O oxide. The image is lacking in contrast since the copper matrix contains oxide pits and also since an emission of ions of mass 16 takes place which apparently uniformly coat all investigated specimens. We made no specific studies for determining the exact origin of this emission. It is well possible that it is produced by a deposition of the gaseous phase on the object surface, a coating which is constantly being destroyed by the bombardment, yielding ions of the O^-, $(CH_4)^-$, or $(NH_2)^-$ type; the emission may also be due to a surface oxidation by the oxygen contained in the residual gas. By letting the vacuum degrade on the object side, we found that the extent of this emission increases, which seems to indicate that a vacuum of 10^{-8} mm Hg is possibly not sufficient for surface investigations with negative ions.

If the object consists of an ionic compound, it must be expected, as demon-strated above, that an intense emission of negative ions takes place. For ex-ample, let us deposit, on the polished face of a stainless steel pellet, a drop of sodium chloride solution. After evaporating the solvent, a deposit of salt will remain; this deposit must be sufficiently diluted so that the electric charges can be dissipated since sodium chloride is an insulator. The micro-graph in Fig.b (Plate III) shows the image obtained with Cl^{-35} ions on such an object. Similar images are obtained with Br^- and F^- ions on potassium bromide and on lithium fluoride. These images are very luminous so that the exposure time for photographing them from outside is of the order of only 1 - 2 sec. In addition, since the deposit is quite thin, the progress of sputtering can be followed on the progressive disappearance of the image.

These few experiments show that it is possible to obtain distribution images with negative ions, without changing the optics of the apparatus. This may be of interest for analyzing certain constituents which readily yield nega-tive ions. However, a slightly more detailed study will be necessary for accu-rately defining the portion of the emission which is to be attributed to char-acteristic ions and, so far as possible, to obtain conditions under which the emission of "parasite spikes" is suppressed or at least very much attenuated. In addition, the observation of images obtained from insulators creates an in-centive for a more detailed study of this important problem.

^. Insulators

A study of insulating materials encounters two types of difficulties: The surface of a given insulator is not necessarily equipotential so that the elec-tric charges cannot be dissipated. This results in the fact that the potential

of secondary ion emission is not well defined and will vary with time, which
will result in a disappearance of the image; in addition, the accumulation of charges will result in breakdowns.

By suitably arranging conductors with fixed potential in the vicinity of the insulator, it is possible to render the surface from which the secondary ions are emitted equipotential. For example, by giving the insulating material the shape of a foil with parallel faces and by placing this foil on one of the armatures of a plane capacitor, the faces of this foil will coincide with a plane equipotential surface. Consequently, if an insulating foil is plated to the plane face of the electrode M, the face of the insulator parallel to the electrode A will be equipotential. Let a be the thickness of the foil, ε its relative dielectric constant, and Δ the distance of the free surface of the in-sulator from the electrode A, with M being brought to a potential V, so that the leaving potential of the secondary ions will be $\frac{V}{1 + \frac{c}{\varepsilon \Delta}}$. However, in such an arrangement, dissipation of the charges is not fully ensured and the arrival as well as the departure of charged particles will balance only by chance, which means that the indicated distribution of the potential will be perturbed by the presence of static charges.

Depending on the polarization of the object, the retained charges will be either positive or negative. If the object is positively polarized, it will attract the secondary electrons produced mainly on the electrode A by the impact of secondary ions and of primary ions diffused by the target. Some of the primary ions may enter the crystal lattice of the insulator and, since their penetration is quite shallow, will form a practically superficial layer. In this case, an equilibrium state must be expected in which, as the sputtering progresses, a layer of positive charges is continuously destroyed and reconsti-

tuted. If the object is negatively polarized, it will retain the positive

charges, which means that the positive ions of the bombardment will accumulate;

in addition, since the negative ions and the secondary electrons are repelled,

the positive charge of the object will only increase at the point where the

primary beam strikes. Consequently, it can be predicted that a migration of

the ion charges will take place, accompanied by a variation in the leaving

potential and by breakdowns.

No matter whether positive or negative secondary ions are involved, it

seems obvious that the static charges accumulating on the object make an obser-

vation of the image rather difficult. To keep the distribution of the potential

from being influenced by the presence of these charges, it is necessary to ob-

tain either their neutralization or their dissipation.

a. Preparation of the Object

It is difficult to apply here the method used in electron-probe micro-

analyzers, which consists in depositing a continuous metal layer on the insu-

lator. In fact, the negligible penetration depth of the ions into the material

would prevent the primary ions from reaching the target and, a fortiori, the

secondary ions from leaving the target. Consequently, the deposited layer must

have gaps which leave some areas of the insulator free of coating, which then

are exactly the regions which will be imaged. However, these gaps must have

sufficiently small dimensions to have the potential vary only little from one

point to the other on the insulating surface not covered by the metal layer.

In addition, the metal coating deposited on the plane and polished surface of

the insulator must be provided with identical gaps, so that the observation of

each individual islet can proceed under equal conditions. Thus, the simplest

117

way is to deposit a metal screen, formed of crossed continuous wires or simply of parallel wires. To ensure as satisfactory an electric contact as possible, the insulator is enclosed in a pellet of Wood's alloy; one of the faces of the pellet is in the same plane as the polished surface of the insulator to be investigated. The next step is to vacuum-deposit an aluminum layer of a thickness of several microns over the entire surface of the specimen, using a mask to keep a region of 8 mm diameter on the insulating surface free of coating. The screen is obtained by vacuum-depositing aluminum through a mask formed of parallel wires. To obtain a screen of crossed wires it is sufficient to apply two successive coatings, with the direction of the wires in the second vaporization being at 90° to the first vaporization. By changing the diameter of the wires and their spacing, the width of the bars and the mesh of the aluminum screen deposited on the insulator can be varied. In general, we used screens of 0.08 mm mesh, 0.03 mm width of the bars, and several microns thickness. The aluminum wires are sufficiently extended to come into contact with the preceding vapor deposition, so that each wire is directly connected to the conducting support. Aluminum was selected because of its low sputtering rate. In addition, to avoid any break in electric contact, the region in which the insulator is linked to the metal support is coated with a conducting silvering before vaporization. The pellet prepared in this manner is then covered with a copper sheet of 9 μ thickness, pierced by a hole of 3 mm diameter; the entire unit is placed into an object support identical to those used for conducting specimens. The role played by the copper sheet is mainly that of partially eliminating the secondary electrons coming from the electrode A. Let us mention that, for limiting the bombarded area and for decreasing the magnitude of secondary phenomena, including the emission of secondary electrons, a diaphragm of 0.5 mm diameter is placed at

118

the exit of the channel Ca by which the primary ion beam arrives. This does result in a decrease in the density of ions arriving at the target, but this density is still sufficient to give images of adequate luminosity.

b. Observation of the Images

The images observed by us were formed by positive ions. As long as the wires of the screen are not destroyed by the sputtering, the image remains stable, the breakdowns are rather infrequent, and all adjustments that can be /45 made with conducting objects (adjustment of achromatism and stigmatism) can be also made with insulating objects. The micrograph (Fig.d, Plate III), taken with Mg^{+24} ions on a calcareous specimen, indicates already that the quality of the images is not too greatly affected by the treatment to which the object had been subjected (the black bands correspond to the aluminum bars vapor-deposited on the object, with the screen being formed here by parallel wires).

The fact that an image of the insulating surface is obtained and that this image is more or less normally illuminated indicates that the leaving potential of the secondary ions is practically the same at any point of the observed field. Nevertheless, there is a possibility that a potential difference exists between insulator and conducting screen. To define this, the Al^+ ions can be used for successively forming the image of the screen and the image of the free surfaces of the underlying insulator (naturally, provided that the latter con- tains aluminum). If these two images are obtained without changing the setting of the magnetic spectrograph, it would mean that the leaving potential of the ions is practically the same on both metal and insulator. Conversely, if the magnitude of the magnetic induction must be either decreased or increased in order to "recover" the image of the insulator, it is obvious that its potential

is either weaker or stronger than that of the screen. Working in this manner, we found that the leaving potential of the ions on the insulator could be higher by several tens of volts. This seems to indicate that the charge remaining on the object is positive. However, it could also be imagined that the maximum of energy distribution of the ion emission by the insulator is shifted toward high energies. Let us mention that, for explaining the observed pattern, this maximum would have to be extremely high since the contrast diaphragm eliminates many
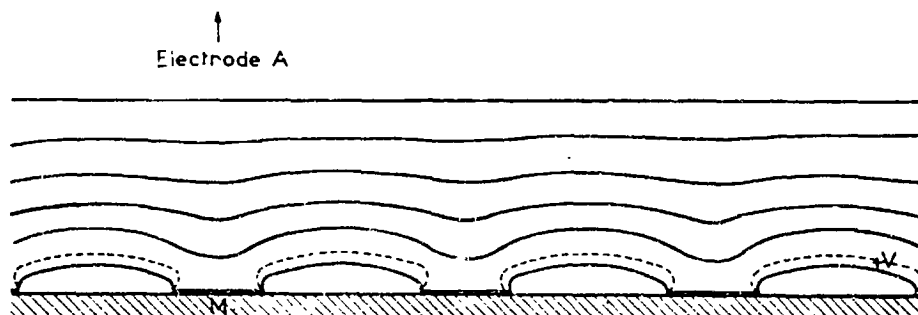

Electrode A

Fig.26

of the fast ions. In addition, even after some of the bars of the screen have disintegrated, an image whose field is crossed by a light-colored band can still be observed for a certain time. On displacing the object, it will be found that this band is "linked" to it; in addition, on modifying the excitation of the spectrograph this band will shift. All this seems to indicate that this particular pattern might be due to the fact that the potential is no longer sufficiently uniform over the observed region; to each excitation of the spectrograph there corresponds a certain energy band. This tends to indicate that it is much more likely that the line shift is produced by charges remaining on the object rather than by a displacement of the emission maximum. To corroborate this finding, it would be of interest to bombard the target with neutral particles or even with

120

negative ions. Let us mention finally that the line shift is slight. Thus, on the image (Fig.c, Plate VI) taken with Al⁺ ions and a granite specimen, at a given value of magnetic induction, it is possible to see simultaneously the image of the screen and the image of aluminum distribution in the insulator. By slightly reducing the magnetic induction to below this value, the image of the screen will become somewhat more luminous while the image of the aluminum distribution will be stumped; the opposite pattern is observed by slightly increasing the induction. This minor line shift generally does not increase the difficulty of identifying the elements.

From these experiments, it can be concluded that the potential of the object is automatically fixed to a constant value which is almost uniform over the entire imaged surface of the insulator. However, the insulating object retains positive charges so that a portion of these charges is necessarily neutralized by the arrival of electrons. Since it has been found that the image can no longer be observed if the screen is disintegrated by the primary bombardment of the surface of the imaged field, these electrons presumably originate in the screen from which they are extracted by the impact of primary ions. The question to be solved is that of the manner in which these electrons, repelled by the field E_0 which accelerates the positive secondary ions, are able to reach the insulating zones. For this, let us consider the distribution of equipotential surfaces between the electrode A and the object M: This distribution affects the form sketched in Fig.26 where the black rectangles represent the intersection of the wires of the screen by the plane of the figure. The positive charges present on the insulator "repel" for example the equipotential + V which, because of this fact, presents a prominence or hump each time it comes to lie above an insulating region. On an increase in the charge carried by the

insulator, the hump of the equipotential expands into a "bulge" (shown as a broken line in Fig.26) which runs along the top of the screen bars. The region located at the interior of such a bulge is at a potential higher than that of the screen bars, so that secondary electrons are emitted by the bars which are drained toward the insulating regions. This indicates that a state of equilibrium may be established at which the positive charges are partly neutralized, so that the potential remains approximately constant. In addition, since the electrons are more attracted by regions which have accumulated slightly more positive charges, the potential of the insulating surface will be almost uniform.

Making use of this method of preparation, we investigated objects composed of various specimens of natural rock: a limestone, a granite, and a complex phosphate known as amblygonite. A detailed examination of the micrographs with these various specimens will be the subject of the next Chapter.

Let us note that our method definitely can be extended to an investigation of insulators by means of negative ions. We mentioned in the preceding Section that we had obtained images with Cl^- ions on an object of sodium chloride. The preparation of the object in this case is somewhat similar to that discussed below. In fact, it can be stated that the conductor used as support for the thinly deposited salt plays the same role as the aluminum screen. However, this role is somewhat less significant in the case of a screen since it is impossible to expect the same regularity in the distribution of conducting surfaces. Thus, as soon as the conglomerates of insulators become of too widely differing size, the charge of the individual conglomerates no longer is close and the leaving potentials will change; it never happens that all the islets can be illuminated together at one and the same adjustment of the spectrograph.

CHAPTER IV

FIELD OF APPLICATION

The main drawback of this method of analysis is the difficulty of quantita-
tive interpretation of the results. However, in many cases, this drawback
probably is of a temporary nature, since it is chiefly due to a lack of data on
the phenomenon of secondary emission of characteristic ions. The setup developed
by us offers a means of investigation which is particularly sensitive and effi-
cient since it permits to "see" directly what might happen on the surface of the
bombarded object. Consequently, the instrument can be used for two complement-
ary purposes of which the first, combined with a measurement of the ion currents,
concerns the study of the emission itself while the second exploits the existing
possibilities of semiquantitative analysis.

1. Contribution to the Study of Secondary Ion Emission

a. Identification of the Ions

The distribution images frequently offer a valuable aid for studying the
emission of secondary ions. Particularly, the research on the identity of the
ions which is often rendered quite complex by the presence of molecular ions,
by multiply charged ions, or by diffused primary atoms, is facilitated by ob-
serving the corresponding images of the object surface. To give an example,
recordings of the secondary ion current frequently show a spike for the mass
40, whose slope on the side of higher masses is quite peculiar and not always
reproducible. Since the specimen is bombarded by argon ions, the course of the
recording was attributed to the diffusion of these ions. The observed images
with ions of mass 40 show brilliant points against a much paler background,

123

which gives a highly complex aspect to the diffusion of argon ions. Later, we found that the appearance of these brilliant points depends on the preparation of the specimen and that they will disappear when electrolytically polished objects are used. It is quite likely that the origin of these points lies in the emission of $(Si - C)^+$ ions, produced by carborundum particles included in the object during polishing. A check test with respect to the isotopes is rather difficult here since the isotopes 29 and 30 of silicon are present only in low concentration and since the images are swamped in the continuous background of the diffusion of argon (this could be remedied by bombarding with ions of another rare gas).

b. Elements in Low Concentration

A low-concentration element in a given specimen may produce a more or less intense emission of secondary ions, depending on whether this element is dissolved in the object or conglomerated in precipitates (for example, effect of the cupro-aluminum matrix). Since the distribution image gives the local concentration of the element, it is easy to differentiate one case from the other, naturally within the resolving power of the apparatus. In addition, if the element is conglomerated in precipitates, the concentration of emission in a few points rather facilitates its investigation although the overall intensity of /47 the ion current may be low. Let us imagine that the overall emission over an area of 0.5 mm diameter, of an element in the solid state is 10^{-10} amp and that a precipitate of 5μ diameter, immersed in another element, will emit a total current of 10^{-14} amp. Despite the fact that it is easy to measure, this current may be overlooked in compiling the list of emitted ions. Similarly, a control with respect to the isotopes is quite easy since, on passing from one isotope

to the other, the image remains the same.

If an element of low concentration enters an ionic combination, its emission is enhanced and its investigation is correspondingly facilitated. Thus, in a casting containing 0.5% of manganese, we observed several precipitates of manganese sulfide. In addition, an image formed with negative S^{-32} ions is observed.

c. Influence of the Chemical Bond

Generally speaking, the presence of a given element in a chemical bond is visually displayed on the image obtained with the characteristic ions of this element. Obviously, the measuring of the secondary ion current is insufficient since it only permits defining the variations in intensity from one islet to the other or from one specimen to the other, without the possibility of detecting the accurate cause. A striking example is that of a solid copper object containing nodules of copper oxide Cu_2O whose image is given on the micrograph of Fig.c (Plate III), taken with Cu^{+63} ions. The regions where the copper has entered into chemical combination with the oxygen show up as light spots despite the fact that the concentration of copper is quite low there; in addition, small specks of oxide appear in the copper matrix. We would like to mention that the images obtained with O^+ and O^- would be of great assistance in identifying the oxidized regions in cases that are less complex than that given here. We encountered a similar case with an iron specimen which showed a few islets of oxide.

2. Semiquantitative Analysis

a. Metallic Alloys

The micrographs in Plate IV, obtained with an Al-Mg-Si crude foundry alloy

give a general view over the possibilities of semiquantitative analysis. These micrographs correspond to the distribution of magnesium, aluminum, and silicon. The image of silicon clearly shows the presence of a small plate of pure silicon and polygonal precipitates of a phase less rich in silicon. The magnesium image shows a difference of intensity in the "blacks"; the placement of the silicon platelet conceals no visible trace of magnesium whereas the aluminum matrix seems to contain a small amount of it. Unfortunately, these differences which can be seen with the naked eye cannot be photographed from outside because of the excessively long exposure times that would be needed. Let us mention incidentally that the magnesium, aluminum, and silicon images are obtained with exposure times of 2, 0.5, and 10 sec, respectively. Since a small part(about 1‰) of the light emitted by the fluorescent screen is used for producing an image on the film, it is logical that a substantial gain in sensitivity could be obtained by directly reproducing the electron image on a photographic plate. This would make it possible to distinguish minor variations in intensity or else to reduce the exposure time or the sputtering rate.

A comparison of images of this type with those obtained by scanning with an electron-probe microanalyzer proves that the local variations in concentration of the various elements are quite faithfully represented by the variations in local illumination of the image; in fact, neighbored elements are involved here for which the intensity of secondary ion emission varies roughly as the concentration of the elements. Naturally, numerous cases exist in which the fact that the emission is not proportional to the concentration will interfere considerably. Nevertheless, a distribution image indicates the local presence of a given element and, in this sense, always will have the value of a qualitative microanalysis. On the other hand, since the emission of this element is

126

influenced only by the presence of other elements, a comparison of the images obtained for the various constituents will yield useful data on the combinations of which they form part. Such a study also is worth being simultaneously conducted by both ion microanalysis and X-ray microanalysis.

b. <u>Light Elements</u>

One of the advantages of our method of analysis is the fact that it is equally suitable for light elements such as lithium, beryllium, boron, carbon, nitrogen, oxygen, etc. for which the electron-probe microanalyzer is quite difficult to use or may even be completely useless. To give an example of the analysis of oxygen, we could mention the case of a specimen containing copper oxide nodules where the image formed by the O^{-16} ions (Fig.a, Plate III) represents the oxygen distribution. One can also expect further improvements in the image recording device which would permit obtaining a micrograph with O^{+16} ions. It is highly probable that the emission of oxygen ions by various oxides of a metal will differ so that it would become possible to distinguish one type of oxide from another. No matter how this might be, a comparison of the images given by metallic ions and by oxygen ions already permits an identification of the presence of oxides without difficulty.

Without making a systematic study of a particular case, we investigated other specimens. The micrographs given in Plate V (Fig.c, a, b) show, respectively, an image obtained with B^{+11} ions and two images produced with Fe^{+56} ions in an iron specimen of crude casting, containing 0.2% of boron and 0.5% of /48 carbon.

The image in Fig.a (Plate V) was taken with an exposure time three times longer than that used for the image in Fig.b (Plate V) (4 sec exposure) to

demonstrate the intensification of the emission of iron. This enhancement coincides with the distribution image of boron, which seems to indicate that iron and boron enter in the same chemical combination. In addition, on changing to negative ions, analogous lattices can be seen on the images formed by C^{-12} and C^{-24} ions; consequently, the three elements boron, carbon, and iron are associated, probably involving an iron borocarbide.

We can also mention images observed on a casting with C^+ and C^- ions, which permit a localization of graphite filaments. The images formed by the C^- and C_2^- ions are more luminous than their homologs in positive ions but, under the slightly precarious conditions of work, it is rather difficult to photograph these from outside the equipment. The emission of carbon on graphite also does not authorize us to state that the presence of carbon is always detectable. Thus, we were unable to observe an image of pearlitic precipitates which this casting contained. In this particular case, if it is not a question of luminosity, it is possible that this phenomenon is due to the character of the bond in the cementite. The emission of carbon compounds poses a problem which it would be interesting to solve. We also observed an image formed by N_2^+ ions on an aluminum specimen containing nitrides of polygonal forms.

The light elements are frequently encountered among the constituents of natural rocks; in the following Section we will give a few application examples.

c. Insulators

The possibility of observing images on insulators permits an extension of the method of analysis by secondary ion emission to all solids. Among insulating materials, natural rocks because of the variety of elements they enclose, are the specimens of choice, disregarding even the intrinsic interest that their

investigation might offer. Three types of object: were examined: a limestone, a granite, and an amblygonite.

The first of these is composed of calcium carbonate containing various inclusions, among others a hydrated magnesium silicate (talc). Since the bonds in these compounds rather have an ion character, the emission of various ions is quite interse. We have observed and photographed images giving the distribution of calcium, silicon, aluminum, magnesium, etc. Other images are visible (some of these even very intense) which correspond to the rather numerous impurities in this type of specimen. Occasionally, the inclusions of talc surround the grains of calcite and, since the presence of such inclusions involves a lack of calcium on the image made with Ca^+ ions, the polygonal intersection of the rhombohedrons of calcite by the plane of the surface shows light on a dark background. Conversely, on the images of silicon and magnesium, for example, these grains show up dark.

With respect to the granite object, let us recall that this rock is basically composed of three constituents: quartz, feldspath, and mica. The quartz is the crystallized form of the silicon oxide SiO_2; the feldspath and the mica are two complex aluminosilicates. In the investigated specimen, the mica is a lithiniferous compound known under the name of lepidolite; what distinguishes here the two types of aluminosilicate from the point of view of the chemical composition is the presence of lithium in the mica. The micrographs (Fig.a, b, c, d, e, f, Plates VI and VII) give, respectively, the distribution of lithium, sodium, aluminum, silicon, potassium, and calcium. A comparison of Figs.c and d formed, respectively, by the Al^{+27} and Si^{+28} ions, shows that the light islet in Fig.d appears black in Fig.c; consequently, this spot consists of quartz whereas the darker part belongs to an aluminosilicate. Figure a, formed with

129

Li^{+7} ions, indicates that a mica is involved here. The cations of the alumino-
silicate are lithium, sodium, and potassium but it can be seen that both sodium
and lithium have a tendency to be mutually exclusive. The black and parallel
lines which appear on the first five photos are occupied by a calcium compound
as shown in the last micrograph; probably a carbonate is involved here. On the
aluminum image, the presence of the vaporized screen is clearly seen, which
appears in black on the other images (since several wires of the screen, used as
mask during the vaporization, had accidentally conglomerated, the vaporized
screen shows a slightly larger mesh at some spots than had been indicated in
Chapter III). Finally, in other regions of this same specimen, islets of feld-
spath and of mica could be differentiated by means of the lithium distribution
image.

Quite a number of other images can be observed on this specimen, produced
by low-concentration elements, molecular ions, or possibly by elements that
yield only few positive ions. Thus, an image made by O^{+16} ions can be observed,
indicating that these ions are emitted with a greater intensity on quartz than
on aluminosilicates.

The last specimen investigated consisted of amblygonite which is a complex
phosphate in which lithium, sodium, and aluminum oxides are associated. The
images given by the Li^{+7}, Na^{+23}, and Al^{+27} are very luminous. The regions where
lithium and sodium are present are clearly defined. In addition, metallic im-
purities such as copper are clearly visible.

3. Other Applications   /149

The ion source which is constituted by the unit of the emission objective,
suggests other applications which will not always require the use of distribu-

tion images.

a. Analysis of Surface Layers

If no precise localization in the plane of the surface is required, the ionic scouring of a few atomic layers will yield a secondary ion current of sufficient intensity to be measured easily. In fact, consider the highly unfavorable case of a body whose ion yield is of the order of 10^{-7}. In itself, the measurement of a current of the order of 10^{-14} amp presents no particular difficulty. However, this current transports 6.25×10^4 ions per second; for producing such a current it is necessary to sputter 6.25×10^{11} particles per second. Since the mean density of a solid is of the order of 10^{11} particles per μ^3, it is necessary to sputter a volume of matter of about $6 \, \mu^3$ to produce a current of 10^{-14} amp. On an area of 0.2 mm diameter, this volume represents a layer of matter of about 20 Å thickness. The resolving power "in depth" thus is infinitely superior to that of the electron-probe microanalyzer. For example, we were able to detect the 0^+ spike produced by the natural oxide layer on a magnesium specimen (whose thickness is several tens of angstroms) and follow its progressive disappearance as increasingly deeper layers were analyzed.

b. Isotope Analysis

The simultaneous measuring of ion currents, corresponding to two isotopes of one and the same element, yields the isotope abundance ratio of this element in the sputtered volume. If the mutual diffusion of two isotopes is to be studied (or the diffusion of an isotope in the natural element) it is, for example, possible to make use of ionic scouring for observing the variation in the isotope ratio as increasingly deeper layers are being analyzed. It is also

possible to make a cut parallel to the direction of diffusion and view the image of the region where the diffusion is produce'; a photometric plot would then permit to obtain the diffusion curve. It even is possible to use the distribution images for detecting "isotope segregations" within the natural specimens which, during their history, had been subjected to high thermal gradients. Speaking generally, in all cases in which the tracer method is inapplicable because of the lack of a radioactive isotope, the secondary ion emission could be used for studying self-diffusion problems.

c. Analysis of Low-Concentration Elements

Here, it is a question of analyzing elements whose local concentration is low. Various cases may occur, depending on whether the traces of an element distributed over the entire specimen are to be investigated or whether it is desired to detect the existence of an element within a region which, primarily, is defective in this element while the same element is present at a considerable concentration within the specimen (it has been reported, for example, that aluminum is present in the "black" areas of the distribution of this element within the Al-Mg-Si alloy, discussed in Chapter II).

To determine the accuracy of resolution and the resolving power that can be expected from the analysis, it is primarily necessary to define the ion yield of the considered element. However, this yield depends on the alloy in which this element is present and on the chemical bonds which link it to the other elements. If only an order of magnitude of the detectable concentrations is to be established, the conditions can be simplified to the extreme by assuming that the wanted element retains the same ionization probability, no matter in which alloy it exists. This means that, for an emission lens whose contrast

diaphragm limits the resolution to ε microns, the ion yield which would be $\left[\dfrac{n_i \varepsilon}{n_0 \varepsilon_i}\right]_{P}$ for a pure element would become $c\left[\dfrac{n_i \varepsilon}{n_0 \varepsilon_i}\right]_{P}$ for the element at the atomic concentration c. From the expression for the ultimate resolving power ε it can be derived that the lowest concentration c detectable, in a volume ε^3, with an accuracy of p % is given by the expression

$$ c = \frac{10^4}{p^2} \frac{1}{K \varepsilon^3} \left[\left(\frac{n_0}{n_i}\right)_{\exp} \right]_P $$

This formula, when applied to the case of aluminum, demonstrates that it would be possible to detect a concentration of a few millionths with an accuracy of 10% in a volume of the order of $1\,\mu^3$. Under the same conditions, a concentration of the order of 1% can be detected in the case of copper. Let us mention that if it is a question of a certain element being distributed over the entire specimen, such a highly localized analysis will not be necessary and it will be sufficient to count the ions emitted by the entire imaged field. By retaining the same contrast diaphragm as that which yields a resolution limit of one micron, the ion yield of the pure elements will be $\left(\dfrac{n_0}{n_i}\right)_{\exp}$, while the concentration of the sought element, measured with an accuracy of p % in a volume v, is given by the expression

$$ c = \frac{10^4}{p^2} \frac{1}{K v} \left(\frac{n_0}{n_i}\right)_{\exp} . $$

The sputtering of a layer of one micron in thickness on a field of 0.3 mm diameter would permit the detection, with an accuracy to within 10%, of a concentration of some 10^{-11} in the case of aluminum; in the case of copper, a concentration of the order of a ten-millionth would still be detectable with the same accuracy.

This necessitates, on the one hand, that the ion emissions be measured

with an absolute accuracy (i.e., that the pickup device counts the arrival of individual ions) and, on the other hand, that no "continuous background" will interfere with these measurements. Such a continuous background may be produced by the diffusion of ions on the molecules of the residual gas along their entire path, but the most disturbing phenomenon would be the deposition of matter on the specimen. In fact, the particles extracted from the target by sputtering may rebound from the surface of the electrode A, facing the object, and may return to the specimen where they would deposit as a thin film. If two adjacent regions contained the same element E, one in high concentration and the other in low concentration, the "redeposition" of matter would take place on these two regions and the detection of low contents of E would become impossible. It is difficult to say to what extent this detection would be affected since the degree of "redeposition" depends on the element in question, as well as on the nature, the temperature, and the shape of the electrode A. Nevertheless, in the case of an element distributed within the entire specimen in low concentration, such redeposition is of little significance since it interferes with the accuracy of the analysis to only an extremely slight extent. It is also of interest that the deposition of matter takes place over the entire surface of the object. On observing regions that had not yet been subjected to primary bombardment, this may be a considerable drawback, specifically for investigations of surface layers. A very thin diaphragm, placed in front of the object and leaving only a region of the order of the imaged field open, would eliminate this drawback.

CONCLUSIONS

The results obtained with this analysis method demonstrate that it is

possible to obtain directly distribution images whose limit of resolution is of the order of one micron. However, these images permit only a semiquantitative analysis in the sense that the emission of secondary ions is not always proportional to the concentration of the element sought. In fact, we have seen that the presence of a few percent of an element in a given alloy may, in certain cases, produce a noticeable enhancement of the secondary emission and, on the other hand, that the nature of the bond linking the elements within a chemical combination has some influence on the emission. Under these conditions, it is a rather difficult problem to derive a law linking the intensity of emission to the concentration, and a considerable standardization effort would be required to render the method quantitative. Nevertheless, the dependence on the emission with respect to the chemical bond will be useful for defining in which type of bond the element is present.

With respect to light elements, the analysis encounters only difficulties that have to do with the ion yield of the bombarded specimens. For example, lithium, beryllium, and boron are easy to analyze whereas carbon poses a more difficult problem, which is due to the nature of the bonds linking this carbon to the other elements. The use of negative ions, once the problems of stray emissions are mastered, seems to furnish a valuable aid for easy detection of elements with an electronegative tendency, including oxygen and, no doubt, also carbon.

The identification of oxides furnishes a typical example for the scope of the method. A comparison of images obtained with positive ions and with negative ions will also yield data on the chemical bonds.

The equipment developed by us can be further perfected in numerous points. Thus, it is possible to improve the resolving power of the images and to increase

135

the sensitivity by direct recording of the final electron image. The exact limits of its potentialities can be established only after a sufficient number of individual studies on secondary ion emission have been performed, so as to define all aspects of the phenomenon. However, even in its present state, the method seems highly useful for studying inclusions, precipitates, oxides, and probably carbides and nitrides in metallographic specimens. In addition, the possibility of analyzing insulating objects extends the field of application of the ion microanalysis to all solid specimens. Specifically, natural mineral objects, where light elements frequently are abundant and where the bonds of ion character give the elements an intense secondary emissivity, seem to be the material of choice for this method.

In addition, it is possible to predict applications to isotope analyses and to investigations of surface layers.

Finally, this method has certain advantages over X-ray analysis, such as the possibility of improving the resolving power, detecting light elements, directly obtaining a distribution image, permitting an analysis of surface layers, and making possible an isotope analysis; however, the method is inferior to X-ray analyses in the field of quantitative analysis. Thus, the two methods seem to complement each other and it would be of advantage to use them in combination.

APPENDIX I   /51

The calculation of second-order aberrations in orthogonal systems has been treated in Cotte's thesis in a very general form. Nevertheless, exactly the generality of his formulas makes their direct application to a practical case difficult. Before calculating the aberrations in the case of a magnetic prism

and within the limits of our proposition, let us recall the basic data of Cotte's theory.

The trajectories close to a curve (Γ), at the Gaussian approximation, are calculated by means of Euler-Lagrange equations written in their Hamiltonian form in a system of curvilinear coordinates (x, y, z). In this system of coordinates, (Γ) has the equations $x = 0$ and $y = 0$; the position of a moving point P of the curve (Γ) is determined by its curvilinear abscissa z. Let $\vec{t}$, $\vec{n}$, $\vec{b}$ be the unit vectors of the Frenet-Serret trihedron attached to the point P; by a suitable rotation of the axes $\vec{b}$ and $\vec{n}$ about $\vec{t}$, it is possible to derive an orthogonal triple system which, reduced to Cartesian coordinates, will yield the following expression for the distance between two infinitely close points:

$$ ds^2 = \left[1 - \frac{k \, z}{R \, z} x - \frac{l'z}{T z} y \right]^2 dz^2 - d x^2 - dy^2 \tag{I.1} $$

where R(z) and T(z) are the radii of curvature and of torsion of the curve (Γ) at the point P. For simplifying the calculation, we can take below the case of a magnetic prism. In such a system, the magnetic field has a plane of symmetry where it is natural to place (Γ). For a plane curve, we have $\frac{1}{T} = 0$, $k(z) = 1$, so that the expression of ds^2 becomes

$$ ds^2 = 1 - \theta(z)^2 dz^2 - dx^2 - dy^2 \tag{I.2} $$

where

$$ \theta(z) = \frac{1}{R z} $$

The x axis will then coincide with the normal to the curve (Γ) while the y axis will be perpendicular to the plane of symmetry. Consequently, $\theta(z)$ is positive if the x axis is directed toward the center of curvature and negative in the opposite case.

The magnetic field is projected onto the axes (x, y, z) along H_x, H_y, H_z.

At a point P of (Γ), these values become H_x^0, H_y^0, H_z^0. In the air gap of the electromagnet, for the case that the field can be considered as being uniform,
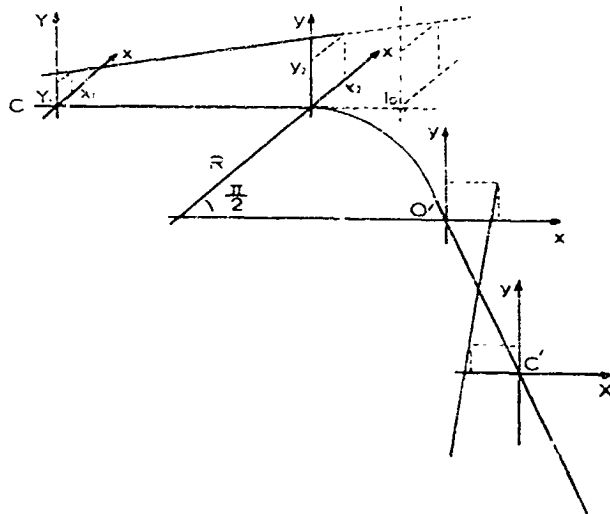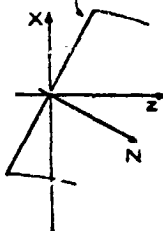

Fig.I.1

ENTRANCE FACE OF THE PRISM

Fig.I.2

we will have $H_x = H_y = 0$. The expansion in series of the vector potential of the magnetic field in the variables x, y makes it possible to write the Hamiltonian of the system, in the vicinity of the curve (Γ), in the form of a sum $H = H_0 + H_1 + H_2 + H_3$. Here, H_1, H_2, H_3 contain, respectively, the terms of the first, second, and third order in x, y, p, and q; the quantities p and q are

the conjugate moments of the dynamic variables x and y: $p = \dfrac{\partial L}{\partial x'}$, $q = \dfrac{\partial L}{\partial y'}$

(with L being the Lagrangian of the system). The quantity H_0 contains the terms of zero order.

The second-order approximation consists in neglecting H_3. This will yield differential equations of the trajectories:

$$\frac{d\,px'}{dz} = xf(z) - g(z) \Bigg)$$
$$\frac{d\,ny'}{dz} = ye\left(\frac{\partial H_y}{\partial x}\right)_0 \Bigg\rangle \qquad\qquad (I.3)$$

with

$$g(z) = eH_y^0 + n\dot\theta$$
$$f(z) = e\left[\theta H_y^0 - \left(\frac{\partial H_y}{\partial x}\right)_0\right]$$

where n denotes the momentum mv, while $\left(\dfrac{\partial H_y}{\partial x}\right)_0$ is the derivative at a point of the curve (Γ). Let us note that $\dfrac{\partial H_x}{\partial y}$ can be replaced by $\dfrac{\partial H_y}{\partial x}$ which is equal to it in virtue of Ampère's theorem.

If (Γ) is the mean trajectory of the particle beam, then $g(z) = 0$ since $R = |R(z)| = \dfrac{mv}{eH_y^0}$. The equations of the trajectories then are written as

$$\frac{d\,nx'}{dz} = xe\left[\theta H_y^0 - \left(\frac{\partial H}{\partial x}\right)_0\right] \Bigg) (a)$$
$$\frac{d\,ny'}{dz} = ye\left(\frac{\partial H_y}{\partial x}\right)_0 \qquad\Bigg\rangle (b) \qquad\qquad (I.4)$$

It will be noted that eqs.(I.4a) and (I.4b) are independent. A trajectory whose tangent to a point is contained in the plane of symmetry or in the first principal section will remain in this plane; a trajectory whose tangent to a point is also tangent to the cylinder whose generatrices are perpendicular to the plane of symmetry and are based on (Γ) will remain in this surface or in the second principal section. A given trajectory is represented by its projections

onto the two principal sections. For particles whose initial velocity is tangent

to the second section, this is true only to within approximately the second

order. In fact, it will be demonstrated below that, in their subsequent motion,

these particles leave the cylindrical surface and move away from this surface at

distances of the second order.

It is specifically convenient to write the solution of the differential

equations governing the motion in matrix form. For this, it is assumed that two

solutions $u(z)$ and $v(z)$ of eq.(4a) and two solutions $w(z)$ and $t(z)$ of eq.(4b)

are known, such that

$$u(a) = 1 \quad u'(a) = 0 \quad w(a) = 1 \quad w'(a) = 0$$
$$v(a) = 0 \quad nv'(a) = 1 \quad t(a) = 0 \quad nt'(a) = 1 \; . \qquad \text{(I.5)}$$

Since the initial conditions of a trajectory at the abscissa point $z = a$ are

$$x(a) = x_a \quad y(a) = y_a \quad \textbf{and} \quad x'(a) = x'_a \quad y'(a) = y'_a \, ,$$

this trajectory will be expressed by

$$x = x_a u(z) + n x'_a v(z) \qquad n x' = n x_a u' + n v' n x'_a$$
$$y = y_a w(z) + n y'_a t(z) \qquad n y' = n y_a w' + n t' n y'_a \qquad \text{(I.6)}$$

which can also be written as

$$\begin{vmatrix} x \\ nx' \end{vmatrix} = M_{za} \begin{vmatrix} x_a \\ n r'_a \end{vmatrix} \quad \textbf{and} \quad \begin{vmatrix} y \\ ny' \end{vmatrix} = N_{za} \begin{vmatrix} y_a \\ ny'_a \end{vmatrix} \, ,$$

where

$$M_{za} = \begin{vmatrix} u(z) & v(z) \\ nu'(z) & nv'(z) \end{vmatrix} \quad N_{za} = \begin{vmatrix} w(z) & (z) \\ nw'(z) & nt'(z) \end{vmatrix}$$

If the trajectories start and end in a region of zero field, the matrices

that represent the uniform and rectilinear motion of the particles will be,

respectively, between the abscissa points a and z_0 and the abscissa points b

and z_1

$$M_{az_0} = \begin{vmatrix} 1 & \dfrac{a - z_0}{n} \\ 0 & 1 \end{vmatrix} \quad \textbf{and} \quad M_{bz_1} = \begin{vmatrix} 1 & \dfrac{z_1 - b}{n} \\ 0 & 1 \end{vmatrix}$$

Let M_{ba} and N_{ba} be the matrices describing the action of the prism in the first and in the second principal section, between the abscissa points O and O' , z = a and z = b.

The plane $z = z_1$ intersects the trajectories along coordinates which are transforms of the position and velocity coordinates in the plane $z = z_0$ by action of the matrices

$$M_{z_1 z_0} = M_{z_1 b} M_{ba} M_{az_0} \quad \textbf{and} \quad N_{z_1 z_0} = M_{z_1'} N_{ba} M_{az_0}$$

in their respective section.

To determine the matrices M_{ba} and N_{ba}, three regions can be differentiated. At the entrance, an infinitely thin "passage layer" sees the magnetic field pass from a zero value to a finite value, which it assumes in the air gap of the electromagnet. In this air gap, which is the second region, the field remains uniform. Finally, at the exit, the magnetic field returns to its zero value through a "passage layer" identical to that encountered at the entrance side. The transition matrices describing the action of the prism at the entrance, for example, are as follows for the first and for the second principal section, respectively:

$$M_e = \begin{vmatrix} 1 & 0 \\ - e l l \operatorname{tg} \varepsilon' & 1 \end{vmatrix} \quad \textbf{and} \quad N_e = \begin{vmatrix} 1 & 0 \\ + e l l \operatorname{tg} \varepsilon' & 1 \end{vmatrix}$$

where H is the value of the magnetic field and ε' is the angle of the tangent to the trajectory with the normal to the entrance face (see Fig.I.2). The action of the prism in the first principal section is expressed by

$$\begin{vmatrix} x_b \\ nx_b' \end{vmatrix} = \begin{vmatrix} 1 & 0 \\ eH\,\mathrm{tg}\,\varepsilon'' & 1 \end{vmatrix} \times \begin{vmatrix} \cos\dfrac{z-a}{R} & \dfrac{R}{n}\sin\dfrac{z-a}{R} \\ -\dfrac{n}{R}\sin\dfrac{z-a}{R} & \cos\dfrac{z-a}{R} \end{vmatrix} \times$$

$$\times \begin{vmatrix} 1 & 0 \\ -eH\,\mathrm{tg}\,\varepsilon' & 1 \end{vmatrix} \times \begin{vmatrix} x_a \\ nx_a' \end{vmatrix},$$

where ε'' is the angle of the tangent to the trajectory with the normal to the exit face of the prism. In the second principal section, we find

$$\begin{vmatrix} y_b \\ ny_b' \end{vmatrix} = \begin{vmatrix} 1 & 0 \\ -eH\,\mathrm{tg}\,\varepsilon'' & 1 \end{vmatrix} \times \begin{vmatrix} 1 & \dfrac{(z-a)}{n} \\ 0 & n \end{vmatrix} \times$$

$$\times \begin{vmatrix} 1 & 0 \\ eH\,\mathrm{tg}\,\varepsilon' & 1 \end{vmatrix} \times \begin{vmatrix} y_a \\ ny_a' \end{vmatrix}.$$

From these statements it is easy to derive eqs.(15) and (16) which give /53 the positions of the conjugate points in each of the principal sections. The

	First Principal Section	Second Principal Section
Region without Field extending in front of the prism	$u(z) = 1,\ u'(z) = 0$ $v(z) = \dfrac{z-z_0}{n},\ v'(z) = \dfrac{1}{n}$	$w(z) = 1,\ w'(z) = 0$ $l(z) = \dfrac{z-z_0}{n},\ l'(z) = \dfrac{1}{n}$
Passage layer at the Entrance to the Magnet	$u(a) = 1,\ u'(a) = \dfrac{1}{2R}$ $v(a) = \dfrac{2R}{n},\ v'(a) = \dfrac{2}{n}$	$w(a) = 1,\ w'(a) = -\dfrac{1}{2R}$ $l(a) = \dfrac{2R}{n},\ l'(a) = 0$
Region of uniform Field	$u(z) = \cos\dfrac{z-a}{R} + \dfrac{1}{2}\sin\dfrac{z-a}{R}$ $v(z) = \dfrac{2R}{n}\left(\cos\dfrac{z-a}{R} + \sin\dfrac{z-a}{R}\right)$	$w(z) = 1 - \dfrac{z-a}{2h}$ $l(z) = \dfrac{2R}{n}$
Passage layer at the Exit from the Magnet	$u(z) = \dfrac{1}{2},\ u'(z) = -\dfrac{3}{4R}$ $v(z) = \dfrac{2R}{n},\ v'(z) = -\dfrac{1}{n}$	$w(z) = 1 - \dfrac{\pi}{4},\ w'(z) = -\dfrac{1}{2R}\left(2 - \dfrac{\pi}{4}\right)$ $l(z) = \dfrac{2R}{n},\ l'(z) = -\dfrac{1}{n}$
Region of Zero Field extending after the Prism	$u(z) = \dfrac{1}{2} - \dfrac{3}{4}\cdot\dfrac{z-b}{R}$ $v(z) = \dfrac{2R}{n} - \dfrac{z-b}{n}$	$w(z) = 1 - \dfrac{\pi}{4} - \dfrac{z-b}{2R}\left(2 - \dfrac{\pi}{4}\right)$ $l(z) = \dfrac{2R}{n} - \dfrac{z-b}{n}$

calculation of second-order aberrations requires knowledge of the functions u, v, w, t as well as of their derivative. In the symmetry case, which is treated here, we have $-\tan \epsilon' = \tan \epsilon'' = \frac{1}{2}$. The matrix formulation permits to establish, without difficulty, a Table of these functions for each of the regions traversed by the particles.

1. Calculation of Second-Order Aberrations

The formulas derived in the preceding Section permit to calculate, to within the second order, the position and velocity coordinates in any plane z, provided that the value of these coordinates in the plane $z = z_0$ is known. If a more accurate definition of the trajectories is desired, the equations of motion must be solved with consideration of the term H_3. It is also possible to introduce a parameter ϵ for describing the heterogeneity of velocity of the particles.

Since u, v, w, t are particular solutions, defined above, of the equations of motion written on the basis of the Hamiltonian $H^0 = H_0 + H_1 + H_2$, the solution of these equations can be given the following form:

$$x = C_1 u + C_2 v \qquad y = \Gamma_1 w + \Gamma_2 t$$
$$p = n C_1 u' + n C_2 v' \qquad q = n \Gamma_1 w' + n \Gamma_2 t' \qquad (I.7)$$

where the constants C_1, C_2, Γ_1, and Γ_2 depend on the initial conditions. It is also possible to determine solutions of the form of eq.(7) for the differential equations of the trajectories written on the basis of the Hamiltonian $H = H_0 + H^*$ where H^* contains the third-order terms originating from H_3 and the terms introduced by ϵ; then C_1, C_2, Γ_1, Γ_2 become functions of z. On returning to the second-order approximation, it is necessary to return to the solution of equations written on the basis of H^0, so that C_1, C_2, Γ_1, Γ_2 can be given the form of an expansion in series in infinitely small quantities of the first order,

which are the initial coordinates.

Now, the entire problem reduces to a calculation of the various coefficients in these series, which coefficients are functions of z. To do this, Cotte considers that the expressions (I.7) define a change in variables transforming x, y, p, q into C_1, C_2, Γ_1, Γ_2. This same author mentioned that this transformation is canonical: The new variables C_1, C_2, Γ_1, Γ_2 are dynamic variables. Since C_1, Γ_1 are canonically conjugate to C_2, Γ_2, the differential $\underline{/54}$ equations of the trajectories will assume the following form:

$$\frac{dC_1}{dz} = \frac{\partial K}{\partial C_2} \qquad \frac{dC_2}{dz} = -\frac{\partial K}{\partial C_1}$$
$$\frac{d\Gamma_1}{dz} = \frac{\partial K}{\partial \Gamma_2} \qquad \frac{d\Gamma_2}{dz} = -\frac{\partial K}{\partial \Gamma_1} \qquad\qquad (I.8)$$

where $K(C_1, C_2, \Gamma_1, \Gamma_2, z)$ is the new Hamiltonian function. The solution of the system (I.8) which satisfies the initial conditions

$$C_1(s) = \xi_1, \quad C_2(d) = \xi_2, \quad \Gamma_1(s) = \eta_1, \quad \Gamma_2(d) = \eta_2$$

is written in the form of expansions in series in ξ_1, ξ_2, η_1, η_2 whose expressions are as follows:

$$C_1(z) = \xi_1 + \varepsilon\varphi_1(z) + A_{00}\frac{\varepsilon^2}{2} + \sum_i A_{0i}\varepsilon\xi_i$$
$$+ \frac{1}{2}\sum_{i,k}(A_{ik}\xi_i\xi_k + E_{ik}\eta_i\eta_k)$$
$$C_2(z) = \xi_2 + \varepsilon\varphi_2(z) + B_{00}\frac{\varepsilon^2}{2} + \sum_i B_{0i}\varepsilon\xi_i$$
$$+ \frac{1}{2}\sum_{i,k}(B_{ik}\xi_i\xi_k + F_{ik}\eta_i\eta_k)$$
$$\Gamma_1(z) = \eta_1 + \sum_i C_{0i}\varepsilon\eta_i + \sum_{i,k}C_{ik}\xi_i\eta_k$$
$$\Gamma_2(z) = \eta_2 + \sum_i D_{0i}\varepsilon\eta_i + \sum_{i,k}D_{ik}\xi_i\eta_k$$

where

$$A_{ik} = A_{ki}, \quad E_{ik} = E_{ki}, \quad B_{ik} = B_{ki}, \quad F_{ik} = F_{ki}$$

The expressions of these coefficients will then be:

Chromatic dispersion:

$$\varphi_1 = \int_s^z \omega_2 dz, \qquad \varphi_2 = -\int_d^z \omega_1 dz.$$

Chromatic aberrations:

$$A_{00} = \int_s^z (\bar{\omega}_2 + 2\lambda_{12}\varphi_1 + 2\lambda_{22}\varphi_2 + \alpha_{12}\varphi_1^2$$
$$+ 2\alpha_{21}\varphi_1\varphi_2 + \alpha_{22}\varphi_2^2) dz$$

$$A_{01} = \int_s^z (\lambda_{12} + \varphi_1\alpha_{12} + \varphi_2\alpha_{21}) dz$$

$$A_{02} = \int_s^z (\lambda_{22} + \varphi_1\alpha_{21} + \varphi_2\alpha_{22}) dz$$

$$B_{00} = -\int_d^z (\bar{\omega}_1 + \alpha_{11}\varphi_1^2 + 2\alpha_{12}\varphi_1\varphi_2 + \alpha_{21}\varphi_2^2$$
$$+ 2\lambda_{11}\varphi_1 + 2\lambda_1\varphi_{22}) dz$$

$B_{01} = -\int_d^z (\lambda_{11} + \alpha_{11}\varphi_1 + \alpha_{12}\varphi_2) dz$	$B_{02} = -\int_d^z (\lambda_{12} + \alpha_{12}\varphi_1 + \alpha_{21}\varphi_2) dz$
$C_{01} = \int_s^z \mu_{12} dz$	$C_{02} = \int_s^z \mu_{22} dz$
$D_{01} = -\int_d^z \mu_{11} dz$	$D_{02} = -\int_d^z \mu_{12} dz$

2. Geometric Aberrations

$A_{11} = \int_s^z \alpha_{11} dz$	$A_{12} = \int_s^z \alpha_{21} dz$	$A_{12} = A_{21}$	$A_{22} = \int_s^z \alpha_{22} dz$
$B_{11} = -\int_d^z \alpha_{11} dz$	$B_{12} = -\int_d^z \alpha_{12} dz$	$B_{12} = B_{21}$	$B_{22} = -\int_d^z \alpha_{21} dz$
$C_{11} = \int_s^z \gamma_1 dz$	$C_{12} = \int_s^z \beta_{12} dz$	$C_{21} = \int_s^z \gamma_{21} dz$	$C_{22} = \int_s^z \beta_{22} dz$

$$D_{11} = -\int_d^z \beta_{11} dz, \quad D_{12} = -\int_d^z \gamma_1 dz, \quad D_{21} = -\int_d^z \beta_{21} dz, \quad D_{22} = -\int_d^z \gamma_2 dz$$

$$E_{11} = \int_s^z \beta_{21} dz, \quad E_{12} = \int_s^z \gamma_2 dz, \quad E_{12} = E_{21}, \quad E_{22} = \int_s^z \beta_{22} dz$$

$$F_{11} = -\int_d^z \beta_{11} dz, \quad F_{12} = -\int_d^z \gamma_1 dz, \quad F_{12} = F_{21}, \quad F_{22} = -\int_d^z \beta_{12} dz$$

None of these coefficients are independent; relations exist between them such as

$$E_{22} - C_{22} = 0 \qquad E_{11} - D_{11} = 0$$
$$E_{21} - C_{21} = 0 \qquad F_{12} - D_{12} = 0$$

as well as ten relations of the type of

$$A_{01}(z) + B_{02}(z) = \text{constant} .$$

In the case of a magnetic prism, the functions of z which appear in the integrals are expressed by

$$\omega_1 = u\frac{\partial g}{\partial \varepsilon} \qquad \omega_2 = v\frac{\partial g}{\partial \varepsilon} \qquad \bar\omega_1 = u\frac{\partial^2 g}{\partial \varepsilon^2} \qquad \bar\omega_2 = v\frac{\partial^2 g}{\partial \varepsilon^2}$$

$$\lambda_{11} = -u'^2\frac{\partial n}{\partial \varepsilon} \qquad \lambda_{12} = -u'v'\frac{\partial n}{\partial \varepsilon} \qquad \lambda_{22} = -v'^2\frac{\partial n}{\partial \varepsilon}$$

$$\mu_{11} = -w'^2\frac{\partial n}{\partial \varepsilon} \qquad \mu_{12} = -w't'\frac{\partial n}{\partial \varepsilon} \qquad \mu_{22} = -t'^2\frac{\partial n}{\partial \varepsilon}$$

where

$$\frac{\partial n}{\partial \varepsilon} = m \quad \text{and} \quad \frac{\partial g}{\partial \varepsilon} = m\theta .$$

$$\alpha_{11} = 3Auu'^2 + Bu^3$$
$$\alpha_{21} = A(uv'^2 + 2vu'v') + Buv^2$$
$$\alpha_{12} = A(2uu'v' + vu'^2) + Buv^2$$
$$\alpha_{22} = 3Avv'^2 + Bv^3$$
$$\gamma_1 = Guwt + Auw't' + Du'wt$$

$$\beta_{11} = Guw^2 + Auw'^2 + Du'w^2$$
$$\beta_{12} = Gut^2 + Aut'^2 + Du't^2$$
$$\beta_{21} = Gvw^2 + Avw'^2 + Dv'w^2$$
$$\beta_{22} = Gvt^2 + Avt'^2 + Dv't^2$$
$$\gamma_2 = Gvwt + Avw't' + Dv'wt$$

where

155

$$A = -\theta n, \quad B = e\left(\frac{\partial^2 H_y}{\partial z^2}\right)_0, \quad 2e\theta\left(\frac{\partial H_y}{\partial x}\right)_0, \quad D = +e\frac{dH^0}{e}$$

$$G = e\left(\frac{\partial^2 H_y}{\partial r^2}\right)_0 + e\theta\left(\frac{\partial H_y}{\partial x}\right)_0.$$

In the hypothesis of an equivalent magnet, the magnetic field changes abruptly in value as soon as a passage layer is traversed, so that the functions B, D, and G become infinite; the same holds true for the coefficients α_{1k}, β_{1k}, and γ_1. Nevertheless, a calculation of the aberration coefficients remains possible since α_{1k}, β_{1k}, and γ_1 enter only with their integrals. The Table of values of the functions A, B, D, G can be established for each of the regions traversed by the particles.

	A	B	D	G
In front of the Magnet .	o	o	o	o
Passage layer (Entrance).	$-\theta n$	$e\left(\frac{\partial^2 H_y}{\partial z^2}\right)_0 - 2e\theta\left(\frac{\partial H_y}{\partial x}\right)_0$	$e\frac{dH_y^0}{dz} \to +\infty$	$-e\left(\frac{\partial^2 H_y}{\partial z^2}\right)_0 + e\theta\left(\frac{\partial H_y}{\partial x}\right)_0$
Air Gap	$-\theta n$	o	o	o
Passage layer (Exit) .	$-\theta n$	$e\left(\frac{\partial^2 H_y}{\partial z^2}\right)_0 - 2e\theta\left(\frac{\partial H_y}{\partial x}\right)_0$	$e\frac{dH_y}{dz} < 0 \to -\infty$	$-e\left(\frac{\partial^2 H_y}{\partial z^2}\right)_0 + e\theta\left(\frac{\partial H_y}{\partial x}\right)_0$
After the Magnet . . .	o	o	o	o

The orientation of the axes (x, y, z) is as indicated in Fig.I.1: the x-axis is directed opposite to the center of curvature, so that θ is negative. Let us put $H_y^0(z) = h(z)$, $h(z) > 0$ and let us denote by N the normal to the entrance face, which yields

$$dN = \sin \varepsilon'dx, \quad dN = \cos \varepsilon'dz, \quad \left(\frac{\partial H_y}{\partial x}\right)_0 = \frac{dh}{dn}\sin \varepsilon'.$$

This leaves three types of integrals to calculate:

$$I_1 = \int f(z)\left(\frac{\partial H_y}{\partial x}\right)_\bullet dz, \qquad I_2 = \int f(z)\cdot \theta(z)\left(\frac{\partial H_y}{\partial x}\right)_\bullet dz,$$

$$I_3 = \int f(z)\left(\frac{\partial^2 H_y}{\partial x^2}\right)_\bullet dz$$

extending at the "thickness" of the passage layers, where f(z) is a function which remains finite on passing through this layer.

Let a and b be the curvilinear abscissas of the points O and O' . At the entrance to the prism, we have

$$J_1 = f(a)\cdot \int_0^H \frac{dh}{dN}\cdot \frac{\sin \varepsilon'}{\cos \varepsilon'}\cdot dN = f(a)\cdot \operatorname{tg}\varepsilon' H = -f(a) H \operatorname{tg}\varepsilon$$

and, at the exit,

$$I_1 = f(b)\cdot \int_H^0 \frac{dh}{dN}\cdot \frac{\sin \varepsilon''}{\cos \varepsilon''}\cdot dN = f(b)\cdot \operatorname{tg}\varepsilon''(-H)$$
$$= -f(b)\cdot H \operatorname{tg}\varepsilon.$$

Since $\theta(z) = -\dfrac{eh}{n}$ we will have, at the entrance to the prism,

$$I_2 = f(a)\cdot \int_0^H -\frac{eh}{n}\cdot dh\cdot \operatorname{tg}\varepsilon'$$
$$= -\frac{e}{n}\cdot f(a)\operatorname{tg}\varepsilon'\frac{H^2}{2} = \frac{eH^2}{2n}\cdot \operatorname{tg}\varepsilon\cdot f(a)$$

and, at the exit,

$$I_2 = f(b)\cdot \int_H^0 -\frac{eh}{n}\cdot dh\cdot \operatorname{tg}\varepsilon''$$
$$= -\frac{e}{n}f(b)\cdot \operatorname{tg}\varepsilon''\left(-\frac{H^2}{2}\right) = \frac{eH^2}{2n}\cdot \operatorname{tg}\varepsilon\cdot f(b).$$

With respect to the integral I_3, we can state that

$$I_3 = f(a)\int_0^H d\left(\frac{dh}{dn}\sin \varepsilon'\right)\operatorname{tg}\varepsilon' = f(a)\cdot \operatorname{tg}\varepsilon'\left[\frac{dh}{dn}\sin \varepsilon'\right]_0^H$$

and that $\dfrac{dh}{dn}$ is zero at the entrance as well as the exit of one and the same passage layer. Consequently, we have $I_3 = 0$.

The functions B, D, G appear only at the entrance and exit of the prism, over the intermediary of integrals of the type I_1 and I_2. Conversely, the function A intervenes all along the air gap where, associated with the functions u, v, u', v', w', and t', it gives rise to the calculation of integrals of the type $\int_o^\pi \cos{}^m\Theta \sin{}^n\Theta d\Theta$, where m and n are integers while Θ is an integration variable.

The functions u, v, w, t and their first derivatives have been defined above. However, let us note that, on traversing the entrance layer for example, it is convenient to use the function $\frac{e\bar{h}(z)}{2n}$ for u' each time that u' is associated with D in the calculation of an integral of the type I_2.

After calculations which offer no further difficulty than the length, the following Table can be established:

$\int_a^b \alpha_{,1} dz = \frac{9\pi}{16R^2}$	$\int_a^b \beta_{,1} dz = \left[\frac{7}{8} - \left(1 - \frac{\pi}{4}\right)^2\right]\frac{\pi}{R^2}$
$\int_a^b \alpha_{z1} dz = \frac{3}{\pi}$	$\int_a^b \beta_{z1} dz = \left[3 + 2\left(1 - \frac{\pi}{4}\right)^2\right]\frac{1}{R}$
$\int_a^b \alpha_{1z} dz = \frac{5}{3}\cdot\frac{1}{R}$	$\int_a^b \beta_{z} dz = \frac{6}{\pi}$
$\int_a^b \alpha_{zz} dz = \frac{8R}{\pi^2}$	$\int_a^b \beta_{zz} dz = \frac{16R}{\pi^2}$
$\int_a^b \gamma_1 dz = \left(3 - \frac{\pi}{4}\right)\frac{1}{R}$	$\int_a^b \gamma_z dz = (8 - \pi)\frac{1}{\pi}$

For calculating the value of the coefficients in any plane $z = z_1$, it can be stated that

$$\int_s^{z_1} = \int_s^a + \int_a^b + \int_b^{z_1}$$

so that, in taking the point z = s, in a region of zero field, we have $\int_s^a = \int_b^{z_1} = 0$ since A = B = D = G = 0 and, consequently, $\int_s^{z_1} = \int_a^b$. The above Table thus gives the values for the coefficients describing the geometric aberrations in the expansions C_1, C_2, Γ_1, and Γ_2.

With a prism, operating under symmetry conditions, the crossover of the emission lens is located at 2R of the entrance face while the image of the object surface, given by this lens, is located at $\dfrac{8R}{3}$ of the crossover. If the crossover of the lens is placed in the plane z = z_0, we have

$$a = 2R + z_0, \quad b = \left(2 - \frac{\pi}{2}\right) R + z_0.$$

It is possible to define a trajectory by the coordinates x_0, y_0 of its intersection with the plane z = z_0 and by the angles made by its projections onto the planes (x, z) and (y, z) with the z axis. Let α and β be the angles that define the axis of a trajectory pencil converging initially toward a point of the image I_0 and having an aperture limited by the geometric dimensions of the crossover.

Then, ξ_1, ξ_2, η_1, η_2 assume the following values:

$$\xi_1 = x_0 \qquad \xi_2 = \left(\alpha - \frac{3}{8}\frac{x_0}{R}\right)n$$

$$\eta_1 = y_0 \qquad \eta_2 = \left(\beta - \frac{3}{8}\frac{y_0}{R}\right)n.$$

In the plane $z_1 = b + 2R$, eqs.(7) will yield

$$x(z_1) = C_1(z_1).u(z_1) + C_2(z_1).v(z_1)$$
$$y(z_1) = \Gamma_1(z_1).w(z_1) + \Gamma_2(z_1).t(z_1)$$

and, since,

$$u(z_1) = -1, \quad w(z_1) = -1, \quad v(z_1) = t(z_1) = 0,$$

we have

$$x(z_1) = -C_1(z_1)$$
$$y(z_1) = -\Gamma_1(z_1).$$

For comparing the value of the aberrations calculated at the level of the crossover with those of the aberrations measured by Hennequin, let us take $\epsilon = 0$ and $x_0 = y_0 = 0$. This will yield

$$x = -4R\alpha^2 - 8R\beta^2$$
$$y = -16R\alpha\beta.$$

The term in α^2 is identical to that obtained by a classical geometric calculation; with respect to the term in β^2, Hennequin found a coefficient having a value of about $10R$, which means that the agreement is satisfactory.

3. Chromatic Aberrations

The coefficients A_{00} and B_{00} will not be calculated here since below we will neglect the terms in ϵ^2. This leaves only the functions φ_1 and φ_2 that determine the dispersion of the prism to be calculated, as well as the coefficients A_{01}, A_{02}, B_{01}, B_{02}, C_{01}, C_{02}, D_{01}, D_{02}. Let us note that it is sufficient to take the integrals between the limits a and b since, outside of these limits, the magnetic field is zero and since C_1, C_2, Γ_1, Γ_2 return to being constants.

Dispersion of the prism:

$$\varphi_1(z) = \int_a^z m v \theta dz = -\frac{2mR}{n}\left(1 + \sin\frac{z-a}{R} - \cos\frac{z-a}{R}\right)$$
$$\varphi_2(z) = -\int_a^z m u \theta dz = m\left(\frac{1}{2} + \sin\frac{z-a}{R} - \frac{1}{2}\cos\frac{z-a}{R}\right)$$

At the level of the crossover C', $z_1 = b + 2R$, $x(z_1) = -C_2$, neglecting the second-order aberrations, we will thus have

$$x(z_1) = -x_0 - \epsilon\varphi_1 = -x_0 + \frac{4mR}{n}\epsilon$$

i.e., in view of the fact that $\epsilon = \Delta v$ and $n = mv$:

$$x(z_1) = -x_0 - 4R\frac{\Delta v}{v} \quad \text{or else} \quad x(z_1) = -x_0 + 2R\frac{\Delta V}{V}$$

which is the classical expression for the dispersion in the case of the prism used.

Since $\dfrac{\partial n}{\partial \varepsilon} = m$, the functions λ_{11}, λ_{12}, λ_{22}, μ_{11}, μ_{12}, μ_{22} assume the following form:

$$\lambda_{11} = -mu'^2, \quad \lambda_{12} = -mu'v', \quad \lambda_{22} = -mv'^2$$
$$\mu_{11} = -n\,v'^2, \quad \mu_{12} = -mv't', \quad \mu_{22} = -mt'^2$$

Since $t' = 0$ in the prism, it follows that μ_{12} and μ_{22} are zero and, consequently $C_{01} = C_{02} = L_{b2} = 0$. This leaves

$$D_{01} = \int_a^b mw'^2 dz = \frac{m}{4R^2}\int_a^b dz = \frac{m\pi}{R8}.$$

The calculation of the coefficients A_{01}, A_{02}, B_{01}, $B_{02} = -A_{01}$ is much longer. In fact, it is necessary to calculate a Table of the nine integrals, as follows:

$$\int_a^b \lambda_{11}dz = -\frac{m}{R}\left(\frac{5\pi}{16} - \frac{1}{2}\right) \qquad \int_a^b \lambda_{12}dz = -\frac{3m}{2n}\left(\frac{\pi}{2} - 1\right) \qquad \int_a^b \lambda_{22}dz = -\frac{4mR}{n^2}\left(\frac{\pi}{2} - 1\right)$$

$$\int_a^b \varphi_1\alpha_{11}dz = \frac{m}{R}\left(\frac{15\pi}{64} - \frac{5\pi}{16}\right) \qquad \int_a^b \varphi_1\alpha_{12}dz = \left(\frac{3\pi}{8} - 1\right)\frac{m}{n} \qquad \int_a^b \varphi_1\alpha_{12}dz = -\frac{2mR}{n^2}\left(6 - \frac{\pi}{4}\right)$$

$$\int_a^b \varphi_2\alpha_{12}dz = \frac{m}{R}\left(\frac{5\pi}{64} - \frac{3}{4}\right) \qquad \int_a^b \varphi_2\alpha_{21}dz = \left(\frac{3\pi}{8} - 3\right)\frac{m}{n} \qquad \int_a^b \varphi_2\alpha_{22}dz = \frac{mR}{n^2}\left(2 - \frac{3\pi}{2}\right)$$

By simple addition of the results in each column, this will yield the value of the wanted coefficients

$$A_{01} = -\frac{5}{2}\cdot\frac{m}{n}, \qquad A_{02} = -6\frac{mR}{n^2},$$
$$B_{01} = -\frac{9}{8}\frac{m}{R}, \qquad B_{02} = \frac{5}{2}\cdot\frac{m}{n}.$$

The values of the coefficients Γ and C, reduced to the chromatic aberrations, are then as follows:

$$\Gamma_1(b) = y_0 \quad \text{and} \quad \Gamma_2(b) = n\left(\beta - \frac{3y_0}{8R}\right) + \frac{m\pi}{8R} y_0 \varepsilon$$

$$C_1(b) = x_0 - 4\frac{m\varepsilon}{n} R - \frac{1}{4}\frac{m\varepsilon}{n} x_0 - 6\frac{m\varepsilon}{n} R\alpha$$

$$C_2(b) = n\alpha - \frac{3x_0}{8R} n + \frac{3}{2} m\varepsilon + \frac{3}{16} m\varepsilon \frac{x_0}{R} + \frac{5}{2} m\varepsilon\alpha.$$

At the level of the crossover, we have $x(z_1) = -C_1$ from which, neglecting the geometric aberrations, we obtain

$$x(z_1) = -x_0 + \frac{4mR}{n}\varepsilon + \frac{1}{4}\frac{m\varepsilon}{n} x_0 + 6\frac{m\varepsilon}{n} R\alpha.$$

In the plane $z = b$, we find

$$x(b) = u(b)C_1(b) + v(b)C_2(b) = \frac{C_1}{2} + \frac{2R}{n} C_2$$

i.e., neglecting the geometric aberrations,

$$x(b) = 2R\alpha - \frac{x_0}{4} + \frac{m\varepsilon}{n} R + \frac{1}{8}\frac{m\varepsilon}{n} x_0 + 2\frac{m\varepsilon}{n} R\alpha.$$

Taking into consideration all second-order aberrations (except that in ε^2), we obtain

$$x(b) = 2R\alpha - \frac{x_0}{4} + \frac{m\varepsilon}{n} R + \frac{1}{8}\frac{m\varepsilon}{n} x_0$$
$$+ \frac{2m\varepsilon}{n} R\alpha - R\alpha^2 - 2R\beta^2 - \frac{x_0\alpha}{4} - \frac{y_0\beta}{2}$$

$$y(b) = 2R\beta - \frac{\pi - 1}{4} y_0 + \frac{\pi}{4}\frac{m\varepsilon}{n} y_0 - 2\pi R\alpha\beta$$
$$+ \frac{\pi}{4} x_0\beta - \left(\frac{\pi}{4} + 2\right) y_0\alpha$$

and

$$x(z_1) = -x_0 + \frac{4m\varepsilon}{n} R + \frac{1}{2}\frac{m\varepsilon}{n} x_0 + \frac{6m\varepsilon}{n} R\alpha - 4R\alpha^2 - 8R\beta^2$$
$$+ (\pi - 2)y_0\beta$$
$$y(z_1) = -y_0 - 16R\alpha\beta + (\pi - 2)y_0\alpha.$$

153

1. Castaing, R.: Doctorate Thesis, Paris, O.N.E.R.A., Ed. Publ., No.55, 1951.

2. Castaing. R.: Advances in Electronics, Vol.XIII, p.317, Academic Press,
    New York, 1960.

3. Castaing, R. and Guinier, A.: Proc. Conf. on Elec. Microscopy, Delft,
    Martinus Nijhoff, Ed., La Haye, pp.60-63, 1949.

4. Cosslett, V.E. and Duncumb, P.: Nature, Vol.177, p.1172, 1956.

5. Duncumb, P. and Melford, D.A.: Proc. of the Second International Symposium
    on X-Ray Microanalysis, Stockholm, Elsevier Publishing Co., Amsterdam,
    p.358, 1959.

6. Philibert, J.: J. of the Inst. of Metals, Vol.90, p.241, 1961.

7a. Dempster, A.: Proc. Amer. Phil. Soc., Vol.75, p.755, 1935.

7b. Graig, R.D., Errock, G.A., and Waldron, J.D.: Advances in Mass Spectro-
    metry, p.126, Pergamon Press, 1959.

8. Wenner, G.K.: Advances in Electronics, Vol.VII, p.239, Academic Press,
    New York, 1755.

9. Veksler, V.I. and Benyaminovich, M.B.: Zhur. Tekh. Fiz., Vol.26, p.1671,
    1956.

10a. Stanton, H.E.: Bull. Amer. Phys. Soc., Ser.II, Vol.2, p.34, 1956.

10b. Stanton, H.E.: J. Appl. Phys., Vol.31, p.678, 1960.

11a. Bradley, R.C., Stabler, R.C., and Arakengy, A.: Bull. Amer. Phys. Soc.,
    Ser.II, Vol.2, p.269, 1956.

11b. Arakengy, A. and Bradley, R.C.: Bull. Amer. Phys. Soc., Ser.II, Vol.3,
    p.193, 1958.

11c. Bradley, R.C.: J. Appl. Phys., Vol.30, p.1, 1959.

12a. Honig, R.E.: Bull. Amer. Phys. Soc., Ser.II, Vol.2, p.34, 1957.

12b. Honig, R.E.: Advances in Mass Spectrometry, p.161, Pergamon Press, 1959.

12c. Honig, R.E.: J. Appl. Phys., Vol.29, p.549, 1958.

13a. Herzog, R.F.K. and Vichboeck, F.P.: Phys. Rev., Vol.76, p.855, 1949.

13b. Herzog, R.F.K. and Liebl, H.J.: Phys. Rev., Vol.34, p.2893, 1963.

14a. Castaing, R., Jouffrey, B., and Slodzian, G.: Comptes Rendus Ac.Sc.,
        Vol.251, p.1010, 1960.

14b. Castaing, R. and Slodzian, G.: Proc. Conf. on Elec. Microscopy, Delft,
        Vol.1, p.169, 1960.

14c. Castaing, R. and Slodzian, G.: Comptes Rendus Ac. Sc., Vol.255, p.1893,
        1962.

14d. Castaing, R. and Slodzian, G.: Journal de Microscopie, Vol.1, No.6, p.395,
        1962.

15a. Fogel, Ya.M., Slabospitskiy, R.P., and Rastrepin, A.B.: Zhur. Tekh. Fiz.,
        No.1, p.63, 1960.

15b. Fogel, Ya.M., Slabospitskiy, R.P., and Karnaukhov, I.M.: Zhur. Tekh.
        Phys., Vol.30, p.824, 1960.

16. Magnan, C. et al.: Treatise on Electron Microscopy (Traité de Microscopie
        Électronique). Hermann, Paris, 1961.

17. Johansson, H.: Ann. der Phys., Vol.18, p.385, 1933.

18a. Septier, A.: Doctorate Thesis, Paris, 1954.

18b. Septier, A.: Publication of C.E.R.N. 59-1, Geneva, 1958.

19. Fert, Cn. and Simon, R.: Comptes Rendus Ac. Sc., Vol. 244, p.1177, 1957.

20. Simon, R.: Doctorate Thesis, Toulouse, 1959.

21. Zworykin, V.K. et al.: Electron Optics and the Electron Microscope, John
        Wiley and Sons, New York, 1946.

22. Möllenstedt, G.: Meeting of the German Society of Electron Microscopy,

Innsbruck, 1953.

23. Jouffrey, B.: Diploma of Higher Education, Paris, 1960.

24. Cotte, M.: Doctorate Thesis, Paris, 1938.

25. Hennequin, J.F.: Diploma of Higher Education, Paris, 1960.

26. El Hili, A.: Thesis 3rd Cycle, Paris, 1962.

27. Guépin, J.: Thesis 3rd Cycle, Paris, 1963.

28. Regenstreif, E.: Doctorate Thesis, Paris, 1951.

29a. Bernard, R. and Goutte, R.: Comptes Rendus Ac. Sc., Vol.246, p.2597, 1958.

29b. Bernard, R., Goutte, R., Gaillaud, C., and Javelas, R.: Colloquium of
      Ion Bombardment (Colloque sur le bombardement ionique). Bellevue, Ed.
      of C.N.R.S., 1962.

30. Gauzit, M.: Doctorate Thesis, Paris, 1954.

31a. Arnot, F.L.: Proc. Roy. Soc. A, Vol.158, p.137, 1937.

31b. Arnot, F.L. and Milligan, J.: Proc. Roy. Soc. A, Vol.156, p.538, 1936,

31c. Arnot, F.L. and Beckett, C.: Proc. Roy. Soc. A, Vol.168, p.103, 1938.

32. Sloane, R.H. and Watt, C.S.: Proc. Phys. Soc., Vol.61, p.217, 1948.

33a. Mitropan, I.M. and Gumeniuk, V.S.: Zhur. Eksp. i Teor. Fiz., Vol.32,
      p.214, 1957.

33b. Mitropan, I.M. and Gumeniuk, V.S.: Zhur. Eksp. i Teor. Fiz., Vol.34,
      p.135, 1958.

SECOND THESIS

SUGGESTIONS GIVEN BY THE FACULTY

DIFFRACTION OF SLOW ELECTRONS

Seen and approved:

Paris 22 November 1963

Dean of the Faculty of Sciences,

Marc Zamansky

Seen and passed for printing:

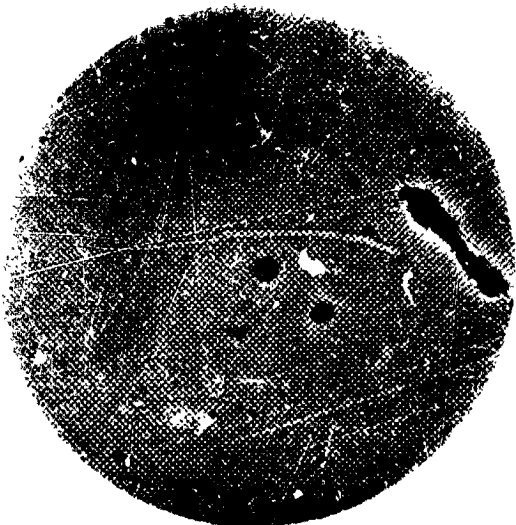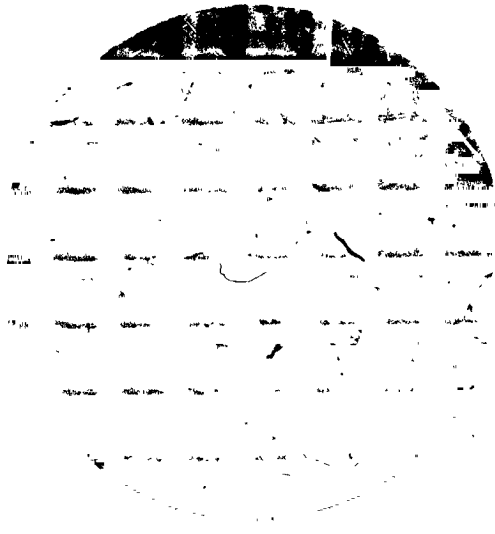Rector of the Academy of Paris,

Jean Roche
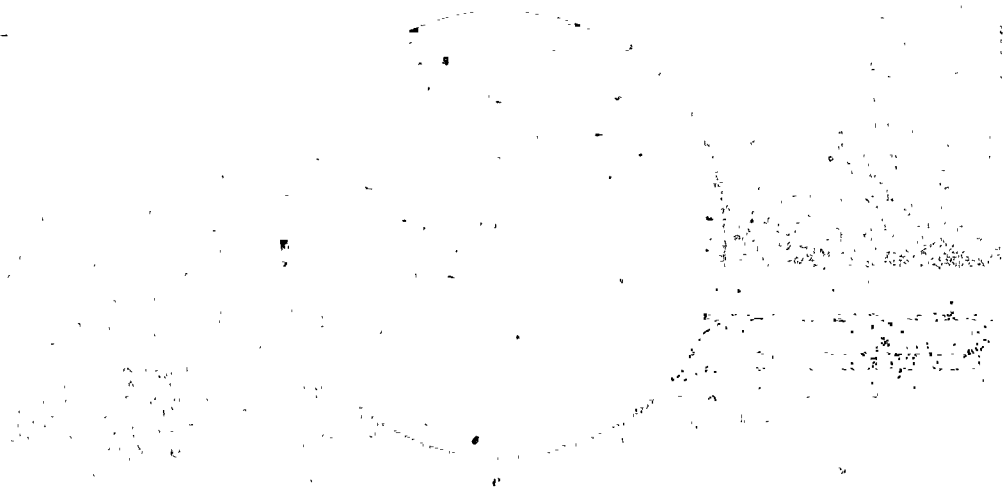
Plate I

100μ

a

100μ

b

c

d

Plate II

a   *b*

c

Plate III

100µ

a

b

100µ

c

d

Plate IV

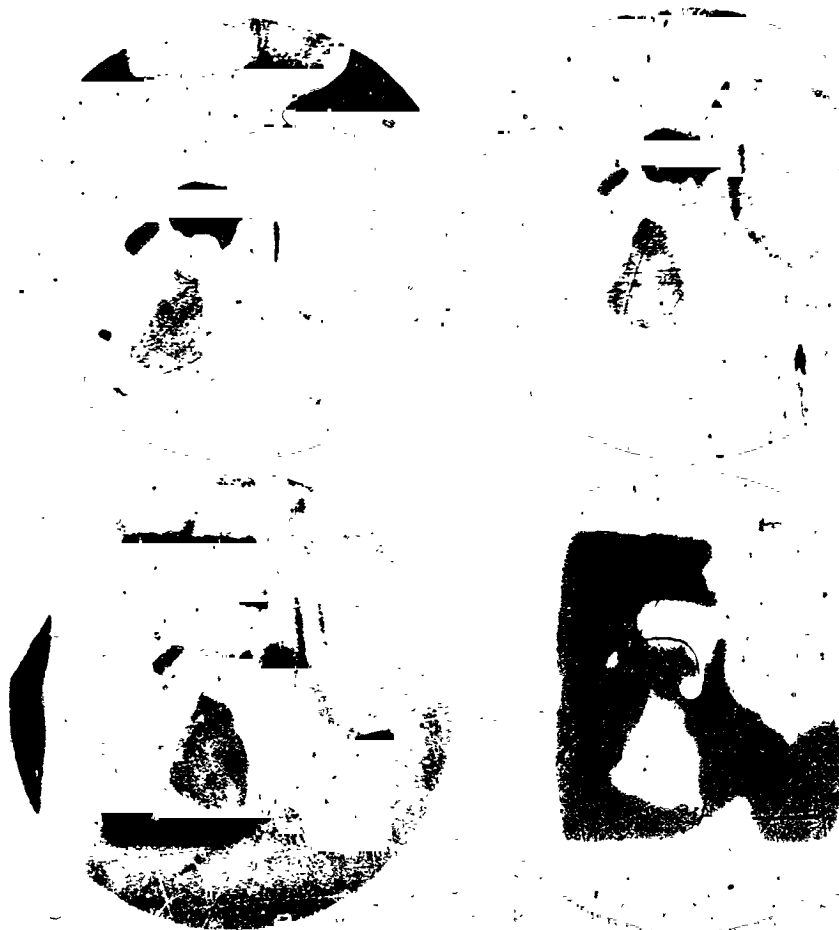Si   Mg

100μ

Plate V

100μ

a

b

c
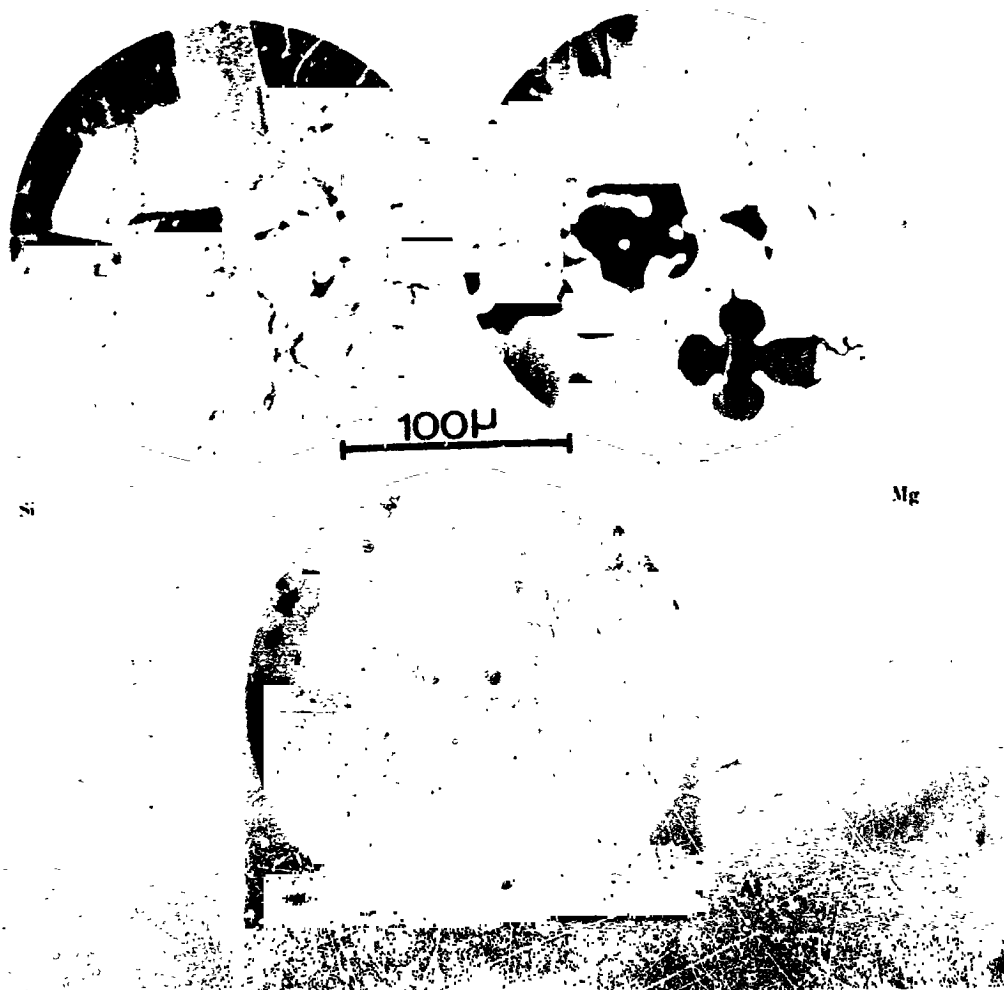
Plate VI

Plate VII

FIG. 17.

Plate VIII

FIG. 23.

FIG. 24